UPC CTTC

Development of a finite volume method for elastic materials and fluid-solid coupled applications

Centre Tecnològic de Transferència de Calor
Departament de Màquines i Motors Tèrmics
Universitat Politècnica de Catalunya

Ignacio González Acedo
Doctoral Thesis

Development of a finite volume method for elastic materials and fluid-solid coupled applications

Ignacio González Acedo

TESI DOCTORAL

presentada al

Departament de Màquines i Motors Tèrmics
ESEIAAT
Universitat Politècnica de Catalunya

per a l'obtenció del grau de

Doctor per la UPC

Terrassa, March 8, 2019

Development of a finite volume method for elastic materials and fluid-solid coupled applications

Ignacio González Acedo

Director de la tesi

Dr Carlos David Pérez Segarra

Tutor

Dr Assensi Oliva Llena

Tribunal Qualificador

Dr Antonio María Pascau Benito
Universidad de Zaragoza

Dr Francesc Xavier Trias Miquel
Universitat Politècnica de Catalunya

Dr Philip Cardiff
University College Dublin

Esta tesis está dedicada a
mis padres Carlos y Ana Cristina,
y a mis hermanos Carlitos y Javi

Acknowledgements

I would like to express my sincere gratitude to Prof. Assensi Oliva, director of the Heat and Mass Transfer Technological Center (CTTC), for placing his trust in me and encouraging me to pursue a PhD. I am also indebted to my supervisor, Prof. Carlos David Pérez Segarra, for his continuous guidance and support during this study.

I wish to thank Prof. Joaquim Rigola for his interest and motivation, and all past and present members of the CTTC who have collaborated on this work, academically, technically and administratively.

Thanks to UCD School of Mechanical & Materials Engineering, particularly to Prof. Alojz Ivanković and Dr Philip Cardiff, for their valuable comments during my short stay.

The financial support provided by the Ministerio de Educación, Cultura y Deporte, Spain, through the FPU13-03850 fellowship is gratefully acknowledged.

Contents

Abstract

This thesis presents the development of a parallel finite volume numerical method to analyse thermoelastic and hyperelastic materials and applied problems with mutual interaction between a fluid and a structure.

The solid problem follows a cell-centred finite volume formulation for three-dimensional unstructured grids under the same framework that is frequently devoted to computational fluid dynamics. Second-order accurate schemes are used to discretise both in time and space. A direct implicit time integration promotes numerical stability when facing vibration and quasi-static scenarios. The geometrical non-linearities, encountered with the large displacements of both Saint Venant-Kirchhoff and neo-Hookean models, are tackled by means of an updated Lagrangian approach.

Verification of the method is conducted with canonical cases which involve: static equilibrium, thermal stress, vibration, structural damping, large deformations, nearly incompressible materials and high memory usage. Significant savings in computation time are achieved owing to the acceleration strategies implemented within the system resolution, namely a segregated algorithm with Aitken relaxation and a block-coupled system arrangement. The similarities between the block-coupled method and the displacement-based finite element method, with regards to the matrix form of the resulting equations, allow for including Rayleigh viscous damping within a finite volume solver.

The program for structures is to be coupled with the in-house fluid numerical models in order to produce a unified fluid-structure interaction platform, where an arbitrary Lagrangian-Eulerian approach is used to solve the flow in a conforming grid. As a first step, the method for incompressible Newtonian fluids is adapted to deal with structure-coupled problems. To do so, the Lagrangian-Eulerian version of the Navier-Stokes equations is presented, and automatic moving mesh techniques are developed. These techniques are designed to mitigate the mesh quality deterioration and to satisfy

the space conservation law. Besides, a semi-implicit coupling algorithm, which only implicitly couples the fluid pressure term to the structure, is implemented. As a result, numerical stability for strongly coupled phenomena at a reduced computational cost is obtained. These new tools are tested on an applied case, consisting of the turbulent flow through self-actuated flexible valves.

Finally, a pioneering coupled numerical model for the thermal and structural analysis of packed-bed thermocline storage tanks is developed. This thermal accumulation system for concentrated solar power plants has attracted the attention of the industry due to the economic advantage compared to the usual two-tank system. Dynamic coupling among the thermoelastic equations for the tank shell and the numerical models for all other relevant elements of the system is considered. After validating the model with experimental results, the commercial viability of the thermocline concept, regarding energetic effectiveness and structural reliability, is evaluated under real operating conditions of the power plants.

1

Introduction

1.1 Background and motivation

There are many engineering applications where the behaviour of a fluid depends on the movement and temperature of a structure, and vice versa. Fluttering and static deformation of aircraft and turbomachinery, dynamics of lightweight structures such as airbags or parachutes, and stresses in high-temperature solar collectors and nuclear reactors are some examples of dynamic coupling between fluid and solid media. Their relevance within the design process of contemporary technology has given rise to specific research on the field categorised as fluid-structure interaction (FSI). The difficulty in modelling FSI systems analytically, due to their inherent non-linearity, and the limitations in scope of laboratory experiments have fostered the development of numerical methods for this purpose [1].

An FSI case of industrial interest can be found in concentrated solar power plants, specifically in a novel system to store the thermal energy extracted from solar irradiation. It consists of a dual-media vessel containing a fluid and a granulate material, usually referred to as packed-bed thermocline tank, which takes advantage of thermal stratification and the inner bulk material to reduce the costs of the commonly-used two-tank system [2]. Despite the economic benefit, there is still a concern regarding the structural integrity of the tank, taking into account the strong thermal gradient of the contained fluid and the different thermal expansion of the tank walls and inner materials. A better understanding of the commercial viability of thermocline approach, with emphasis on structural reliability, is lacking in the industry. Therefore, a detailed numerical analysis of this storage alternative, which integrates the structure, the inner

substances and other significant elements of the system would be of great value.

The group where this thesis has been elaborated is especially aligned with this type of applied research, focused on the thermal and fluid-dynamic optimisation of engineering equipment. It is one of its work lines, along with a more basic research. From the eighties [3, 4] to now, the group has accumulated a long experience in mathematical formulation, numerical resolution and experimental validation of fluid dynamics and heat and mass transfer phenomena. Some of the physical aspects studied include: natural and forced convection, aerodynamics, large-eddy simulation (LES), combustion, multiphase flows, radiation, porous media and particle-fluid systems.

The work carried out by the group has been accompanied by the development of an in-house multiphysics computational fluid dynamics (CFD) code called TermoFluids [5]. The software is programmed in C++ following the object-oriented paradigm and designed for high-performance parallel computing [6]. It is based on a three-dimensional finite volume formulation for unstructured grids. Among the capabilities that it incorporates are iterative and direct linear solvers, moving mesh methods, adaptive mesh refinement and sliding meshes. An exhaustive list of publications featured in the research group can be found in [7].

To predict the response of the thermocline storage system numerical methods to solve structures and their thermo-mechanical interaction with other elements are required. Additionally, extending these coupling tools, especially those used for the strong interaction between a structure and a fluid, will help to cope with a broader variety of engineering problems in the future.

1.2 Objectives of the thesis

The hybrid numerical approach to solve FSI problems uses two different numerical methods and programmes to model each sub-domain, for instance, a finite volume method for the fluid and a finite element method for the solid. An interface module needs to handle data communication between both packages.

In the unified approach, both media are solved by means of a common numerical framework, making easier and more consistent the information exchange and avoiding coupling limitations imposed by third-party programmes.

The strong potential achieved by the research group with respect to CFD modelling makes evident the use of TermoFluids finite volume solvers for fluids in our FSI studies. Precisely, this experience with finite volumes and the similarity between the governing equations of fluid and solid lead us to consider adopting the same discretisation method

to solve the solid domain. By using the same numerical method and software infrastructure, we would facilitate and expand the capabilities of the coupling strategy derived from a unified FSI approach. In addition, the platform would preserve the underlying simplicity and strongly conservative nature of the finite volume method for the coupled discretised problem. The decision also lies in the fact that other authors have already demonstrated the accuracy and efficiency of the finite volume method for computational solid mechanics (see for example [8–10]) and its fruitful integration into unified FSI programmes (see for example [11–15]).

In this manner, the specific objectives of this thesis are:

- To develop a structural method within TermoFluids code, which will use the same three-dimensional finite volume unstructured formulation and includes parallel computing capabilities. The model is to be used for applied problems with thermo-mechanical interaction with a fluid, where large deformations may be expected.

- To develop the complementary tools to build the FSI platform, aiming at an arbitrary Lagrangian-Eulerian (ALE) description of the fluid. As a result, a proper ALE formulation of the fluid equations, a moving mesh method which adjusts the fluid mesh to the new space defined by the solid interface, and a fluid-structure algorithm should be implemented. Since no changes in the mesh topology will be considered at this stage, validity and quality of the adapted mesh will become a challenge to be solved when facing big alterations of the domain.

- To verify the correct performance of the implemented FSI tools by studying a coupled problem from the engineering field.

- To carry out a thermo-mechanical analysis of the thermocline energy storage tanks by coupling the behaviour of the main elements of the system. Thermal efficiency and structural integrity should be measured, and insight into the wall thermal stresses should be gained.

The present work follows the path started by Olga Estruch within the group, who developed a moving mesh method based on radial basis functions [16] and implemented an early version of the solid finite volume method, which was finally redesigned from scratch.

1.3 Outline of the thesis

The next chapter (chapter 2) is devoted to present the mathematical formulation, spatial discretisation on three-dimensional unstructured grids and time integration for solving the elasticity equations. Linear thermoelasticity and hyperelasticity models are considered. A direct calculation of the displacement gradient at the faces improves the accuracy of the solution, especially on the boundaries of the domain. Special attention is paid to the arrangement of the coupled linear system in order to accelerate the computational convergence.

The implemented method is verified in chapter 3 by assessing different aspects of solid numerical analysis: static equilibrium, thermal stresses, vibration, structural damping, large deformations and nearly incompressible materials. A comparison among the different techniques to speed up the performance is conducted by measuring calculation times both on a workstation and a supercomputer.

Having successfully developed a new and competitive numerical tool for structural analysis, it is time to build the foundation for its future coupling with the CFD of TermoFluids. Chapter 4 is dedicated to the description of the methodology used for the resolution of the incompressible flow in FSI problems. The method is concerned with a conforming mesh and an ALE approach, along with an innovative semi-implicit coupling algorithm for strong mutual fluid-solid dependence. The design of this coupling scheme has been elaborated by Alireza Naseri within the group. All these tools are employed to conduct the simulation of the flow through flexible reed valves. The structure is modelled according to a two-dimensional plate theory. Different physical phenomena are encountered in this case of industrial interest: fluid-structure interaction, turbulent flow with separations, shedding vortices and solid impact.

In chapter 5, a thermo-mechanical analysis of packed-bed thermocline storage tanks is performed. Dynamic coupling among the solution of the most significant components of the thermal system, including the tank walls and the inner heat transfer fluid, is taken into account. The thermoelastic finite volume solver is used. After validating the model with experimental results, the commercial viability of the thermocline tank, regarding energetic effectiveness and structural reliability, is evaluated under real working conditions of concentrated solar power plants.

Chapter 6 summarises the main conclusions of the work and proposes research strategies for the future.

References

[1] G. Hou, J. Wang, and A. Layton. Numerical methods for fluid-structure interaction — A review. *Communications in Computational Physics*, 12(2):337–377, 2012.

[2] A. Gil, M. Medrano, I. Martorell, A. Lázaro, P. Dolado, B. Zalba, and L. F. Cabeza. State of the art on high temperature thermal energy storage for power generation. Part 1—Concepts, materials and modellization. *Renewable and Sustainable Energy Reviews*, 14(1):31 – 55, 2010.

[3] A. Oliva. *Systematic numerical resolution of heat transfer by conduction and convection under subsonic and stabilisation conditions (in Spanish)*. PhD thesis, Universitat Politècnica de Catalunya, 1982.

[4] C. D. Pérez-Segarra. *Numerical criteria in the resolution of heat transfer in convection phenomena (in Spanish)*. PhD thesis, Universitat Politècnica de Catalunya, 1988.

[5] Termo Fluids S.L. http://www.termofluids.com/.

[6] R. Borrell, J. Chiva, O. Lehmkuhl, G. Oyarzun, I. Rodríguez, and A. Oliva. Optimising the TermoFluids CFD code for petascale simulations. *International Journal of Computational Fluid Dynamics*, 30(6):425–430, 2016.

[7] Heat and Mass Transfer Technological Center (CTTC) - Universitat Politècnica de Catalunya - BarcelonaTech (UPC). http://www.cttc.upc.edu/.

[8] I. Demirdžić and S. Muzaferija. Finite volume method for stress analysis in complex domains. *International Journal for Numerical Methods in Engineering*, 37(21):3751–3766, 1994.

[9] H. Jasak and H. G. Weller. Application of the finite volume method and unstructured meshes to linear elasticity. *International Journal for Numerical Methods in Engineering*, 48(2):267–287, 2000.

[10] P. Cardiff, Ž. Tuković, P. D. Jaeger, M. Clancy, and A. Ivanković. A lagrangian cell-centred finite volume method for metal forming simulation. *International Journal for Numerical Methods in Engineering*, 109(13):1777–1803, 2017.

[11] A. Ivanković, A. Karač, E. Dendrinos, and K. Parker. Towards early diagnosis of atherosclerosis: the finite volume method for fluid-structure interaction. *Biorheology*, 39(3-4):401, 2002.

[12] A. Kovacevic, N. Stosic, and I. K. Smith. A numerical study of fluid-solid interaction in screw compressors. *International Journal on Computer Application in Technology*, 21(4):148–158, 2004.

[13] C. Habchi, S. Russeil, D. Bougeard, J.-L. Harion, T. Lemenand, A. Ghanem, D. D. Valle, and H. Peerhossaini. Partitioned solver for strongly coupled fluid–structure interaction. *Computers & Fluids*, 71:306–319, 2013.

[14] H.-D. Yao, M. Y. Svensson, and H. Nilsson. Deformation of dorsal root ganglion due to pressure transients of venous blood and cerebrospinal fluid in the cervical vertebral canal. *Journal of Biomechanics*, 76:16–26, 2018.

[15] Ž. Tuković, A. Karač, P. Cardiff, H. Jasak, and A. Ivanković. OpenFOAM finite volume solver for fluid-solid interaction. *Transactions of FAMENA*, 42(3):1–31, 2018.

[16] O. Estruch, O. Lehmkuhl, R. Borrell, C. D. Pérez-Segarra, and A. Oliva. A parallel radial basis function interpolation metohd for unstructured dynamic meshes. *Computer & Fluids*, 80:44–54, 2012.

2

A finite volume method for structural dynamics

2.1 Introduction

The finite element method was initially developed to model structural analysis and nowadays has become the most extended tool in the field of computational solid mechanics [1, 2]. The development of the finite volume method, instead, was aligned with computational fluid dynamics. However, both the inherent simplicity and strong conservation qualities of the finite volume formulation, along with the similarities between the governing equations, attracted researchers to solve solid mechanics with finite volume methods.

Before proceeding, it is important to distinguish between two types of approaches of the finite volume method towards structural physics. On the one hand, the vertex-centred variable arrangement requires a secondary grid to delimit the control volumes and is, in fact, a particular case of the finite element method with non-Galerkin weighting [3–8]. On the other hand, there is the cell-centred formulation, where control volumes coincide with the mesh and discretisation points are placed at the centre of the cells over which the conservation laws are imposed. Concerning the latter path, the pioneer model by [9] for linear thermoelastic materials in two-dimensional Cartesian meshes represent the first contribution. Early works from [10, 11] were proving as well the validity of this finite volume approach for structures with alternative perspectives.

The cell-centred model rapidly incorporated complex three-dimensional domains

[12] and parallel computing functionalities [13]. Since the original linear problem, subsequent modellings to handle different constitutive relationships and magnitude of deformations have been developed: thermo-elastoplasticity [14, 15], elastoplasticity [16], hyperelasticity [17, 18], thermo-viscoelasticity [19], incompressible elasticity [20–22], poro-elastoplasticity [23], hyperelastoplasticity [15, 24] and anisotropy [18, 25, 26].

In parallel, other specific solid phenomena have been studied with the same finite volume framework, such as fracture mechanics [27–30], Mindlin-Reissner plate models [31–34], extrusion process with arbitrary Lagrangian-Eulerian description [35] or electrostatic loads [36]. Boundary conditions have been a matter of investigation too. Some examples can be found in contact analysis, both static two-dimensional [13] and dynamic three-dimensional [37], and musculotendon surface forces [38].

Cell-centred finite volume models generally solve momentum balance implicitly, considering the displacement as the dependent variable, and use second-order accurate approximations to discretise the equation spatially. Therefore, special mention should be given to [39, 40], who developed explicit analysis with mixed formulations suitable for wave propagation, bending scenarios and incompressible materials, and to [41], who presented a fourth order spatial discretisation to alleviate shear locking.

Typical resolution method for the resulting linearised system is based on a segregated algorithm. Equations of each displacement direction are decoupled into three different linear systems where the inter-component dependencies have been deferred to the source term. Thus, the convergence of a time implicit solution needs to perform outer fixed-point iterations. The result is a proved robust procedure that additionally requires low computer memory. Nevertheless, it can experience slow convergence rates when there is strong coupling between displacement components, for example in bending of extended structures.

Consequently, different solutions to accelerate the solution convergence have been proposed in the literature. A full multigrid algorithm based on V cycles and a correction scheme was used in [25, 42]. In [36], the entire elasticity equation for small deformations was arranged in a single linear system by integrating the discretisation coefficients of the displacement gradient into a coupled matrix. The method showed dramatical improvement in the convergence rate. Similarly, [43] defined a block-coupled solver for linear elasticity which resulted in less execution time and memory requirements than a finite element software for the set of cases tested.

An invaluable comprehensive review of all the literature on the finite volume method for solid mechanics produced in the last thirty years can be found in [44]. Critical analysis of the different approaches and recommendations for future progress are given.

The current work addresses the development of a finite volume method for structures capable of dealing with unstructured three-dimensional grids. The new structural tool has been implemented into the group's parallel object-oriented code called TermoFluids [45]. Linear thermoelasticity and hyperelasticity models are taken into account and special emphasis is placed on computational performance. For this purpose, three techniques are followed: a lightweight second-order vertex interpolation [46], a segregated algorithm with both an Aitken acceleration and a transient predictor step, and a block-coupled system arrangement [43].

The second pillar of the presented finite volume methodology is the enhanced evaluation of the stress. Following the contributions from [43, 47], displacement gradient (and hence strain and stress) are computed directly on the cell faces, instead of interpolating its value from the adjacent cell centres. Thereon, independent numerical schemes are employed to discretise normal and tangential components of the gradient in order to obtain a coherent formulation between implicit and correction terms and an improved accuracy at the boundaries.

Finally, further novelties of the implemented program can be identified in terms of dynamic analysis. Four time schemes are available for the inertial term, including the Bathe method [48, 49], not used within finite volume frameworks yet. Furthermore, the addition of Rayleigh structural damping is new too, since finite volume methods have only considered scalar-coefficient viscous damping up to now.

This chapter presents the mathematical description and the numerical procedures followed to solve the solid problem. Firstly, various measures of continuum motion and deformation are summarised in section 2.2. The conservation equations in section 2.3 are followed by the constitutive relationships of linear thermoelastic, Saint Venant-Kirchhoff and neo-Hookean materials in section 2.4. In this manner, closed systems of integral equations, under both linear and nonlinear hypothesis, can be assembled in section 2.5. Sections 2.6 and 2.7 provide the main characteristics of the numerical discretisation and the system resolution, respectively. Finally, a brief comment on the code parallelisation is given in section 2.8.

2.2 Deformation and strain

Consider the motion of a continuum body as depicted in figure 2.1. Deformation is the change in dimensions and shape of the body between a reference material configuration at time t_0 (undeformed) and the current configuration at time t (deformed). A material particle P_0, which had a position vector $\boldsymbol{x_0}$ in the reference state, is at position $\boldsymbol{x}$ in the

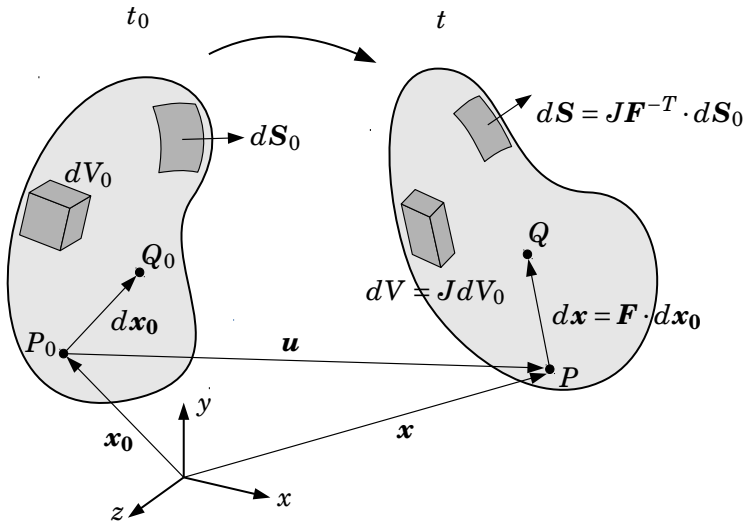

Figure 2.1: Motion of a continuum body from reference configuration at t_0 to current configuration at time t.

current configuration. The motion of the continuum can be defined as the mapping from the material location to the current location $\boldsymbol{x} = \boldsymbol{x}(\boldsymbol{x_0}, t)$. The difference between both initial and final positions is the displacement

$$\boldsymbol{u}(\boldsymbol{x_0}, t) = \boldsymbol{x}(\boldsymbol{x_0}, t) - \boldsymbol{x_0}\,. \tag{2.1}$$

An infinitesimal line segment $d\boldsymbol{x_0}$ only stretches and rotates as a result of the deformation. Then, the deformation can be characterised by the material deformation tensor $\boldsymbol{F}$ according to

$$d\boldsymbol{x} = \frac{\partial \boldsymbol{x}}{\partial \boldsymbol{x_0}} \cdot d\boldsymbol{x_0} = \boldsymbol{F} \cdot d\boldsymbol{x_0}\,, \tag{2.2}$$

where $\boldsymbol{F}$ is the gradient of the mapping function and can be expressed as

$$\boldsymbol{F} = (\nabla_0 \boldsymbol{x})^T = [\nabla_0 (\boldsymbol{x_0} + \boldsymbol{u})]^T = \boldsymbol{I} + (\nabla_0 \boldsymbol{u})^T\,, \tag{2.3}$$

where $\boldsymbol{I}$ is the identity tensor. The material gradient operator ∇_0 finds the derivatives with respect to the material coordinates. The determinant of the material deformation tensor is the Jacobian, $J = \det(\boldsymbol{F})$, and relates the initial and deformed differential

volume:

$$dV = JdV_0\,. \tag{2.4}$$

Likewise, there is a relationship between undeformed and current configurations for area vectors, known as the Nanson's formula:

$$\boldsymbol{n}dS = J\boldsymbol{F}^{-T}\cdot\boldsymbol{n}_0 dS_0\,. \tag{2.5}$$

However, tensor $\boldsymbol{F}$ contains not only information of the deformation but also of rigid body rotation, which does not provoke any stresses in the body. Thus, it is more convenient to work with the magnitude $(d\boldsymbol{x})^2$, which ignores rotation:

$$(d\boldsymbol{x})^2 = d\boldsymbol{x}^T\cdot d\boldsymbol{x} = (\boldsymbol{F}\cdot d\boldsymbol{x_0})^T\cdot(\boldsymbol{F}\cdot d\boldsymbol{x_0}) = d\boldsymbol{x_0}^T\cdot\left(\boldsymbol{F}^T\cdot\boldsymbol{F}\right)\cdot d\boldsymbol{x_0}\,. \tag{2.6}$$

Subtracting $(d\boldsymbol{x_0})^2$ to $(d\boldsymbol{x})^2$ gives a local measure of the deformation between t_0 and t:

$$\begin{aligned}(d\boldsymbol{x})^2-(d\boldsymbol{x_0})^2 &= d\boldsymbol{x_0}^T\cdot\left(\boldsymbol{F}^T\cdot\boldsymbol{F}\right)\cdot d\boldsymbol{x_0} - d\boldsymbol{x_0}^T\cdot\boldsymbol{I}\cdot d\boldsymbol{x_0}\\ &= d\boldsymbol{x_0}^T\cdot\left(\boldsymbol{F}^T\cdot\boldsymbol{F}-\boldsymbol{I}\right)\cdot d\boldsymbol{x_0}\\ &= d\boldsymbol{x_0}^T\cdot(2\boldsymbol{E})\cdot d\boldsymbol{x_0}\,,\end{aligned} \tag{2.7}$$

where

$$\boldsymbol{E} = \frac{1}{2}\left(\boldsymbol{F}^T\cdot\boldsymbol{F}-\boldsymbol{I}\right) = \frac{1}{2}\left[\nabla_0\boldsymbol{u}+(\nabla_0\boldsymbol{u})^T+\nabla_0\boldsymbol{u}\cdot(\nabla_0\boldsymbol{u})^T\right] \tag{2.8}$$

is the Green-Lagrange finite strain tensor. When the deformations are sufficiently small, the strain measure can be simplified by neglecting the high-order terms, giving place to the infinitesimal strain tensor:

$$\boldsymbol{\varepsilon} = \frac{1}{2}\left[\nabla_0\boldsymbol{u}+(\nabla_0\boldsymbol{u})^T\right]. \tag{2.9}$$

Similarly, the difference of equation 2.7 can be formulated referred to the current configuration according to $d\boldsymbol{x_0} = \boldsymbol{F}^{-1}\cdot d\boldsymbol{x}$, and then

$$(d\boldsymbol{x})^2-(d\boldsymbol{x_0})^2 = d\boldsymbol{x}^T\cdot(2\boldsymbol{e})\cdot d\boldsymbol{x}\,, \tag{2.10}$$

where $\boldsymbol{e}$ is the Euler-Almansi finite strain tensor:

$$\boldsymbol{e} = \frac{1}{2}\left(\boldsymbol{I}-\boldsymbol{F}^{-T}\cdot\boldsymbol{F}^{-1}\right). \tag{2.11}$$

Another rotation-independent deformation measure is the left Cauchy-Green deformation tensor, whose invariants are used to derive stress-strain relationships,

$$\boldsymbol{B} = \boldsymbol{F} \cdot \boldsymbol{F}^T . \tag{2.12}$$

2.3 Governing equations

The mechanics of a continuum medium is governed by the fundamental conservation laws of mass, linear momentum, angular momentum and energy.

The mass conservation principle requires the total time derivative of the mass to vanish, i.e. to preserve the mass of the system:

$$\frac{D}{Dt}\int_V \rho dV = 0 , \tag{2.13}$$

which can be rewritten considering V as a Lagrangian control volume, and the relation between initial and final volumes of equation 2.4:

$$\begin{aligned}\int_{V_0} \rho(\boldsymbol{x_0}, t_0) dV_0 &= \int_V \rho(\boldsymbol{x}, t) dV \\ &= \int_{V_0} \rho(\boldsymbol{x}(\boldsymbol{x_0}, t), t) J dV_0 ,\end{aligned} \tag{2.14}$$

where $\rho(\boldsymbol{x_0}, t_0) = \rho_0$ and $\rho(\boldsymbol{x}, t) = \rho$ are the densities at the reference and current configurations, respectively. As a result, mass conservation is condensed in a relation of densities:

$$\int_{V_0} \left(\rho_0 - J\rho\right) dV_0 = 0 \quad \Rightarrow \quad \rho_0 = \rho J . \tag{2.15}$$

The conservation of momentum states that the total change in linear momentum is equal to the net force acting on the system, resulting from surface forces (or stresses) and volumetric body forces:

$$\frac{D}{Dt}\int_V \rho \dot{\boldsymbol{u}} dV = \int_V \nabla \cdot \boldsymbol{\sigma} dV + \int_V \rho \boldsymbol{b} dV , \tag{2.16}$$

where $\dot{\boldsymbol{u}}$ is the velocity, $\boldsymbol{b}$ is the body force per unit mass, ∇ is the gradient operator with respect to the current geometry and $\boldsymbol{\sigma}$ is the Cauchy stress tensor. The force per unit area acting on a surface with normal unit vector $\boldsymbol{n}$ is obtained with the product $\boldsymbol{n} \cdot \boldsymbol{\sigma}$. After applying the divergence theorem in the stress term, and both Reynolds' transport

theorem and a Lagrangian description in the time derivative, the balance results in:

$$\int_V \frac{\partial}{\partial t}\left(\rho \dot{\boldsymbol{u}}\right) dV = \int_S \boldsymbol{n}\cdot\boldsymbol{\sigma} dS + \int_V \rho \boldsymbol{b} dV\,, \tag{2.17}$$

where $\boldsymbol{n}$ is the outward-pointing normal of the closed surface S that fully encloses the control volume V.

The angular momentum is conserved if and only if the Cauchy stress tensor is symmetric (the derivation can be found for example in [50]):

$$\boldsymbol{\sigma}^T = \boldsymbol{\sigma}\,. \tag{2.18}$$

The balance of energy considers heat and mechanical work as energy sources. The integral form of its equation takes the form:

$$\frac{D}{Dt}\int_V \rho e dV = -\int_S \boldsymbol{q}\cdot\boldsymbol{n} dS + \int_V q_r dV + \int_V \rho \boldsymbol{b}\cdot\dot{\boldsymbol{u}} dV + \int_S (\boldsymbol{n}\cdot\boldsymbol{\sigma})\cdot\dot{\boldsymbol{u}} dS\,, \tag{2.19}$$

where e is the total specific energy, $\boldsymbol{q}$ the heat flux across a surface element dS and q_r the radiation energy per unit volume absorbed from the surroundings. Last two terms on the right-hand side represent, from left to right, the work done by body forces and surface forces. The energy law can be transformed into the conservation of thermal energy as

$$\int_V \frac{\partial}{\partial t}\left(\rho u\right) dV = -\int_S \boldsymbol{q}\cdot\boldsymbol{n} dS + \int_V q_r dV + \int_V \boldsymbol{\sigma} : \nabla\dot{\boldsymbol{u}} dV \tag{2.20}$$

after considering the total energy as the sum of internal and kinetic energy ($e = u + \frac{1}{2}\dot{\boldsymbol{u}}\cdot\dot{\boldsymbol{u}}$), and after subtracting the mechanical energy balance, which derives from the dot product between the momentum equation 2.17 and the velocity vector.

It is important to note that both conservation equations 2.17 and 2.20 should be satisfied at instant t, and thus they are integrated over the current deformed configuration.

2.4 Constitutive relationships

Thus far, eight equations based on physics fundamental laws have been defined: conservation of mass 2.15 (1), momentum 2.17 (3), angular momentum 2.18 (3) and energy 2.20 (1). But there are seventeen unknown variables: density ρ (1), displacement $\boldsymbol{u}$ (3), stress $\boldsymbol{\sigma}$ (9), heat flux $\boldsymbol{q}$ (3) and internal energy u (1). This section includes the

remaining required mathematical relations between the variables to determine the whole system of equations completely, known as the constitutive equations. The target is to have the displacement $\boldsymbol{u}$ and temperature T as the only dependent variables, i.e. a displacement-based formulation.

Unfortunately, constitutive relationships cannot describe the complex behaviour of all different materials over their entire range of deformations [15]. Consequently, specific models are formulated to approximate experimental behaviours of certain materials over a suitably restricted range [51].

In this case, two types of elastic behaviours will be modelled: linear thermoelasticity and isothermal hyperelasticity. Elastic deformations are reversible and time independent, and therefore the original configuration can be recovered when loads are removed. This behaviour is captured before the onset of the plastic regime and when viscous effects can be neglected.

2.4.1 Linear thermoelastic material

Linear thermoelasticity considers mechanical and thermal loads, and assume the resulting deformations and rotations to be small. In this way, thermal and mechanical strains can be linearly added, and a linear relationship between stress and both strain and temperature can be defined [52]. For an isotropic material, the equation is defined by the Duhamel-Neumann form of Hooke's law:

$$\boldsymbol{\sigma} = 2\mu\boldsymbol{\varepsilon} + \lambda \mathrm{tr}(\boldsymbol{\varepsilon})\boldsymbol{I} - 3K\alpha(T - T_0)\boldsymbol{I}\,, \tag{2.21}$$

where λ and μ are the Lamé's parameters, K is the bulk modulus, α is the coefficient of linear thermal expansion and T_0 is the temperature corresponding to the unstrained state. In this case, isotropy allows for determining the strain-stress relation with only three mechanical properties of the material, usually modulus of elasticity E (Young's modulus), Poisson's coefficient ν and α. Accordingly, Lamé's parameters and bulk modulus can be obtained by a combination of them:

$$\mu = \frac{E}{2(1+\nu)}\,, \tag{2.22}$$

$$\lambda = \frac{\nu E}{(1+\nu)(1-2\nu)}\,, \tag{2.23}$$

$$K = \frac{E}{3(1-2\nu)}\,, \tag{2.24}$$

where $E > 0$ and $-1 \leqslant \nu < 0.5$. Poisson's ratio equal to 0.5 belongs to an incompressible material, whose bulk modulus approaches infinity.

For an isothermal process, temperature difference $T - T_0 = 0$, and the last term of equation 2.21 vanish. The result is the classical Hooke's law for linear elasticity, where there are no thermal stresses. When there is a temperature change, though, conditions for zero thermal stress become severe: uniform or linear distribution of temperature, boundaries free of traction and temperature-independent mechanical properties. Otherwise, thermal expansion is constrained by external supports or by other parts of the same body, and thermal stress emerges [52, 53].

Concerning the energy balance, the heat flux is described proportional to the temperature gradient according to the empirical Fourier's law:

$$\boldsymbol{q} = -k\nabla T\,, \tag{2.25}$$

where k is the thermal conductivity of the material.

Besides, internal energy is related as well to temperature by the following equation of state

$$du = c_E dT\,, \tag{2.26}$$

as can be deduced for example in [52]. Material property c_E defines the specific heat at constant strain, whose value is close to the value of c_v within the theory of linear elasticity.

The last term of equation 2.20 reflects a dependency between temperature and velocity of deformation. With the small strain assumption, it can be proved to be equivalent to

$$\boldsymbol{\sigma} : \nabla \dot{\boldsymbol{u}} = -3K\alpha T \mathrm{tr}(\dot{\boldsymbol{\varepsilon}})\,, \tag{2.27}$$

and therefore, when $\mathrm{tr}(\dot{\boldsymbol{\varepsilon}}) < 0$ (transient volume compression) heat is generated, whereas when $\mathrm{tr}(\dot{\boldsymbol{\varepsilon}}) > 0$ (transient volume expansion) heat is lost. This phenomenon becomes significant when thermal stress waves are produced as a result of the rapid application of a thermal load. However, in most practical engineering cases this load varies sufficiently slowly so as not to excite inertia effects, and this term can be neglected [52]. In this way, the energy balance reduces to a conduction heat transfer equation. Depending on whether this term is considered or not, the linear thermoelasticity theory is described as coupled or uncoupled, respectively.

2.4.2 Hyperelastic materials

Strain-stress relationships of hyperelastic materials are derived from a strain energy function such that the stress at a particle is a function of the current deformation ($\boldsymbol{F}$) associated with that particle. Thus, the response of the material is path-independent. Hyperelasticity acts as model of elastic materials which are subjected to very large deformations and exhibit nonlinear behaviour, namely elastomers, polymers, foams and biological tissues [51, 54].

Unlike what happens with the infinitesimal elasticity and Hooke's law (section 2.4.1), a wide range of strain-stress relations have been formulated under the hyperelastic hypothesis. Here the focus will be on two models suitable when thermal effects are negligible in front of mechanical effects. Consequently, medium is governed by conservation equations of mass and momentum, and only the displacement works as primary variable. The simplest model of a hyperelastic material is the Saint Venant-Kirchhoff material. It arises from using Hooke's law for infinitesimal deformations (see equation 2.21) but with two different strain and stress tensors: the Green-Lagrange finite strain tensor $\boldsymbol{E}$, formulated in equation 2.8, and the second Piola-Kirchhoff stress tensor $\boldsymbol{\Sigma}$. The resulting form of the isotropic constitutive relationship is [55]

$$\boldsymbol{\Sigma} = 2\mu\boldsymbol{E} + \lambda \mathrm{tr}(\boldsymbol{E})\boldsymbol{I}\,. \tag{2.28}$$

This stress tensor gives the current force transformed to the reference configuration, i.e. $d\boldsymbol{t}_0 = \boldsymbol{n}_0 \cdot \boldsymbol{\Sigma} dS_0$ and then $d\boldsymbol{t} = \boldsymbol{F} \cdot d\boldsymbol{t}_0$. It is a symmetric tensor which is related to the real Cauchy stress as

$$\boldsymbol{\sigma} = \frac{1}{J}\boldsymbol{F} \cdot \boldsymbol{\Sigma} \cdot \boldsymbol{F}^T\,. \tag{2.29}$$

In this manner, equation 2.28 can be rewritten in terms of the Cauchy stress:

$$\boldsymbol{\sigma} = \frac{\boldsymbol{B}}{2J}\left[2\mu(\boldsymbol{B}-\boldsymbol{I}) + \lambda \mathrm{tr}(\boldsymbol{B}-\boldsymbol{I})\boldsymbol{I}\right]. \tag{2.30}$$

Saint Venant-Kirchhoff material model defines a high-order strain-stress relation and is coherent with the infinitesimal theory (because both $\boldsymbol{\Sigma}$ and $\boldsymbol{E}$ in equation 2.28 tend to $\boldsymbol{\sigma}$ and $\boldsymbol{\varepsilon}$ when $\boldsymbol{u} \to 0$). Nevertheless, it suffers from instabilities when representing very large strains as a result of not verifying the polyconvexity conditions [55]. For this reason, this relationship is limited to cases with large displacements and large rotations but small strains.

The neo-Hookean hyperelastic material, instead, does not have such limitation and

reduces as well to the linear elastic model for small strains and rotations [56]:

$$\boldsymbol{\sigma} = \frac{\mu}{J}(\boldsymbol{B} - \boldsymbol{I}) + \frac{\lambda}{J}(\ln J)\boldsymbol{I}\,. \tag{2.31}$$

A truly incompressible material ($\nu = 0.5$, $K = \infty$, $J = 1$) needs to be modelled with a constitutive equation different from the compressible version. In this case all relations 2.21, 2.28 and 2.31 are compressible. Moreover, a different formulation of the system is necessary, like the mixed approach which adds the hydrostatic pressure as another structural variable [57]. But experience demonstrates that many large strain materials resist volume changes and thus behave under incompressible or near incompressible conditions. As a consequence, an intermediate neo-Hookean model, which helps to enforce near incompressibility within the traditional displacement-based formulation, is sometimes suitable [51, 56]:

$$\boldsymbol{\sigma} = \mu(J-1)\boldsymbol{I} + \frac{K}{J^{5/3}}\left(\boldsymbol{B} - \frac{1}{3}\mathrm{tr}(\boldsymbol{B})\boldsymbol{I}\right). \tag{2.32}$$

2.5 Mathematical model

This section aims at displaying the resulting governing equations as a function of the system primary variables for both material models presented in section 2.4. The summary will allow for identifying the key features of the numerical resolution. First of all, it is important to keep in mind that the balance laws of energy and momentum (equations 2.20 and 2.17, respectively) are integrated over the current deformed configuration at time t. But this geometry is not established from the beginning, because the displacement of material particles is unknown, and then it is necessary to reformulate them in terms of the initial undeformed configuration. To do so, kinematic relations 2.4 and 2.5 can be used such that:

$$\int_{V_0} \rho_0 \frac{\partial u}{\partial t} dV_0 = -\int_{S_0} \boldsymbol{q} \cdot \left(J\boldsymbol{F}^{-T} \cdot \boldsymbol{n}_0\right) dS_0 + \int_{V_0} q_r J dV_0 + \int_{V_0} (\boldsymbol{\sigma} : \nabla \dot{\boldsymbol{u}}) J dV_0\,, \tag{2.33}$$

$$\int_{V_0} \rho_0 \ddot{\boldsymbol{u}} dV_0 = \int_{S_0} \left(J\boldsymbol{F}^{-T} \cdot \boldsymbol{n}_0\right) \cdot \boldsymbol{\sigma} dS_0 + \int_{V_0} \rho_0 \boldsymbol{b} dV_0\,, \tag{2.34}$$

where $\ddot{\boldsymbol{u}} = (\partial \dot{\boldsymbol{u}}/\partial t)$ is the acceleration.

On the one hand, when dealing with a linear thermoelastic case, displacements are considered infinitesimal, and differences between reference and current configurations are negligible. Displacement nonlinear terms can be neglected so that $dV \approx dV_0$ and

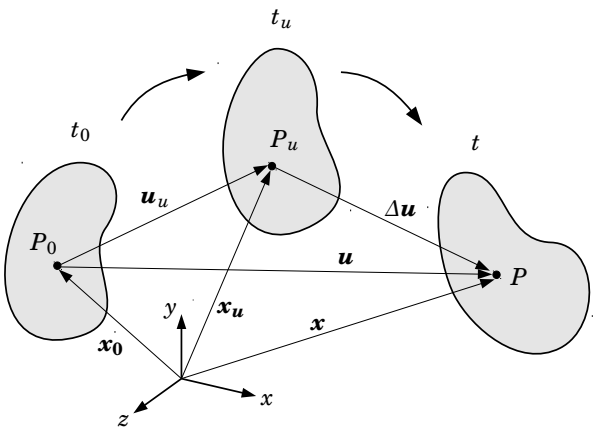

Figure 2.2: Motion of a continuum body at three different instants: initial t_0, arbitrary intermediate (updated) t_u, and current t.

$d\boldsymbol{S} \approx d\boldsymbol{S}_0$. Then, the substitution of the constitutive relationships 2.21, 2.25 and 2.26 into the conservation laws leads to the final governing equations:

Uncoupled linear thermoelasticity with total displacement

$$\int_{V_0} \rho_0 c_E \frac{\partial T}{\partial t} dV_0 = \int_{S_0} k\nabla T \cdot \boldsymbol{n}_0 dS_0 + \int_{V_0} q_r dV_0 \,, \tag{2.35}$$

$$\begin{aligned} \int_{V_0} \rho_0 \ddot{\boldsymbol{u}} dV_0 = & \int_{S_0} \boldsymbol{n}_0 \cdot \left[\mu\nabla_0 \boldsymbol{u} + \mu(\nabla_0 \boldsymbol{u})^T + \lambda \mathrm{tr}(\nabla_0 \boldsymbol{u}) \boldsymbol{I} \right] dS_0 \\ & - \int_{S_0} \boldsymbol{n}_0 \cdot [3K\alpha(T - T_0)\boldsymbol{I}] dS_0 \\ & + \int_{V_0} \rho_0 \boldsymbol{b} dV_0 \,. \end{aligned} \tag{2.36}$$

It is distinguished as *total displacement* because the unknown variable is always the displacement from the reference to the current configuration, $\boldsymbol{u}$. As can be seen on the right hand side of the linear momentum balance 2.36, the stress divergence becomes a function of the displacement gradient on the volume surface, with three terms: Laplacian, Laplacian transpose and trace.

On the other hand, when large displacements are involved, significant changes among continuum configurations are present and geometrical mapping relations should

be maintained. Instead of referring the integrals to the initial state (subscript 0), they may be rearranged into an arbitrary intermediate configuration, referred to as the updated configuration (subscript u), which is assumed to be known. Figure 2.2 shows the solid body at the three control states: initial, updated and current. As seen, $\boldsymbol{x} = \boldsymbol{x_u} + \Delta\boldsymbol{u}$, $\boldsymbol{u} = \boldsymbol{u}_u + \Delta\boldsymbol{u}$, and a new deformation tensor $\boldsymbol{f}$ can be defined to map from the updated domain to the current domain:

$$\begin{aligned}\boldsymbol{f} &= \frac{\partial \boldsymbol{x}}{\partial \boldsymbol{x_u}} = (\nabla_u \boldsymbol{x})^T \\ &= [\nabla_u (\boldsymbol{x_u} + \Delta\boldsymbol{u})]^T = \boldsymbol{I} + [\nabla_u (\Delta\boldsymbol{u})]^T \,.\end{aligned} \tag{2.37}$$

The total deformation gradient of the current state, can be obtained by a simple tensor dot product

$$\underbrace{\boldsymbol{F}}_{\frac{\partial \boldsymbol{x}}{\partial \boldsymbol{x_0}}} = \underbrace{\boldsymbol{f}}_{\frac{\partial \boldsymbol{x}}{\partial \boldsymbol{x_u}}} \cdot \underbrace{\boldsymbol{F}_u}_{\frac{\partial \boldsymbol{x_u}}{\partial \boldsymbol{x_0}}}, \tag{2.38}$$

where $\boldsymbol{F}_u$ is the deformation gradient at the previous updated instant t_u. Integrating over this updated configuration results in the so called updated Lagrangian formulation of the governing equations, whose final form is:

Updated Lagrangian hyperelasticity with incremental displacement

$$\rho_u = \rho j \,, \tag{2.39}$$

$$\int_{V_u} \rho_u \frac{\partial^2 (\boldsymbol{u}_u + \Delta\boldsymbol{u})}{\partial t^2} dV_u = \int_{S_u} \left(j \boldsymbol{f}^{-T} \cdot \boldsymbol{n}_u \right) \cdot \boldsymbol{\sigma} dS_u + \int_{V_u} \rho_u \boldsymbol{b} dV_u \,, \tag{2.40}$$

where $j = \det(\boldsymbol{f})$ and $\boldsymbol{\sigma}(\boldsymbol{u}_u + \Delta\boldsymbol{u})$ depend on the incremental displacement $\Delta\boldsymbol{u}$, which becomes the dependent variable. As mentioned before, temperature variation has not been considered with large deformations. There are two sources of nonlinearities: the strain-stress relation (as was seen in Saint Venant-Kirchhoff and neo-Hookean models), and in the spatial integration of stresses. The use of an updated Lagrangian approach and the incremental displacement for large deformations generally gives superior robustness in numerical tests when compared with a total Lagrangian method [24], which is always referred to the original configuration.

2.6 System discretisation

The continuum body is divided into a finite number of arbitrary convex polyhedral cells which fill the entire domain without mutual overlapping. The governing equations are directly integrated on each cell control volume, thereby solving the strong form of the conservation laws. This allows for obtaining a conservative formulation both locally (cell) and globally (region of cells and whole body).

Only the numerical methods associated with mass and momentum conservation will be described here since they represent the new contribution of the present work. Details about the implemented discretisation schemes for the heat equation were provided in [58].

The dependent variable of the remaining system, the displacement $\boldsymbol{u}$ or $\Delta\boldsymbol{u}$, is evaluated discretely in the centre of the cells, as well as in the centroid of the cell faces which belong to the domain boundary so that boundary conditions can be easily incorporated. In this manner, a cell-centred displacement-based finite volume method is followed. The term *node* will be used to indiscriminately reference the centre of a cell or a boundary face. On the other hand, discrete values of density are stored in the cell centres and the gradient of the displacement, and naturally, deformation and stress measures, are calculated directly on all face centroids. The evaluation of the gradient on a face depends on the value of the displacement at the vertices. Therefore, a method to interpolate the displacement from the nodes to the vertices of the mesh should be defined.

This section summarises the method to discretise the system of elasticity equations. First, numerical schemes for the inertial term are presented. Then, two sections cover the vertex interpolation tool and the gradient discretisation needed for the stress divergence. Finally, an explanation of how to implement the remaining terms and the boundary conditions is given.

2.6.1 Temporal discretisation

Time is discretised in a finite number of instants, where the balance laws are satisfied and solved sequentially. Hence, the resolution of equilibrium at time t^{n+1} is preceded by the already calculated solution at time t^n, both separated by a time increment $\Delta t^{n+1} = t^{n+1} - t^n$. Momentum equation is solved by applying a direct implicit time integration, i.e. all terms (inertial forces, surface forces and body forces) are evaluated at the current instant t^{n+1}, and thus their value is unknown.

The use of an implicit method is justified since the final purpose is to tackle engineering problems where the solid is subjected to a thermo-mechanical interaction with a fluid. This involves a vibrating or a quasi-static response of the structure, which can be addressed with a significantly larger time step than that imposed by the explicit methods [59]. The explicit approach is only suitable when a very small time step is needed to describe the physical problem, mainly in wave propagation scenarios. Furthermore, when applied to solid and fluid in an coupled problem, explicit schemes might establish a more severe restriction on the time step in the former than in the latter [2]. In particular, for the solid, the time increment is limited to

$$\Delta t \leqslant \Delta t_{cr} = \frac{2}{\omega_{max}}, \tag{2.41}$$

where Δt_{cr} is the critical size and ω_{max} is the highest natural frequency of the discretised solid. Normally, this maximum frequency is merely estimated by [60]

$$\omega_{max} = \frac{2}{L_{min}}\sqrt{\frac{E}{\rho}}, \tag{2.42}$$

where L_{min} is the minimum distance between nodes. The Courant number is defined as the ratio $C = \Delta t/\Delta t_{cr}$ and is commonly used as a measure of the time step size also with implicit methods, although they do not depend on it to be stable.

The numerical approximation of the inertial term of the momentum equation (2.36 and 2.40) assumes both density and acceleration at the node P to be the average value over the cell volume so that

$$\int_{V_0} \rho_0 \ddot{\boldsymbol{u}} dV_0 = \rho_{0P} V_{0P} \ddot{\boldsymbol{u}}_P^{n+1}, \tag{2.43}$$

where the acceleration is computed as a function of the new displacement $\boldsymbol{u}_P^{n+1}$ and past kinematics, according to the schemes described below.

When considering hyperelastic materials, the equilibrium is integrated over the updated configuration, which always will refer to the geometry at the previous instant t^n. Thus, after finding the new solution at time t^{n+1}, mesh is updated accordingly for the next time step. Besides, $\boldsymbol{u} = \boldsymbol{u}_u + \Delta\boldsymbol{u}$ becomes $\boldsymbol{u}^{n+1} = \boldsymbol{u}^n + \Delta\boldsymbol{u}$, and it is straightforward to find the equivalent formula of the inertia in terms of the incremental displacement.

Euler scheme Euler time scheme is the most extended scheme within cell-centred finite volume frameworks (see for instance [19,21,24,47]). It is first-order accurate and suffers

from numerical dissipation with large time increments. The second derivative of the displacement results in

$$\ddot{\boldsymbol{u}}^{n+1} = \frac{\dot{\boldsymbol{u}}^{n+1} - \dot{\boldsymbol{u}}^{n}}{\Delta t} = \frac{1}{\Delta t^2}\boldsymbol{u}^{n+1} - \frac{1}{\Delta t^2}\boldsymbol{u}^{n} - \frac{1}{\Delta t}\dot{\boldsymbol{u}}^{n}, \tag{2.44}$$

where all $\Delta t = \Delta t^{n+1}$.

Trapezoidal rule The trapezoidal rule belongs to the family of Newmark's schemes [61] and discretises the acceleration in the following manner:

$$\ddot{\boldsymbol{u}}^{n+1} = 2\frac{\dot{\boldsymbol{u}}^{n+1} - \dot{\boldsymbol{u}}^{n}}{\Delta t} - \ddot{\boldsymbol{u}}^{n} = \frac{4}{\Delta t^2}\boldsymbol{u}^{n+1} - \frac{4}{\Delta t^2}\boldsymbol{u}^{n} - \frac{4}{\Delta t}\dot{\boldsymbol{u}}^{n} - \ddot{\boldsymbol{u}}^{n}, \tag{2.45}$$

where $\Delta t = \Delta t^{n+1}$. It is one of the most commonly used schemes in finite element [62] and vertex-centred finite volume formulations [7, 8] because it is second-order accurate and shows limited integration errors [2] (classified as period elongation and amplitude decay in vibration analysis). The work developed by [63] included the trapezoidal rule in a cell-centred finite volume solver.

Three-point Euler backward scheme This scheme uses information from two previous instants to estimate the current acceleration as

$$\begin{aligned} \ddot{\boldsymbol{u}}^{n+1} &= c_1\dot{\boldsymbol{u}}^{n-1} + c_2\dot{\boldsymbol{u}}^{n} + c_3\dot{\boldsymbol{u}}^{n+1} \\ &= c_1\dot{\boldsymbol{u}}^{n-1} + c_2\dot{\boldsymbol{u}}^{n} + c_1c_3\boldsymbol{u}^{n-1} + c_2c_3\boldsymbol{u}^{n} + c_3c_3\boldsymbol{u}^{n+1}. \end{aligned} \tag{2.46}$$

The coefficients are affected by the time step sizes Δt^n and Δt^{n+1}:

$$c_1 = \frac{1-\gamma}{\Delta t^n}, \qquad c_2 = \frac{-1}{\gamma\Delta t^{n+1}}, \qquad c_3 = \frac{2-\gamma}{\Delta t^{n+1}}, \tag{2.47}$$

where $\gamma = \Delta t^n/\left(\Delta t^n + \Delta t^{n+1}\right)$. This second-order time scheme was used along with the finite volume method in [17], and can show numerical damping, as the first-order Euler.

Bathe method The finite element community has contemplated composite implicit methods for structural dynamics because of their low integration errors and stability in nonlinear analysis [64]. None example of using such an approach within finite volume formulations has been found in the literature. In the Bathe composite method [48, 49] the time step Δt^{n+1} is divided into two sub-steps, and each of them is solved with a

different scheme: the first with the trapezoidal rule (equation 2.45) and the second with the three-point Euler backward scheme (equation 2.46). As highlighted by [62], if the first sub-step corresponds to $\left(2-\sqrt{2}\right)\Delta t^{n+1}$, both schemes define the same coefficient multiplying $\boldsymbol{u}^{n+1}$. Thus, the same system matrix can be used within both sub-steps if there is a total Lagrangian description.

2.6.2 Vertex interpolation

The interpolated displacement at the vertices is needed, first, to calculate the gradient of displacement on the faces, and second, to move the mesh if an updated Lagrangian approach is considered. The formula to interpolate any variable ϕ in a vertex V will be a linear combination of the node values ϕ_i surrounding this vertex:

$$\phi_V = \frac{\sum_i w_i \phi_i}{\sum_i w_i} = \sum_i \omega_i \phi_i \,, \tag{2.48}$$

where ω_i is the final weight corresponding to every neighbouring node. The compact stencil of nodes associated with a vertex is outlined in figure 2.3 (left). A lightweight technique to measure the contribution of each node is through its distance to the vertex as

$$w_i = \frac{1}{d_i} \,, \tag{2.49}$$

where $d_i = |\boldsymbol{x}_V - \boldsymbol{x}_i|$. While this inverse distance interpolation is first-order accurate for non-orthogonal grids, it preserves the positivity of the weighting coefficients and always provides a bounded interpolated value [65]. Second-order accuracy can be achieved by using the modified inverse distance interpolation developed by [46]. The weight is a function of the Lagrange multipliers $\boldsymbol{\lambda} = \left(\lambda_x, \lambda_y, \lambda_z\right)$ and the vertex-node distance in the following manner:

$$w_i = \frac{\boldsymbol{\lambda} \cdot \boldsymbol{r}_i}{d_i} \,, \tag{2.50}$$

where $\boldsymbol{r}_i = (\boldsymbol{x}_V - \boldsymbol{x}_i)/d_i$ is a unit vector. The Lagrange multipliers of a vertex are obtained by solving a 3×3 system of equations, which can be written in the matrix form:

$$\begin{bmatrix} \sum r_{xi}{}^2 & \sum r_{xi} r_{yi} & \sum r_{xi} r_{zi} \\ \sum r_{xi} r_{yi} & \sum r_{yi}{}^2 & \sum r_{yi} r_{zi} \\ \sum r_{xi} r_{zi} & \sum r_{yi} r_{zi} & \sum r_{zi}{}^2 \end{bmatrix} \begin{bmatrix} \lambda_x \\ \lambda_y \\ \lambda_z \end{bmatrix} = - \begin{bmatrix} \sum r_{xi} \\ \sum r_{yi} \\ \sum r_{zi} \end{bmatrix} . \tag{2.51}$$

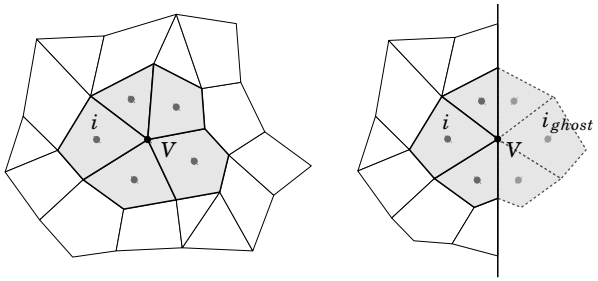

Figure 2.3: Stencil (shaded cells) of an inner vertex (left) and a symmetry boundary vertex (right).

The linear system is solved here with the explicit equation derived from Cramer's rule. Compared with a second-order least-squares interpolation, which assembles a 4×4 system of equations for each vertex [66], this method requires substantially less computational effort. Its disadvantage is that it does not guarantee the positivity of the coefficients, although the original authors proved it to be robust for a wide range of cases.

The interpolation at the boundary vertices is altered if the boundary condition is Dirichlet or a symmetry plane. In the Dirichlet case, the vertex is given the average displacement of the surrounding boundary faces. In the symmetry case, the cells touching the symmetry plane are mirrored at the other side of the surface to enlarge the stencil (see figure 2.3 right), similarly to [65].

2.6.3 Face gradient

The closed integral of the surface forces acting on a cell depends on the gradient of the displacement on its faces, as shown in section 2.5. The integral is approximated on each face by the midpoint rule, resulting in the following general strategy:

$$\int_S \nabla\phi dS = \sum_f \left(\int_{S_f} \nabla\phi dS_f \right) \approx \sum_f (\nabla\phi)_f S_f \tag{2.52}$$

Now the question is how this gradient at the face centroid will be evaluated. In this work, the gradient is computed directly at the face, instead of estimating it at the cell centres and interpolating later its value to the face. By doing so, the required stencil of nodes is shrunk and the accuracy improves [43, 47].

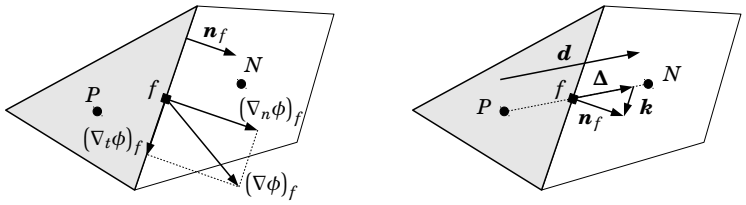

Figure 2.4: Cell P and a neighbour cell N sharing the face f. Decomposition of the gradient on the face (left) and geometrical relations for the orthogonal component of the gradient (right).

The face gradient of any scalar or vector field is decomposed into normal and tangential components to the surface,

$$(\nabla\phi)_f = (\nabla_n\phi)_f + (\nabla_t\phi)_f \,, \tag{2.53}$$

and each one is discretised separately. Figure 2.4 (left) depicts the mentioned decomposition. This approach was used in [47] to measure more accurately the elastic reaction at a multi-material interface, avoiding checkerboard patterns in the numerical solution. The authors from [43] generalised this method for all the cell faces of the computational domain, as performed here.

To calculate the face tangential derivative, the surface Gauss theorem is employed. It relates a surface integral to a line integral as follows [67]:

$$\int_S \nabla_t\phi dS = \int_{\partial S} \boldsymbol{m}\phi dL \,, \tag{2.54}$$

where $\boldsymbol{m}$ is the unit vector perpendicular to ∂S and tangential to surface S, which is assumed to be flat. Therefore, the tangential component at the face centroid can be approximated again by the midpoint rule integrating through all face edges e as

$$(\nabla_t\phi)_f \approx \frac{1}{S}\sum_e L_e \boldsymbol{m}_e \phi_e \,. \tag{2.55}$$

An edge segment is defined from vertex V_1 to vertex V_2, as can be seen in figure 2.5. In this way, $L_e = |V_2 - V_1|$, $\boldsymbol{e} = (V_2 - V_1)/L_e$, $\boldsymbol{m}_e = \boldsymbol{e} \times \boldsymbol{n}_f$ and ϕ_e is the field at the segment centre. The application of this numerical mechanism was proposed within the so called finite area method to evaluate initially the tangential derivatives in multiphase flows [67] and more recently in shallow flows [68].

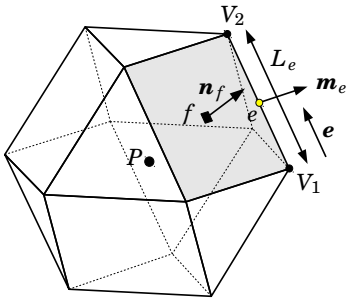

Figure 2.5: Polyhedral control volume with centroid P. Shaded face with centroid f has an edge segment e which is defined from vertex V_1 to vertex V_2.

The variable at the edge ϕ_e can be obtained by averaging the value in the extreme vertices V_1 and V_2. Since vertex values are interpolated according to expression 2.48, the equation 2.55 can be written as a function of the node values as:

$$\begin{aligned}\left(\nabla_t \phi\right)_f &\approx \frac{1}{S}\sum_e L_e \boldsymbol{m}_e \frac{\phi_{V_1}+\phi_{V_2}}{2} \\ &\approx \frac{1}{2S}\sum_e \left(L_e \boldsymbol{m}_e \sum_{i_{1,2}} \omega_i \phi_i \right),\end{aligned} \tag{2.56}$$

where the summation $\sum_{i_{1,2}}$ adds the nodal contributions of both vertices. Like the vertex interpolation, this numerical scheme is exact for linear polynomials.

The discretisation of the face normal derivative is based on the over-relaxed approach from [69]:

$$\begin{aligned}\left(\nabla_n \phi\right)_f &= \boldsymbol{n}_f \left[\boldsymbol{n}_f \cdot \left(\nabla \phi\right)_f \right] \\ &\approx \boldsymbol{n}_f \left[|\boldsymbol{\Delta}| \frac{\phi_N - \phi_P}{|\boldsymbol{d}|} + \boldsymbol{k} \cdot \left(\nabla_t \phi\right)_f \right],\end{aligned} \tag{2.57}$$

where P and N are the nodes sharing the face, and $\boldsymbol{n}_f$ is pointing to N, as can be seen in figure 2.4 (right). The geometrical relations are: $\boldsymbol{d} = \boldsymbol{x}_N - \boldsymbol{x}_P$, $\boldsymbol{\Delta} = \boldsymbol{d}/(\boldsymbol{d}\cdot\boldsymbol{n})$ and $\boldsymbol{k} = \boldsymbol{n} - \boldsymbol{\Delta}$. The selected vector $\boldsymbol{k}$ is tangent to the face, allowing for evaluating the non-orthogonal correction with $\left(\nabla_t \phi\right)_f$ instead of with the total face gradient. As a result, expression 2.56 can be used to obtain the explicit equation of the normal gradient in terms of the

node values:

$$\left(\nabla_n \phi\right)_f \approx \boldsymbol{n}_f \left\{ |\boldsymbol{\Delta}| \frac{\phi_N - \phi_P}{|\boldsymbol{d}|} + \boldsymbol{k} \cdot \left[\frac{1}{2S} \sum_e \left(L_e \boldsymbol{m}_e \sum_{i_{1,2}} \omega_i \phi_i \right) \right] \right\} . \tag{2.58}$$

This scheme provides second-order accurate approximation at inner faces, even though the accuracy could drop if highly skewed elements and non-centred faces are present.

2.6.4 Body force, temperature load and density

The discretised body force of equation 2.36 gets the following form:

$$\int_{V_0} \rho_0 \boldsymbol{b} dV_0 \approx \rho_{0P} \boldsymbol{b}_P V_{0P} . \tag{2.59}$$

The same term in equation 2.40 is approximated identically but considering the updated geometry, instead of the initial configuration.

The surface integral of the temperature load in the thermoelastic momentum equation 2.36 results in

$$\int_{S_0} \boldsymbol{n}_0 \cdot [3K\alpha(T - T_0)\boldsymbol{I}] dS_0 \approx \sum_f 3K_f \alpha_f \left(T_f - T_{0f}\right) S_{0f} \boldsymbol{n}_{0f} , \tag{2.60}$$

where values of K, α and temperature at the faces are linearly interpolated from their value at the nodes.

Mass conservation of equation 2.39 asks for updating the density after every time iteration, and is performed directly at the cell centres as

$$\rho_P = \frac{\rho_{uP}}{j_P} \quad \text{or} \quad \rho_P^{n+1} = \frac{\rho_P^n}{j_P} , \tag{2.61}$$

where the Jacobian at the cell centroid j_P, which is a function of the displacement gradient tensor, is averaged from the cell faces.

2.6.5 Boundary conditions

Three types of boundary conditions, which determine the governing equation of a boundary node B, are considered:

- Known displacement (Dirichlet): $\boldsymbol{u}_B = \boldsymbol{U}$.

- Zero normal gradient of the displacement (Neumann): $\boldsymbol{n}_B \cdot (\nabla \boldsymbol{u})_B = \boldsymbol{0}$. Following the numerical method for the normal derivative (equation 2.57), the resulting discretised formula is

$$|\boldsymbol{\Delta}| \frac{\boldsymbol{u}_B - \boldsymbol{u}_N}{|\boldsymbol{d}|} + \boldsymbol{k} \cdot (\nabla_t \boldsymbol{u})_B = \boldsymbol{0}. \tag{2.62}$$

- Known external load:

$$\int_{S_B} \boldsymbol{n} \cdot \boldsymbol{\sigma} dS_B = \int_{S_B} \boldsymbol{T} dS_B, \tag{2.63}$$

  where the mechanical load $\boldsymbol{T}$ can be defined from a traction $\boldsymbol{t}$ and a pressure p, so that the final force applied on the boundary face is:

$$\int_{S_B} \boldsymbol{T} dS_B = \boldsymbol{t} S_B - p \boldsymbol{n}_B S_B = \boldsymbol{t} |\boldsymbol{S}_B| - p \boldsymbol{S}_B, \tag{2.64}$$

  where $\boldsymbol{S}_B$ is the surface outward vector in the current configuration. When considering small deformations $\boldsymbol{S}_B$ can be approximated by $\boldsymbol{S}_{0B}$, but if large deformations are involved, it should be evaluated by means of Nanson's formula 2.5. The discretisation of the left hand side of equation 2.63 can be deduced from the gradient discretisation described in section 2.6.3.

A symmetry plane is represented as a Dirichlet condition in the normal component of the displacement and a Neumann condition in the tangential directions.

2.7 System resolution

After substituting all terms featuring in the linear momentum equation by their discretised counterparts, an algebraic equation can be assembled over all control volumes and boundary faces. Each equation relates the value of the dependent variable $\boldsymbol{u}$ or $\Delta \boldsymbol{u}$ in the centroid P with its value at the neighbouring nodes N,

$$\mathbf{a}_P \cdot \boldsymbol{u}_P + \sum_N \mathbf{a}_N \cdot \boldsymbol{u}_N = \mathbf{b}_P, \tag{2.65}$$

where $\mathbf{a}$ are tensor linear coefficients and vector $\mathbf{b}_P$ incorporates both source terms and nonlinear terms.

This section is dedicated to describe the two approaches that have been implemented to solve the above system of equations, both focused on accelerating the solution convergence of the classical segregated method.

2.7.1 Accelerated segregated method

In the case of linear elasticity, as was seen in equation 2.36, the stress divergence includes three terms that depend on the displacement, in order: Laplacian, Laplacian transpose and trace. This introduces a dependency among the three components of the displacement. The segregated algorithm approximates the stress terms as a pure diffusive contribution which is evaluated implicitly within the linear system, and a deferred correction is responsible then for assigning the right value of the stresses. In this manner, outer fixed-point iterations are needed to solve the momentum equilibrium until the converged stresses are reached. The formulation of both implicit and deferred correction parts can be distinguished here:

$$\begin{aligned}\int_{S_0} \boldsymbol{n}_0 \cdot \boldsymbol{\sigma} dS_0 = \int_{S_0} \mathscr{Y}_{\text{imp}} \boldsymbol{n}_0 \cdot \nabla_0 \boldsymbol{u} dS_0 \quad &\leftarrow \text{Implicit} \\ + \int_{S_0} \boldsymbol{n}_0 \cdot \left[\boldsymbol{\sigma} - \mathscr{Y}_{\text{imp}} \nabla_0 \boldsymbol{u}\right] dS_0 \quad &\leftarrow \text{Correction}\end{aligned} \tag{2.66}$$

The implicit term is evaluated based on the orthogonal contribution of equation 2.57. The non-orthogonal correction of that same equation, along with the deferred correction of equation 2.66, are computed explicitly with the displacements from the previous outer iteration. Such an arrangement of the surface integral allows for moving the inter-component dependencies to the source term of the system and, as a result, for decoupling the global system into three smaller systems, one for each direction $\mathsf{i} = x, y, z$:

$$[\mathsf{A}_\mathsf{i}] \cdot [\mathsf{u}_\mathsf{i}] = [\mathsf{b}_\mathsf{i}] \,, \tag{2.67}$$

where $[\mathsf{u}_\mathsf{i}]$ is the vector that contains the solution of the specific displacement component. The resulting coefficient matrix $[\mathsf{A}_\mathsf{i}]$ is based on transient and Laplacian terms and, therefore, is sparse, symmetric and diagonally dominant. Moreover, the implicit part of boundary node equations becomes very simple and they can be easily extracted from the matrix system, leading to a system size of $N_c \times N_c$, where N_c is the number of cells.

The magnitude of the scalar $\mathscr{Y}_{\text{imp}}$ from equation 2.66 does not determine the final solution but affects the convergence speed of the iterative process. According to [13], the optimal value, based on the minimisation of the required stress correction in linear elasticity, is $\mathscr{Y}_{\text{imp}} = \left(2\mu + \lambda\right)$.

When considering nonlinear elastic problems, the segregation of the system is performed naturally in the same way, although now the deferred correction incorporates

additionally the nonlinear terms,

$$\int_{S_u}\left(j\boldsymbol{f}^{-T}\cdot\boldsymbol{n}_u\right)\cdot\boldsymbol{\sigma}\,dS_u=\int_{S_u}\mathscr{Y}_{\text{imp}}\boldsymbol{n}_u\cdot\nabla_u(\Delta\boldsymbol{u})\,dS_u + \int_{S_u}\left(j\boldsymbol{f}^{-T}\cdot\boldsymbol{n}_u\right)\cdot\boldsymbol{\sigma}\,dS_u-\int_{S_u}\mathscr{Y}_{\text{imp}}\boldsymbol{n}_u\cdot\nabla_u(\Delta\boldsymbol{u})\,dS_u\,, \tag{2.68}$$

where the implicit stiffness $\mathscr{Y}_{\text{imp}}$ is set as in the linear elastic case, because it was found to provide convergence for hyperelasticity [17] and finite strain elastoplasticity [24]. The variable is the incremental displacement, hence the next form of the matrix system

$$[\mathsf{A}_\mathsf{i}]\cdot[\Delta\mathsf{u}_\mathsf{i}]=[\mathsf{b}_\mathsf{i}]\,. \tag{2.69}$$

The segregated approach is commonly used with cell-centred finite volume structural methods. Early [12, 13] and up-to-date [22, 24, 41] work examples can be found in the literature. While the final segregated algorithm is robust and uses low computer memory, it can experience slow convergence rates when there is strong coupling between displacement directions. For this reason, two different techniques are proposed to speedup the computational performance: a sequence acceleration for the outer fixed-point iterations and a predictor step to extrapolate the solution at an instant and get an improved initial guess.

Aitken acceleration An Aitken Δ^2 technique aims at accelerating the solution convergence of the outer fixed-point iterations. The solution obtained after an outer iteration $\mathsf{k}+1$ is accelerated following the multidimensional *Method 3* presented in [70]:

$$[\tilde{\mathsf{u}}]^{\mathsf{k}+1}=[\mathsf{u}]^{\mathsf{k}+1}+\gamma[\mathsf{r}]^{\mathsf{k}+1} \tag{2.70}$$

$$\gamma=\frac{[\mathsf{r}]^{\mathsf{k}+1}\cdot\left([\mathsf{r}]^{\mathsf{k}+1}-[\mathsf{r}]^{\mathsf{k}}\right)}{\left|[\mathsf{r}]^{\mathsf{k}+1}-[\mathsf{r}]\right|^2} \tag{2.71}$$

$$[\mathsf{r}]^{\mathsf{k}+1}=[\mathsf{u}]^{\mathsf{k}+1}-[\mathsf{u}]^{\mathsf{k}}\,, \tag{2.72}$$

where vectors $[\mathsf{u}]$ concatenate the solutions from all three directions. The same formula is applied to $[\Delta\tilde{\mathsf{u}}]^{\mathsf{k}+1}$. It has been found that applying this Aitken formula every five iterations provides a good convergence acceleration for the linear and nonlinear cases analysed in this work.

Predictor step The displacement solution is extrapolated before conducting the outer iterations in order to estimate better the stress term. Two numerical schemes have been added:

$$\boldsymbol{u}^{n+1} = \boldsymbol{u}^{n} + \dot{\boldsymbol{u}}^{n}\,\Delta t^{n+1}\,, \tag{2.73}$$

$$\boldsymbol{u}^{n+1} = \boldsymbol{u}^{n} + \frac{\Delta t^{n+1}}{2\Delta t^{n}}\left[\left(2\Delta t^{n} + \Delta t^{n+1}\right)\dot{\boldsymbol{u}}^{n} - \Delta t^{n+1}\dot{\boldsymbol{u}}^{n-1}\right], \tag{2.74}$$

the Euler and the two-step Adams-Bashforth with different step sizes, respectively.

The final segregated algorithm for the updated Lagrangian hyperelasticity can be described by the next sequence:

1. Set the time iterator count $n = 0$.
2. Provide initial values for all dependent variables.
3. Increase the time iterator count $n + 1$.
4. Set the momentum outer iteration $\mathsf{k} = 0$.
5. Evaluate the vertex interpolation weights ω_i according to the updated configuration at t^n.
6. Evaluate the nodal coefficients of matrices $[\mathsf{A_i}]^{n+1}$ taking into account the discretisation of inertial term, Laplacian term and boundary conditions on the updated configuration.
7. Initialise the linear solver based on matrix $[\mathsf{A_i}]^{n+1}$.
8. Set the displacement from the predictor step (equation 2.73 or 2.74) as an initial guess.
9. Increase the momentum outer iteration count $\mathsf{k} + 1$.
10. Update discretised face fields: $\nabla_u(\Delta\boldsymbol{u})$, $\boldsymbol{f}$, j, $\boldsymbol{F}$, J and $\boldsymbol{\sigma}$.
11. Update the source terms $[\mathsf{b_i}]^{\mathsf{k}+1}$ taking into account the discretisation of inertial term, body force and non-orthogonal and deferred corrections of stress.
12. Solve the linear system 2.69 to obtain $[\Delta\mathsf{u}]^{\mathsf{k}+1}$. A reduction in the residuals of two orders of magnitude is sufficient, since the source term is approximated from the previous iteration.

13. Accelerate the solution according to equation 2.70 if k is a multiple of five.

14. Evaluate the maximum system initial residual as

$$\frac{\left|[\mathsf{A_i}]^{n+1}\cdot[\Delta\mathsf{u_i}]^{\mathsf{k}}-[\mathsf{b_i}]^{\mathsf{k}+1}\right|}{\left|[\mathsf{b_i}]^{\mathsf{k}+1}\right|} \tag{2.75}$$

    and return to step 9 if it is greater than the momentum numerical tolerance.

15. Evaluate the node fields $\boldsymbol{u}^{n+1}$, $\dot{\boldsymbol{u}}^{n+1}$, $\ddot{\boldsymbol{u}}^{n+1}$ and ρ^{n+1}.

16. Move the mesh according to the interpolated vertex values of $\Delta\boldsymbol{u}_V^{n+1}$.

17. Advance the time by Δt^{n+1} and return to step 3 unless the prescribed final time is reached.

A similar algorithm is used for linear thermoelasticity. The main difference lies in the fact that there is no need to update the mesh and, as a result, the system matrix is unchanged throughout a transient simulation. Moreover, energy conservation should be solved before the linear momentum, whereas mass law can be ignored.

2.7.2 Block-coupled method

Unlike the segregated arrangement, this one does not decouple the linear contributions of all three displacement components but formulates them implicitly. This approach is followed by finite element analysis and has recently been presented as well along with cell-centred finite volume methods for linear elasticity [36, 43]. The result is a larger linear system of size $3N_n \times 3N_n$, where N_n is the total number of nodes:

$$[\mathsf{A}]\cdot[\mathsf{u}]=[\mathsf{b}]\,. \tag{2.76}$$

In addition, the system matrix becomes non-symmetric, less diagonally dominant and less sparse. The linear system is harder to solve, considering numerical stability and memory requirements. However, it can provide a higher convergence speed, as shown by the original authors and by most of the tests in chapter 3.

With linear thermoelasticity, the entire stress divergence term can be written implicitly and then the solution of the linear momentum balance (equation 2.36) can be obtained by a single resolution of a matrix system. The first step consists on decomposing

the surface traction into normal and tangential components [30, 43, 47]:

$$\begin{aligned}\int_{S_0} \boldsymbol{n}_0 \cdot \boldsymbol{\sigma} dS_0 = &\int_{S_0} \left[(2\mu+\lambda)\, \boldsymbol{n}_0 \cdot \nabla_0 \boldsymbol{u}_n + \lambda \boldsymbol{n}_0 \mathrm{tr}(\nabla_{0t} \boldsymbol{u}_t) \right] dS_0 \quad \leftarrow \text{ Normal} \\ &+ \int_{S_0} \left[\mu \boldsymbol{n}_0 \cdot \nabla_0 \boldsymbol{u}_t + \mu \nabla_{0t} u_n \right] dS_0 \quad \leftarrow \text{ Tangential} \\ &- \int_{S_0} \boldsymbol{n}_0 \cdot [3K\alpha(T-T_0)\boldsymbol{I}] dS_0 \end{aligned} \tag{2.77}$$

where $\boldsymbol{u}_n = \boldsymbol{n}_0 \boldsymbol{n}_0 \cdot \boldsymbol{u}$, $\boldsymbol{u}_t = (\boldsymbol{I} - \boldsymbol{n}_0 \boldsymbol{n}_0) \cdot \boldsymbol{u}$, $u_n = \boldsymbol{n}_0 \cdot \boldsymbol{u}$, and tensor $\boldsymbol{n}_0 \boldsymbol{n}_0$ results from the dyadic product of normal vector. The surface tangential derivatives of any variable ϕ are equivalent to $\nabla_{0t}\phi = (\boldsymbol{I} - \boldsymbol{n}_0 \boldsymbol{n}_0) \cdot \nabla_0 \phi$. Having this more suitable form facilitates the implicit formulation of the stress term. Normal derivatives to the surface ($\boldsymbol{n}_0 \cdot \nabla_0 \boldsymbol{u}_n$ and $\boldsymbol{n}_0 \cdot \nabla_0 \boldsymbol{u}_t$) are approximated by means of equation 2.58, whereas tangential derivatives ($\boldsymbol{n}_0 \mathrm{tr}(\nabla_{0t} \boldsymbol{u}_t)$ and $\nabla_{0t} u_n$) employ equation 2.56. Of course there is some algebraic effort needed to obtain the final reduced expressions as linear functions of the node displacements. The reader is referred to [43] for more details about the final form of the linear coefficients.

In this work, the block-coupled procedure has only been implemented yet for linear thermoelasticity. While the segregated approach extends naturally to hyperelasticity, because nonlinear terms can be added without changing the iterative resolution algorithm, the block-coupled method would require outer iterations and Newton-type methods to find the solution efficiently, as underlined by [43].

Structural damping The similarities between the block-coupled method and the finite element method concerning the system arrangement allow for considering the structural damping within a finite volume discretisation.

The basic energy-loss mechanisms are rarely fully understood, and hence difficult to characterise and model numerically. Thus, taking into account computational conveniences, an equivalent viscous-damping property is defined from experimental methods so that the finite element system is represented as [2, 71]:

$$[\mathsf{M}] \cdot [\ddot{\mathsf{u}}] + [\mathsf{C}] \cdot [\dot{\mathsf{u}}] + [\mathsf{K}] \cdot [\mathsf{u}] = [\mathsf{R}], \tag{2.78}$$

where [M] is the global mass matrix, [K] the global stiffness matrix and [R] the load vector. The proportional damping matrix [C] is generally built from mass and stiffness matrices as follows

$$[\mathsf{C}] = \alpha_R [\mathsf{M}] + \beta_R [\mathsf{K}]. \tag{2.79}$$

It corresponds to a kind of damping modelling known as Rayleigh damping, which is determined by two scalars α_R and β_R. They are derived from the next formula for the damping ratio of a particular mode m:

$$\zeta_m = \frac{1}{2}\left(\frac{\alpha_R}{\omega_m} + \beta_R \omega_m\right), \tag{2.80}$$

where ω_m is the angular frequency of mode m. The parameters can be obtained thanks to the pair data from two different modes.

When considering a finite volume methodology, the mass matrix would be identically a diagonal matrix with the mass of every element. For the specific case of the block-coupled approach, the coefficients of the matrix [K] can be analogously extracted from the implicit discretisation of the stress divergence (equation 2.77). In this way, equation 2.79 can be applied, and Rayleigh damping forces can be added to the system. If for instance the trapezoidal rule is used to model the velocity, the matrix and source term of the finite volume system should change according to:

$$[\mathsf{A}] \mathrel{+}= \frac{2}{\Delta t^{n+1}}[\mathsf{C}], \tag{2.81}$$

$$[\mathsf{b}] \mathrel{+}= [\mathsf{C}] \cdot \left(\frac{2}{\Delta t^{n+1}}[\mathsf{u}]^n + [\dot{\mathsf{u}}]^n\right). \tag{2.82}$$

If only mass proportional damping is pursued:

$$\zeta_m = \frac{\alpha_R}{2\omega_m}, \tag{2.83}$$

$$[\mathsf{C}] = \alpha_R [\mathsf{M}], \tag{2.84}$$

and, therefore, damping modelling becomes much simpler and can be also implemented without difficulties within the segregated method.

2.8 Parallelisation

The model presented in this chapter has been integrated into TermoFluids software [45], which is composed of parallel libraries for the mesh geometry, linear solvers and fluid physics. The finite volume method for structures shares the same programming and execution pattern as the flow methods, also from the parallelisation point of view. Their design is based on the distributed memory paradigm [72]: each computing process has exclusive access to its memory portion, and a message-passing is performed to

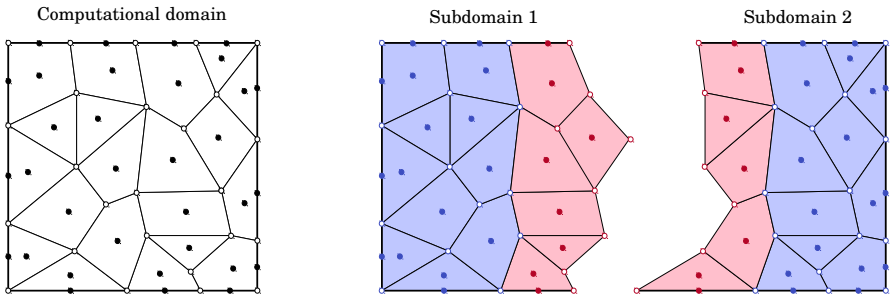

Figure 2.6: Discretised domain (left) and its decomposition between two MPI processes (right). Cell and boundary nodes are represented as filled circles and vertices as empty circles. In blue the owned elements and in red the halo elements of each process.

exchange data among processes and work together. This exchange is implemented using the Message Passing Interface (MPI) standard, making the code portable across all distributed memory systems.

The computational domain is decomposed into subdomains (with the same weight of node calculations) so that each processor handles a different one. The information required by a processor from the adjacent elements of other processor is stored in halo elements. Consequently, two different types of nodes exist: those solved in the processor (owned) and those updated from adjacent processors (halo).

Regarding the solid case, and particularly the vertex interpolation procedure, halo nodes should include all neighbouring nodes which share a vertex with owned nodes, as depicted in figure 2.6. This means halo cell nodes but also halo boundary nodes. Besides, owned/halo classification should be maintained for the grid vertices. First, because every owned vertex needs ϕ_i value at every neighbouring node. And second, because, in case of moving the mesh, halo vertices will allow updating as well the halo cells to their new configuration.

All structural simulations carried out in this work have been conducted using the parallel PETSc solvers [73, 74], whose libraries are linked with those of TermoFluids code.

2.9 Summary

This chapter is dedicated to describing a parallel three-dimensional finite volume method for elastic materials and unstructured computational grids.

The fundamental conservation laws and constitutive equations are assembled in order to define a system with displacement and temperature as dependent variables. On the one hand, small strains and quasi-static thermal effects are assumed to define the uncoupled linear thermoelastic model. Energy and linear momentum equations can be integrated and solved with respect to the initial configuration. On the other hand, the hyperelastic models, namely the Saint Venant-Kirchhoff and neo-Hookean, are constructed with an updated Lagrangian formulation and an incremental analysis aiming at materials which undergo large deformations and negligible thermal loads. Mass and momentum balances are referred to the updated geometry.

Spatial discretisation of the governing equations is performed by fully conservative second-order schemes, which are cell-centred and derived from a linear distribution of variables and the midpoint rule. Direct implicit time integration schemes promote stability when dealing with vibration cases and large time step sizes. The resulting discretised system is arranged in two different fashions, which focus on accelerating the solution convergence: the segregated approach with an Aitken method and a transient predictor step, and the block-coupled method. The analogy of the latter with the displacement-based finite element system allows for mimicking the Rayleigh viscous damping model within a finite volume analysis.

References

[1] T. J. R. Hughes. *The Finite Element Method: Linear Static and Dynamic Finite Element Analysis*. Prentice-Hall, 1987.

[2] K.-J. Bathe. *Finite Element Procedures*. Prentice Hall, 1996.

[3] Y. D. Fryer, C. Bailey, M. Cross, and C. H. Lai. A control volume procedure for solving the elastic stress-strain equations on an unstructured mesh. *Applied Mathematical Modelling*, 15(11):639 – 645, 1991.

[4] E. Oñate, M. Cervera, and O. C. Zienkiewicz. A finite volume format for structural mechanics. *International Journal for Numerical Methods in Engineering*, 37(2):181–201, 1994.

[5] C. Bailey and M. Cross. A finite volume procedure to solve elastic solid mechanics problems in three dimensions on an unstructured mesh. *International Journal for Numerical Methods in Engineering*, 38(10):1757–1776, 1995.

[6] G. A. Taylor, C. Bailey, and M. Cross. Solution of the elastic/visco-plastic constitutive equations: A finite volume approach. *Applied Mathematical Modelling*, 19(12):746 – 760, 1995.

[7] A. K. Slone, C. Bailey, and M. Cross. Dynamic solid mechanics using finite volume methods. *Applied Mathematical Modelling*, 27(2):69–87, 2003.

[8] M. Aguirre, A. J. Gil, J. Bonet, and A. A. Carreño. A vertex centred finite volume Jameson–Schmidt–Turkel (JST) algorithm for a mixed conservation formulation in solid dynamics. *Journal of Computational Physics*, 259:672 – 699, 2014.

[9] I. Demirdžić, D. Martinović, and A. Ivanković. Numerical simulation of thermal deformation in welded workpiece (in Croatian). *Zavarivanje*, 31:209 – 219, 1988.

[10] S. B. Beale and S. R. Elias. Numerical solution of two-dimensional elasticity problems by means of a "SIMPLE"-based finite-difference scheme, TR-LT-020. Technical report, NRCC, Institute for Mechanical Engineering, Ottawa, 1991.

[11] J. H. Hattel and P. N. Hansen. A control volume-based finite difference method for solving the equilibrium equations in terms of displacements. *Applied Mathematical Modelling*, 19(4):210 – 243, 1995.

[12] I. Demirdžić and S. Muzaferija. Finite volume method for stress analysis in complex domains. *International Journal for Numerical Methods in Engineering*, 37(21):3751–3766, 1994.

[13] H. Jasak and H. G. Weller. Application of the finite volume method and unstructured meshes to linear elasticity. *International Journal for Numerical Methods in Engineering*, 48(2):267–287, 2000.

[14] I. Demirdžić and D. Martinović. Finite volume method for thermo-elasto-plastic stress analysis. *Computer Methods in Applied Mechanics and Engineering*, 109(3):331 – 349, 1993.

[15] K. Maneeratana. *Development of the finite volume method for non-linear structural applications*. PhD thesis, Imperial College London (University of London), 2000.

[16] C. J. Rente and P. J. Oliveira. Extension of a finite volume method in solid stress analysis to cater for non-linear elastoplastic effects. In *EM2000 14th Engineering Mechanics Conference*, Austin, 2000.

[17] Ž. Tuković and H. Jasak. Updated lagrangian finite volume solver for large deformation dynamic response of elastic body. *Transactions of FAMENA*, 31:1–18, 2007.

[18] P. Cardiff, A. Karač, and A. Ivanković. A large strain finite volume method for orthotropic bodies with general material orientations. *Computer Methods in Applied Mechanics and Engineering*, 268:318 – 335, 2014.

[19] I. Demirdžić, E. Džaferović, and A. Ivanković. Finite-volume approach to thermo-viscoelasticity. *Numerical Heat Transfer, Part B: Fundamentals*, 47(3):213–237, 2005.

[20] I. Bijelonja, I. Demirdžić, and S. Muzaferija. A finite volume method for large strain analysis of incompressible hyperelastic materials. *International Journal for Numerical Methods in Engineering*, 64(12):1594–1609, 2005.

[21] I. Bijelonja, I. Demirdžić, and S. Muzaferija. A finite volume method for incompressible linear elasticity. *Computer Methods in Applied Mechanics and Engineering*, 195(44):6378 – 6390, 2006.

[22] I. Bijelonja, I. Demirdžić, and S. Muzaferija. Mixed finite volume method for linear thermoelasticity at all Poisson's ratios. *Numerical Heat Transfer, Part A: Applications*, 72(3):215–235, 2017.

[23] T. Tang, O. Hededal, and P. Cardiff. On finite volume method implementation of poro-elasto-plasticity soil model. *International Journal for Numerical and Analytical Methods in Geomechanics*, 39(13):1410–1430, 2015.

[24] P. Cardiff, Ž. Tuković, P. D. Jaeger, M. Clancy, and A. Ivanković. A lagrangian cell-centred finite volume method for metal forming simulation. *International Journal for Numerical Methods in Engineering*, 109(13):1777–1803, 2017.

[25] J. Fainberg and H.-J. Leister. Finite volume multigrid solver for thermo-elastic stress analysis in anisotropic materials. *Computer Methods in Applied Mechanics and Engineering*, 137(2):167 – 174, 1996.

[26] I. Demirdžić, I. Horman, and D. Martinović. Finite volume analysis of stress and deformation in hygro-thermo-elastic orthotropic body. *Computer Methods in Applied Mechanics and Engineering*, 190(8):1221 – 1232, 2000.

[27] A. Ivanković, S. Muzaferija, and I. Demirdžić. Finite volume method and multigrid acceleration in modelling of rapid crack propagation in full-scale pipe test. *Computational Mechanics*, 20(1):46 – 52, 1997.

[28] V. Stylianou and A. Ivanković. Finite volume analysis of dynamic fracture phenomena – I. A node release methodology. *International Journal of Fracture*, 113(2):107 – 123, 2002.

[29] A. Karač, B. R. K. Blackman, V. Cooper, A. J. Kinloch, S. R. Sanchez, W. S. Teo, and A. Ivanković. Modelling the fracture behaviour of adhesively-bonded joints as a function of test rate. *Engineering Fracture Mechanics*, 78(6):973 – 989, 2011.

[30] D. Carolan, Ž. Tuković, N. Murphy, and A. Ivanković. Arbitrary crack propagation in multi-phase materials using the finite volume method. *Computational Materials Science*, 69:153–159, 2013.

[31] I. Demirdžić and A. Ivanković. Finite volume approach to modelling of plates. In *2nd Congress of Croatian Society of Mechanics*, Brač, 1997.

[32] M. A. Wheel. A finite volume method for analysing the bending deformation of thick and thin plates. *Computer Methods in Applied Mechanics and Engineering*, 147(1):199 – 208, 1997.

[33] S. Das, S. R. Mathur, and J. Y. Murthy. Finite-volume method for structural analysis of RF MEMS devices using the theory of plates. *Numerical Heat Transfer, Part B: Fundamentals*, 61(1):1 – 21, 2012.

[34] N. Fallah and A. Parayandeh-Shahrestany. A novel finite volume based formulation for the elasto-plastic analysis of plates. *Thin-Walled Structures*, 77:153 – 164, 2014.

[35] H. Bašić, I. Demirdžić, and S. Muzaferija. Finite volume method for simulation of extrusion processes. *International Journal for Numerical Methods in Engineering*, 62(4):475–494, 2005.

[36] S. Das, S. R. Mathur, and J. Y. Murthy. An unstructured finite-volume method for structure–electrostatics interactions in MEMS. *Numerical Heat Transfer, Part B: Fundamentals*, 60(6):425–451, 2011.

[37] P. Cardiff, A. Karač, and A. Ivanković. Development of a finite volume contact solver based on the penalty method. *Computational Materials Science*, 64:283 – 284, 2012.

[38] P. Cardiff, A. Karač, D. FitzPatrick, R. Flavin, and A. Ivanković. Development of mapped stress-field boundary conditions based on a hill-type muscle model. *International Journal for Numerical Methods in Biomedical Engineering*, 30(9):890–908, 2014.

[39] C. H. Lee, A. J. Gil, and J. Bonet. Development of a cell centred upwind finite volume algorithm for a new conservation law formulation in structural dynamics. *Computers & Structures*, 118:13 – 38, 2013.

[40] J. Haider, C. H. Lee, A. J. Gil, and J. Bonet. A first-order hyperbolic framework for large strain computational solid dynamics: An upwind cell centred Total Lagrangian scheme. *International Journal for Numerical Methods in Engineering*, 109(3):407–456, 2016.

[41] I. Demirdžić. A fourth-order finite volume method for structural analysis. *Applied Mathematical Modelling*, 40(4):3104 – 3114, 2016.

[42] I. Demirdžić, S. Muzaferija, and M. Perić. Benchmark solutions of some structural analysis problems using the finite-volume method and multigrid acceleration. *International Journal for Numerical Methods in Engineering*, 40(10):1893–1908, 1997.

[43] P. Cardiff, Ž. Tuković, H. Jasak, and A. Ivanković. A block-coupled finite volume methodology for linear elasticity and unstructured meshes. *Computers & Structures*, 175:100–122, 2016.

[44] P. Cardiff and I. Demirdžić. Thirty years of the finite volume method for solid mechanics. Submitted, 2018.

[45] Termo Fluids S.L. http://www.termofluids.com/.

[46] P. Chandrashekar and A. Garg. Vertex-centroid finite volume scheme on tetrahedral grids for conservation laws. *Computers & Mathematics with Applications*, 65(1):58–74, 2013.

[47] Ž. Tuković, A. Ivanković, and A. Karač. Finite-volume stress analysis in multi-material linear elastic body. *International Journal for Numerical Methods in Engineering*, 93(4):400–419, 2013.

[48] K.-J. Bathe and M. M. I. Baig. On a composite implicit time integration procedure for nonlinear dynamics. *Computers & Structures*, 83(31):2513 – 2524, 2005.

[49] K.-J. Bathe. Conserving energy and momentum in nonlinear dynamics: A simple implicit time integration scheme. *Computers & Structures*, 85(7):437 – 445, 2007.

[50] E. H. Dill. *Continuum Mechanics. Elasticity, Plasticity, Viscoleasticity*. CRC Press, 2006.

[51] A. F. Bower. *Applied Mechanics of Solids*. CRC Press, 2009.

[52] R. B. Hetnarski and M. R. Eslami. *Thermal Stresses - Advanced Theory and Applications*. Springer, 2009.

[53] H. Parkus. *Thermoelasticity (Second revised and enlarged edition)*. Springer-Verlag, 1976.

[54] L. A. Mihai, L. Chin, P. A. Janmey, and A. Goriely. A comparison of hyperelastic constitutive models applicable to brain and fat tissues. *Journal of The Royal Society Interface*, 12(110):20150486, 2015.

[55] A. Ibrahimbegovic. *Nonlinear solid mechanics: theoretical formulations and finite element solution methods*. Springer, 2009.

[56] J. Bonet and R. D. Wood. *Nonlinear Continuum Mechanics for Finite Element Analysis*. Cambridge University Press, 2 edition, 2008.

[57] E. A. de Souza Neto, D. Peric, and D. R. Owen. *Computational methods for plasticity: theory and applications*. John Wiley & Sons, 2011.

[58] C. D. Pérez-Segarra, C. Farré, J. Cadafalch, and A. Oliva. Analysis of different numerical schemes for the resolution of convection-diffusion equations using finite-volume methods on three-dimensional unstructured grids. Part I: Discretization schemes. *Numerical Heat Transfer, Part B: Fundamentals*, 49(4):333–350, 2006.

[59] G. Noh and K.-J. Bathe. An explicit time integration scheme for the analysis of wave propagations. *Computers & Structures*, 129:178 – 193, 2013.

[60] R. D. Cook. *Concepts and applications of finite element analysis*. Wiley, 2001.

[61] N. M. Newmark. A method of computation for structural dynamics. *Journal of the engineering mechanics division*, 85(3):67–94, 1959.

[62] K.-J. Bathe and G. Noh. Insight into an implicit time integration scheme for structural dynamics. *Computers & Structures*, 98-99:1 – 6, 2012.

[63] P. J. Oliveira and C. J. Rente. Development and application of a finite volume method for static and transient stress analysis. *Proc. NAFEMS World Congress on Effective Engineering Analysis*, 1:297–309, 1999.

[64] W. Wen, Y. Tao, S. Duan, J. Yan, K. Wei, and D. Fang. A comparative study of three composite implicit schemes on structural dynamic and wave propagation analysis. *Computers & Structures*, 190:126 – 149, 2017.

[65] R. Costa, S. Clain, and G. J. Machado. New cell–vertex reconstruction for finite volume scheme: Application to the convection–diffusion–reaction equation. *Computers & Mathematics with Applications*, 68(10):1229 – 1249, 2014.

[66] P. Cardiff. *Development of the finite volume method for hip joint stress analysis*. PhD thesis, University College Dublin. School of Mechanical & Materials Engineering, 2012.

[67] Ž. Tuković and H. Jasak. A moving mesh finite volume interface tracking method for surface tension dominated interfacial fluid flow. *Computers & Fluids*, 55:70–84, 2012.

[68] M. Rauter and Ž. Tuković. A finite area scheme for shallow granular flows on three-dimensional surfaces. *Computers & Fluids*, 166:184 – 199, 2018.

[69] H. Jasak. *Error analysis and estimation for the finite volume method with applications to fluid flows*. PhD thesis, Imperial College London (University of London), 1996.

[70] A. J. Macleod. Acceleration of vector sequences by multidimensional Δ^2 methods. *Communications in Applied Numerical Methods*, 2(4):385–392, 1986.

[71] R. W. Clough and J. Penzien. *Dynamics of Structures (Third edition)*. McGraw-Hill, 1995.

[72] R. Borrell Pol. *Parallel algorithms for computational fluid dynamics on unstructured meshes*. PhD thesis, Universitat Politècnica de Catalunya, 2012.

[73] S. Balay, S. Abhyankar, M. F. Adams, J. Brown, P. Brune, K. Buschelman, L. Dalcin, V. Eijkhout, W. D. Gropp, D. Kaushik, M. G. Knepley, L. C. McInnes, K. Rupp, B. F. Smith, S. Zampini, H. Zhang, and H. Zhang. PETSc users manual. Technical Report ANL-95/11 - Revision 3.8, Argonne National Laboratory, 2017.

[74] S. Balay, W. D. Gropp, L. C. McInnes, and B. F. Smith. Efficient management of parallelism in object oriented numerical software libraries. In E. Arge, A. M. Bruaset, and H. P. Langtangen, editors, *Modern Software Tools in Scientific Computing*, pages 163–202. Birkhäuser Press, 1997.

3

Verification and computational performance of the structural method

3.1 Introduction

This chapter is devoted to assessing the accuracy, stability and computational performance of the structural model that was mathematically assembled and numerically discretised in chapter 2. Seven test cases have been selected to examine different aspects of the implemented finite volume method. The results are compared with standard finite element benchmarks, other finite volume formulations and closed form solutions. A comparison among the different converge acceleration techniques is conducted by measuring calculation times both on a workstation and a supercomputer.

First, the linear thermoelasticity model is verified by means of static cases with temperature change (section 3.2.1) and uniform temperature (section 3.2.2). Then, numerical experiments concerning the dynamic response of the same material model are carried out, in section 3.2.3 without structural dissipation and in section 3.2.4 with Rayleigh and mass proportional damping. Sections 3.3.1 and 3.3.2 deal with the nonlinear updated Lagrangian formulation for hyperelastic materials. In the former, the constitutive models of Saint Venant-Kirchhoff and neo-Hookean are used in a static bending scenario. In the latter, the robustness of the nonlinear method to tackle nearly-incompressible materials is tested simulating the vibration of a neo-Hookean body.

Additionally, the reduction of time cost due to accelerating the segregated algorithm and implicitly coupling the displacement components is discussed in sections 3.2.1 and 3.2.2. Section 3.2.4 includes this same comparison and the speed-up achieved by the extrapolation step in transient cases. Finally, the parallel efficiency of the code is investigated in section 3.4 with a problem of complex geometry and infinitesimal deformations.

Despite being a verification exercise, it should be noted that in some cases the study has been extended beyond previous works on cell-centred finite volume structural analysis. Different time schemes are tested and their integration errors numerically quantified, including the Bathe method [1], which has not been used yet within the finite volume framework [2–5]. The performance of the block-coupled method [6] with respect to the classical segregated algorithm is measured for the first time in dynamic problems and in a parallel computing architecture. The comparison between structural damping models is new too since only constant coefficient damping ($c\ddot{\boldsymbol{u}}$) has been found in the literature [3, 7]. Moreover, the finite bending of a beam in section 3.3.1 is studied under more demanding conditions than [7] and is compared in more detail with the analytical solution.

3.2 Linear elastic cases

In this section the accuracy of the linear thermoelastic model is studied for four different cases, in static and dynamic scenarios, both with and without structural damping. Besides, the effectiveness to reduce the computational times of the segregated convergence acceleration and the block-coupled arrangement is analysed.

A conjugate gradient solver (cg) with an incomplete Cholesky factorisation preconditioner (icc) is used within the segregated tests, whereas a biconjugate gradient method (bcgs) preconditioned by incomplete factorisations (ilu) is used within the coupled tests. Problem convergence tolerance is defined to be 10^{-7}.

3.2.1 Case A: Thermal loading

The static test coded as LE11 from the National Agency for Finite Element Methods and Standards (NAFEMS) [8] is frequently used to verify three-dimensional linear thermoelastic models (see for instance [9–11]). A body of revolution composed of a tapered cylinder and a sphere is subjected to a linear temperature gradient in radial and axial direction. The vertical thermal expansion of the structure is constrained by

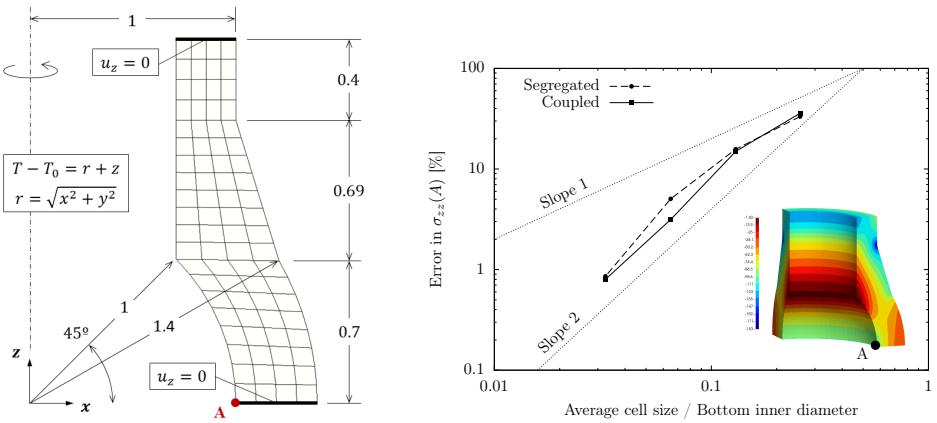

Figure 3.1: Case A: Problem description with mesh 2 (left) and variation of relative error in σ_{zz} at point $\boldsymbol{A}$ (right). All boundary conditions not specified are traction free. Units in m, ºC.

supports on the bottom and top faces. Details on the geometry and boundary conditions can be found in figure 3.1 (left). The mechanical properties of the elastic material are Young's modulus $E = 210$ GPa, Poisson's ratio $\nu = 0.3$ and thermal expansion coefficient $\alpha = 2.3 \cdot 10^{-4}$ K^{-1}.

Since axial thermal expansion is limited, compressive axial stresses will develop. As can be observed in figure 3.1 (right), the body experiences a local increase of stress in one of the outer edges, as a result of the geometric discontinuity. The reference solution refers to this axial thermal stress σ_{zz} at point $\boldsymbol{A} = (1,0,0)$ m, and its value should be -105 MPa.

Due to the axisymmetric nature of geometry and loads, only a quarter of the cylindrical solid is modelled. Four different grid refinements have been tested, each one doubling the number of divisions in all directions of the previous. The coarsest mesh (mesh 1) has $2 \times 3 \times 10$ hexahedral volumes in (r, θ, z) coordinates. Thus, the resulting number of cells of the other meshes are: $4 \times 6 \times 20$ (mesh 2 in figure 3.1), $8 \times 12 \times 40$ (mesh 3) and $16 \times 24 \times 80$ (mesh 4). It has been confirmed that two integration volumes through the thickness are enough to capture properly the elastic bending, instead of the typical three, thanks to the face-centred calculation of the stresses.

The relative error in axial stress at the specified point is plotted as a function of grid size in figure 3.1 (right). The stress at this corner point has been linearly interpolated from the values at neighbouring face-centres. As can be seen, the solution converges at

a second-order rate to the reference value. This order of accuracy in space is not the expected in stress since the displacement-based formulation leads to second order in the displacement (the primary variable), but first order in its spatial derivatives, and hence in strain and stress. The obtained accuracy should be therefore resulting from the particular distribution of stresses and grid points of this case.

Apart from this, the spatial discretisation shows good performance taking into account that it is a point which is located in the domain corner. The vertex interpolation technique and the gradient tangential discretisation provides the same accuracy both on inner and boundary faces. Although segregated and block-coupled methodologies share the same numerical schemes, a minor discrepancy in the stress error appears with mesh 3, probably due to convergence criteria or linear solvers operation.

The execution times consumed to run this case are presented in table 3.1. In general, the computing demand of this case is very low for all meshes, although noticeable differences appear depending on the kind of linear system arrangement and resolution. The convergence acceleration introduced in the classical segregated approach can decrease the computing time with all mesh refinements (between 9 % and 47 %). However, the major savings in this sense are produced by the block-coupled method, which solves the problem up to 2.4 times faster than the proposed segregated method.

Table 3.1: Case A-B: Execution time with each numerical approach: segregated (S), segregated with convergence acceleration (SA) and block-coupled (C). Simulations have been carried out using 1 CPU core (3.4 GHz Intel Haswell processors).

	Case A				Case B			
Mesh	1	2	3	4	1	2	3	4
S [s]	0.10	0.60	4.8	38	0.27	2.0	18	168
SA [s]	0.09	0.31	2.5	25	0.17	1.0	4.9	39
C [s]	0.07	0.15	1.0	10	0.06	0.17	1.1	11
S / SA	1.1	1.9	1.9	1.5	1.6	2.1	3.8	4.3
SA / C	1.4	2.0	2.4	2.4	2.6	5.7	4.3	3.4

3.2.2 Case B: Bending of a thick plate

This test evaluates the static out-of-plane bending of a thick elliptic plate with an elliptic hole. The body is completely clamped at the outer edge and loaded by a normal uniform pressure of 1 MPa at the upper surface. Figure 3.2 (left) presents the exact definition

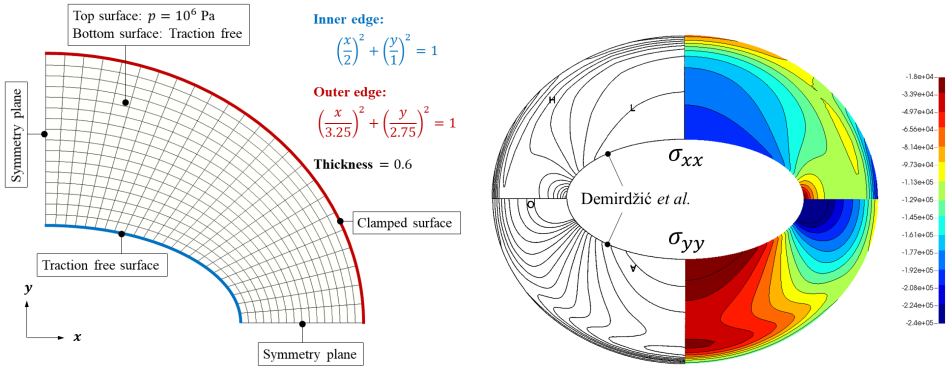

Figure 3.2: Case B: Problem description with mesh 3 (left) and distribution of stress components on the plate mid-section obtained with mesh 4 compared with results from [12] (right). Units in m.

of the geometry. Material properties are $E = 210$ GPa and $\nu = 0.3$. The problem was initially proposed as a three-dimensional benchmark by NAFEMS [8], and it was later studied extensively within the finite volume framework by [12], who defined the slightly different boundary conditions which are here mimicked.

A quarter of the domain is again sufficient for the simulation due to the double symmetry of the problem. As in the previous case, four systematically refined hexahedral meshes have been tested, each of them with the following number of control volumes in (r,θ,z) directions: $4\times6\times3$ (mesh 1), $8\times12\times6$ (mesh 2), $16\times24\times12$ (mesh 3) and $32\times48\times24$ (mesh 4).

The distribution of σ_{xx} and σ_{yy} obtained with mesh 4 on the plate mid-section is compared with the benchmark solution by [12] in figure 3.2 (right). Like in the original solution, the symmetry between both stresses which would be expected with circumferential edges is disrupted by the elliptic shapes. The obtained solution agrees well with the benchmark, although there are visible differences close to the symmetry boundaries, probably as a result of a still coarse grid. In spite of this, convergence to the reference solution is distinctly proved by observing figure 3.3, where x displacement and von Mises equivalent stress along line $x = y$ on the plate mid-section are depicted and compared with tabulated results from [12].

The acceleration achieved with the implemented techniques describes the same tendency as in case A. Even so, both methods reduce the required computational time in greater magnitude than before. This is because bending problems introduce a strong

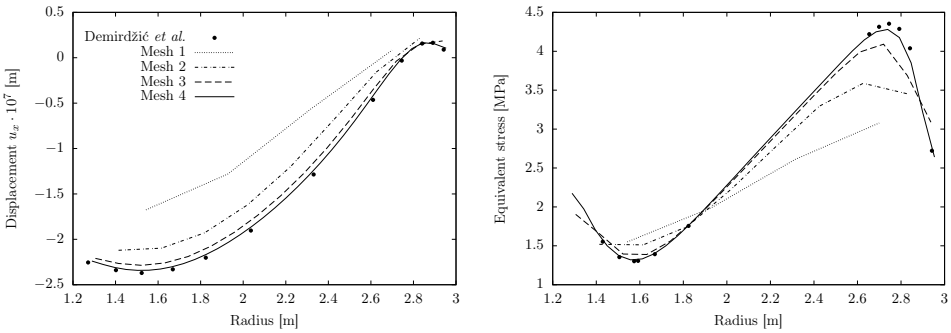

Figure 3.3: Case B: Distribution of u_x (left) and equivalent stress (right) on the plate mid-section along $x = y$ compared with results from [12].

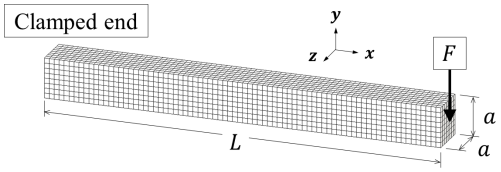

Figure 3.4: Case C: Problem description with spatial discretisation. $a = 2$ m and $L = 10a$.

coupling among displacement components and therefore suppose an unfavourable configuration for the segregated method, where this coupling should be updated through fixed-point iterations. A similar analysis of this case was conducted by [6], showing similar levels of speed-up between block-coupled and segregated methods. In that case, a finite element software was tested too, and the block-coupled approach demonstrated fewer requirements in time (less than one third) and memory (less than half) for all meshes.

3.2.3 Case C: Vibration of a cantilever beam

The aim of this case is to examine the accuracy and stability of the implemented time integration schemes as well as to highlight the differences in computing efficiency among the segregated and block-coupled methods when dealing with a dynamic scenario. To accomplish this goal, the simulation of the linear vibration of a three-dimensional beam is conducted. The structure is fixed at one end, and supports a uniform transverse load at the opposite free end.

Table 3.2: Case C: Average of time integration errors for different time increments and time integration schemes (in order: Euler, three-point backward, trapezoidal and Bathe).

	Period elongation [%]				Amplitude decay [%]			
Δt [s]	Eul.	Three	Trap.	Bat.	Eul.	Three	Trap.	Bat.
0.01	0.018	-0.10	-	-0.044	1.3	0.074	-	0.082
0.1	-0.13	-0.070	0.056	0.14	9.5	0.30	0.032	0.045
1	3.0	3.0	0.90	0.18	62	3.9	-0.77	0.21
2	12	10	3.0	1.9	85	20	0.019	0.18

The case follows an example analysed by [3], and is outlined in figure 3.4. The prismatic beam measures $L = 10a$ long, where a is the side of the square cross-section and is 2 m. Regarding the material, density is 2600 kg/m^3, Young's modulus 10 MPa and Poisson's ratio 0.3. The force in y direction is increased linearly from zero to $F = -500$ N during the first 7 seconds, and then it is released. This ramping helps to avoid a percussive type shock reaction which may develop with a suddenly applied load.

Unlike in the previous cases, here a unique mesh of $80 \times 8 \times 8$ in (x, y, z) (see figure 3.4) has been tested. The variations within the case are centred around different time step sizes: 2 s, 1 s, 0.1 s and 0.01 s; and all implemented time integration schemes: Euler, three-point backward, trapezoidal and Bathe methods. The time step division needed in the Bathe method is carried out so that first sub-step is $\left(2-\sqrt{2}\right)\Delta t^{n+1}$.

Figure 3.5 gathers the transient deflection at the beam tip captured with all time increments and schemes. Since the force is removed and there is no structural damping, a steady vibration around the unstrained configuration, which maintains the energy introduced by the external force, is developed. Considering the converged solution, the motion describes an oscillation with time period $T = 19.96$ s. This figure agrees with the first mode of vibration derived from the Euler-Bernoulli beam theory. According to this theory [13], the natural frequency of vibration of mode n is:

$$f_n = \frac{\beta_n^2}{2\pi}\sqrt{\frac{EI}{\rho a^2}}, \tag{3.1}$$

where $\beta_n L$ equals 1.8751041 m for the first mode. Thus, the load mainly excites the first mode of vibration, and there is no interaction between different modes, as might happen in nonlinear elastodynamics.

Regarding the accuracy of time integration schemes. A very good agreement can be

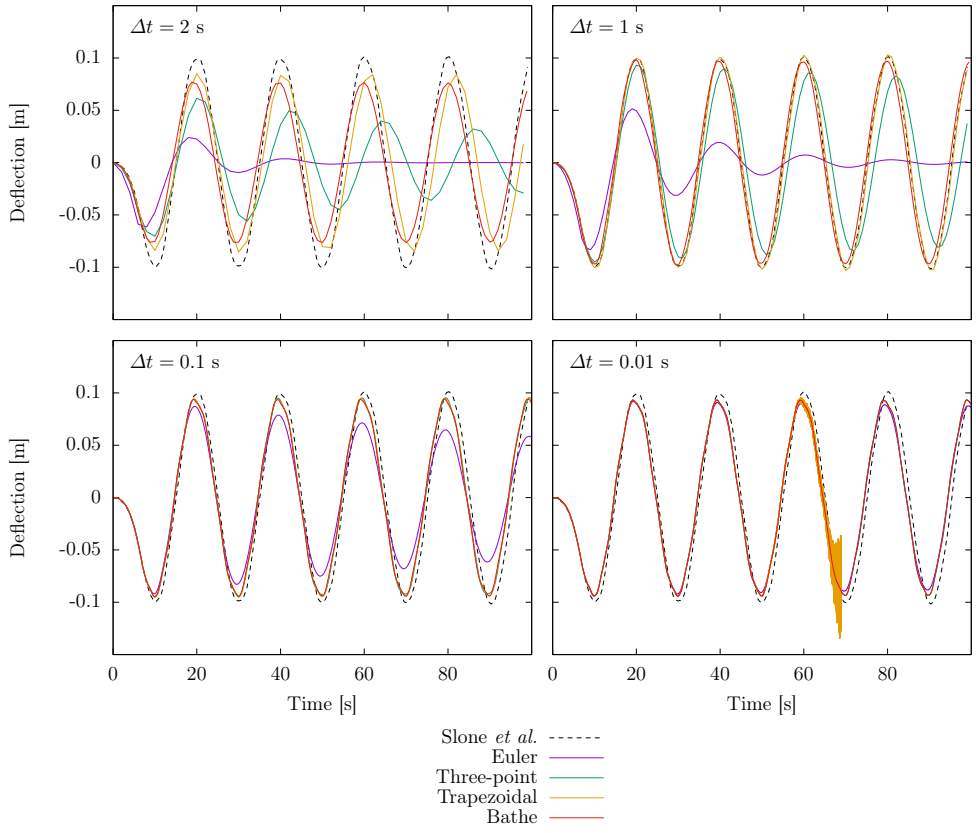

Figure 3.5: Case C: Transient deflection at the centre of the tip for different time integration schemes and time step sizes. Reference results from [3].

distinguished in figure 3.5 in the signal obtained with the trapezoidal rule and $\Delta t = 1$ s when compared with data from [3], where same grid refinement and time parameters were employed. However, numerical results show how all methods converge to a slightly different bending reaction when further decreasing the time increment. Both the trapezoidal rule and the Bathe method are practically reaching the converged response with $\Delta t = 1$ s ($T/\Delta t \approx 20$), whereas three-point backward and Euler schemes require much smaller time steps, about 10 and 100 times smaller, respectively. Post-processing has been performed to calculate the errors in the temporal integration, i.e. period elongation and amplitude decay, in accordance with [14] formulation. Averaged errors are summarised in table 3.2. None of the implicit schemes is showing an important period elongation when $\Delta t \leqslant 1s$. In terms of amplitude decay, it is only different from zero for Euler and three-point backward schemes. The former results in a 85 % decay with $\Delta t = 2$ s and 1.3 % with $\Delta t = 0.01$ s. Meanwhile, the three-point method reduces it from 20 to 0.074 %.

Despite the minor integration errors of the trapezoidal rule, it is suffering from numerical stability issues with the smallest time increment, as shown in figure 3.5. Similar instability has been produced both with segregated and coupled methods. Paying attention to the dynamic response, one can discern high non-physical vibrating modes which emerge and gain amplitude as time progresses. Eventually, displacements and its time derivatives become unrealistically large, and no conservation of momentum is achieved. By reducing the time step, the method can capture these high-frequency modes derived artificially from numerical discretisation, and calculation tolerances progressively intensify them. The other schemes for the inertial term can avoid this error accumulation over time because they are adding some numerical dissipation, which discards these spurious modes.

Other authors have previously described this kind of numerical error. Works by [4,15] highlighted the dispersion provoked by second-order Newmark-type methods and their "tendency to introduce high-frequency noise, especially in the vicinity of sharp spatial gradients". As a matter of fact, the Bathe method has been employed to avoid this problem with elastic materials with moderate displacements [1, 16] and with linear cases where flexible and almost rigid parts coexist [17]. Similarly, in [18] a two-step method including the trapezoidal rule and a dissipative scheme was presented to filter the spurious high modes within wave propagation in elastic materials.

Finally, the computational effort of the code to face dynamic cases will be discussed. Table 3.3 summarises the time dedicated to conducting the entire transient simulations (from 0 to 100 physical seconds) with the block-coupled method. The cost increases as

Table 3.3: Case C: Execution time (in seconds) with the block-coupled method for different time integration schemes and time increments. Simulations have been carried out using 1 CPU core (3.4 GHz Intel Haswell processors).

Δt [s]	Euler	Three-point	Trapezoidal	Bathe
0.01	765	665	-	902
0.1	580	404	313	363
1	266	251	233	324
2	145	140	137	234

Table 3.4: Case C: Execution time with three-point backward time scheme and all different segregated transient approaches: segregated (S), S with convergence acceleration (SA), SA with Euler predictor (SA-E) and SA with Adams predictor (SA-A). Time has been expressed relative to the time spent by using the block-coupled method and the same time scheme. Simulations have been carried out using 1 CPU core (3.4 GHz Intel Haswell processors).

Δt [s]	S	SA	SA-E	SA-A
0.01	10	7.9	2.7	2.6
0.1	12	5.9	3.7	3.9
1	20	5.9	4.9	6.4
2	32	7.5	6.8	6.0

the number of required time iterations does, although it is not directly proportional since the solutions of two consecutive instants become more and more similar and hence cost per time step falls. When comparing how the different schemes affect the execution time only the greater effort needed for the Bathe method, which splits a time step resolution in two, can be emphasised.

Table 3.4 shows the time cost of the segregated method relative to that of the block-coupled method. As in case B, being a bending case defines a strong dependency among displacement components, complicating convergence of fixed-point iterations. The use of the Aitken acceleration technique, though, manages to shrink notably the execution time, especially for larger time steps. On the other hand, the addition of a predictor step, to extrapolate the value at the start of an instant resolution, provides important savings in the transient simulations. Despite the higher order of Adams' predictor compared with Euler's, no significant improvement is achieved. Thanks to both Aitken and prediction techniques, it is possible to solve the entire case with the segregated method and $T/\Delta t \approx 100$ s consuming only 2.6 times more time than the

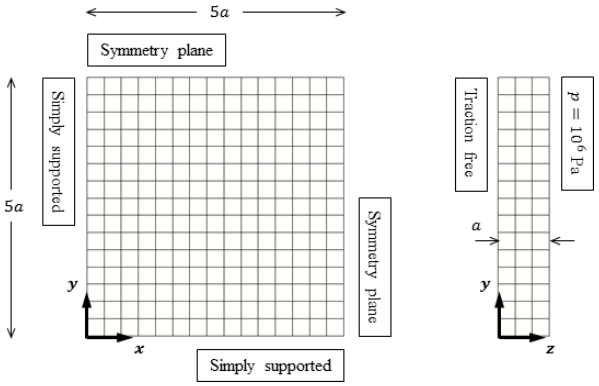

Figure 3.6: Case D: Problem description with coarsest mesh. $a = 1$ m.

block-coupled method. In summary, the fact that this gap can continue narrowing when further reducing the Δt, plus the considerable memory savings and system robustness offered by the segregated approach, makes this method still competitive and useful for numerical analysis of solid mechanics.

3.2.4 Case D: Damped vibration of a plate

The damped vibration of a simply supported thick plate under a uniform pressure is studied in order to verify the implementation of structural damping within the method for solid dynamics. The case is described in NAFEMS benchmarks [8] as a verification exercise of new finite element procedures. The side length of the square plate is 10 m, and its thickness is 1 m. Figure 3.6 contains the boundary conditions of a single quarter of the plate, which is sufficient for the modelling due to the symmetries in the problem configuration. Material Young's modulus is 200 GPa, Poisson's ratio is 0.3 and density is 8000 kg/m^3. Damping is defined as $\zeta_1 = 0.02$, i.e. as 2 % of critical damping in the first natural vibration mode.

Two kinds of structural damping formulations will be used: Rayleigh and mass-only proportional. Rayleigh parameters will be determined by assuming a balanced contribution of mass and stiffness terms as:

$$\zeta_1 = \frac{\alpha_R}{2\omega_1} + \frac{\beta_R \omega_1}{2} = 0.01 + 0.01 = 0.02\,. \tag{3.2}$$

Taking into account the analytical first natural frequency of such a thick plate (288.4

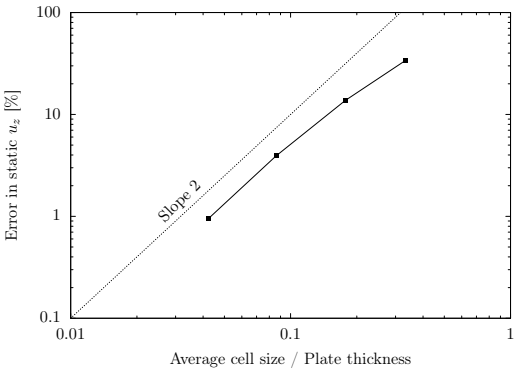

Figure 3.7: Case D: Relative error in static displacement at the plate centre as a function of mesh size.

Table 3.5: Case D: Richardson extrapolation solution obtained by both damping methods.

	Peak displacement		Peak stress	Static case
	u_z [mm]	t [s]	σ_{xx} [MPa]	u_z [mm]
NAFEMS	4.524	0.0108	62.11	2.333
Rayleigh damping	4.605	0.0107	61.20	2.329
Mass proportional damping	4.635	0.0104	65.67	2.329

rad/s [19]) the resulting parameters are: $\alpha_R = 5.772\ \mathrm{s}^{-1}$ and $\beta_R = 6.929 \cdot 10^{-5}$ s. When considering a mass proportional damping only, β_R is zero, and thus $\alpha_R = 11.54\ \mathrm{s}^{-1}$.

Looking for a grid independent solution, four hexahedral meshes with different level of refinement will be tested. They can be defined by the next number of control volumes in (x, y, z) directions: $15 \times 15 \times 3$, $30 \times 30 \times 5$, $60 \times 60 \times 11$ and $120 \times 120 \times 23$. A central line of face nodes is needed at the edge of the plate in order to set the simply supported boundary condition as a displacement constraint only along that line. Time discretisation is established to prevent any numerical dissipation from influencing in the solution. In this sense, the trapezoidal rule and a sufficiently small time step of 10^{-5} s has been chosen. This Δt is equivalent to a Courant number of 2.4 in the finest mesh and can be translated as more than 2000 time iterations per oscillation period.

Solution accuracy as a function of grid size is outlined in figure 3.7, where the relative error on the static deflection at the centre of the plate for all four meshes is plotted. The reference solution is obtained from [8] and is shown in table 3.5. As can

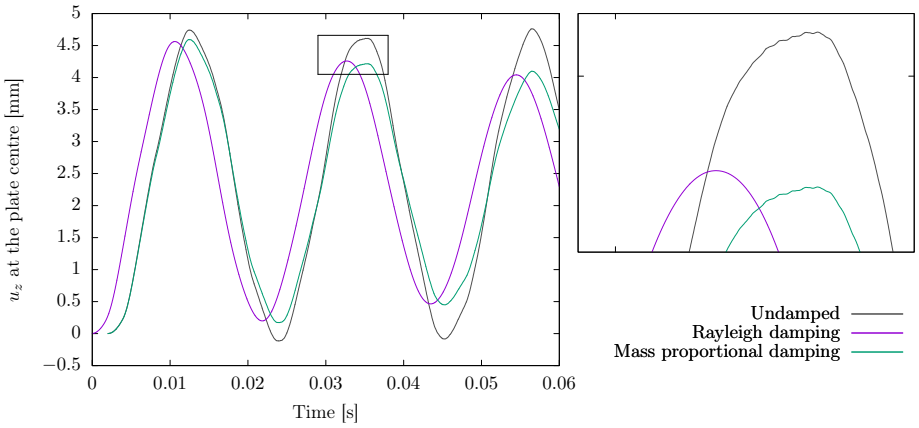

Figure 3.8: Case D: Time history of normal displacement at the centre of the plate. Mass proportional damping and undamped responses have been shifted +0.002 s for visualization purposes.

be seen, the numerical result tends monotonically to the benchmark, and relatively small error can be achieved with the finest mesh. Therefore, this refinement will be used to predict the dynamic response of the structure after the sudden application of the perpendicular load.

Figure 3.8 compares the transient evolution of normal displacement at the plate centre obtained with both structural damping models. Damping causes the oscillations around the static equilibrium to gradually decay in amplitude because damping force is acting against the velocity of the body. Although the responses are overall alike, regarding amplitude decrease and frequency, small differences can be appreciated when observing closely. The graph demonstrates the presence of high vibration modes when no damping is imposed, as a result of the abrupt application of the external force. It is very perceptible in the profile of the bending stress depicted in figure 3.9. Rayleigh dissipation suppresses those modes and in the end, leads to a practically smooth sinusoidal oscillation in displacement and stress governed by the first mode only. On the other hand, the mass proportional damping is imposing small damping ratios at the higher modes, and hence the solution exhibits higher-frequency contributions. This difference between both models is well known and produced too in the finite element community [20–22].

Table 3.5 presents the peak displacement and maximum bending stress at the centre

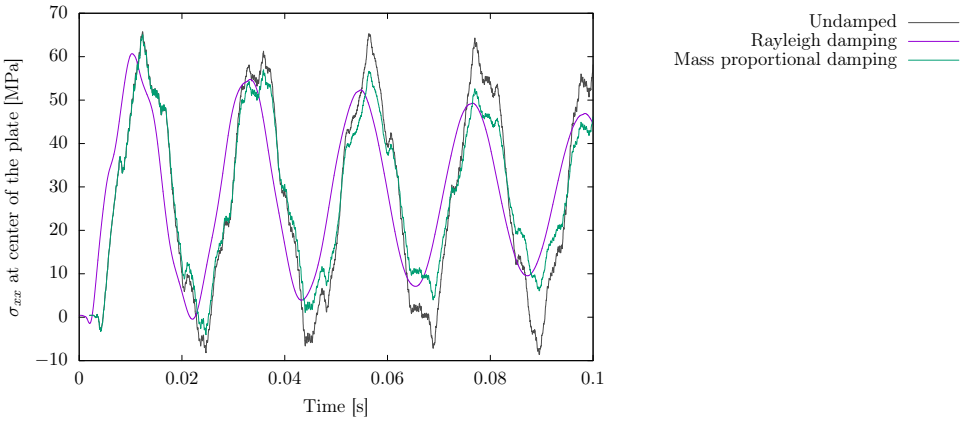

Figure 3.9: Case D: Time history of bending stress at the centre of the plate. Mass proportional damping and undamped responses have been shifted +0.002 s for visualization purposes.

of the plate. The converged numerical solution has been approximated by following the Richardson extrapolation [23] and the results from the two finest meshes:

$$\phi_{exact} \approx \phi_1 + \frac{\phi_1 - \phi_2}{(h_2/h_1)^2 - 1}, \tag{3.3}$$

where h_1 and h_2 are the discrete spacings of the finest and second finest grid, and ϕ_1 and ϕ_2 the result from the same meshes. The figures indicate that a better agreement with the benchmark is achieved by means of the proposed finite-volume Rayleigh damping.

3.3 Hyperelastic cases

The content of this section is focused on verifying the extension of the segregated elastic model to solve hyperelastic materials subjected to large deformations. Hyperelasticity adds geometrical nonlinearity to the governing equation as a result of the unknown integration domain, but can also add material nonlinearities provided that the constitutive model specifies a nonlinear relation between strain and stress. This verification is carried out analysing both a static and a dynamic benchmark problem.

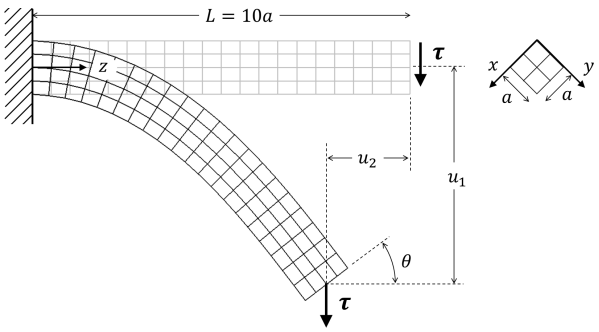

Figure 3.10: Case E: Problem description with mesh 1. $a = 0.2$ m.

3.3.1 Case E: Large deformation of a beam

The large deflection and moderate rotation of a three-dimensional cantilever beam under a terminal shear force is here evaluated. The objective is to demonstrate the second and first order of accuracy in displacement and stresses, respectively, for the proposed discretisation. Since there is no closed form solution for this problem, the solution generated with the finest mesh will be used as a reference to check the error convergence rate. Furthermore, the computed solution will be compared with numerical results from [7] and with a closed form obtained with certain simplifications [24].

The structure is a prismatic body with square diamond cross section with side $a = 0.2$ m, as shown in figure 3.10. The length of the beam is $L = 10a$ and the mechanical properties are $E = 15.293$ MPa and $\nu = 0.3$. It is fully clamped at one end and subjected to a uniform shear traction $\boldsymbol{\tau}$ at the other end. The magnitude of this external load is characterised by the dimensionless parameter $\mathscr{K}$, which is expressed as:

$$\mathscr{K} = \frac{|\boldsymbol{\tau}| a^2 L^2}{EI}, \tag{3.4}$$

where I is the moment of inertia, which is equivalent to $a^4/12$ for this geometry. Thus, the shear traction $\boldsymbol{\tau}$ applied on the free end can be defined as:

$$\boldsymbol{\tau} = \frac{\mathscr{K} EI}{a^2 L^2} \left(\frac{1}{\sqrt{2}}, \frac{1}{\sqrt{2}}, 0 \right). \tag{3.5}$$

In the present study the loading parameter $\mathscr{K}$ will take values ranging from 0.2 to 10.

This particular configuration of the problem corresponds to the work previously de-

Table 3.6: Case E: Deflection u_1/L for different levels of external load and grid refinements with the Saint Venant-Kirchhoff constitutive model. Reference results from [7].

	Tuković & Jasak	Mesh 1	Mesh 2	Mesh 3	Mesh 4
$\mathscr{K}$	$10 \times 10 \times 100$	$2 \times 2 \times 20$	$4 \times 4 \times 40$	$8 \times 8 \times 80$	$16 \times 16 \times 160$
0.2	0.06545	0.05809	0.06407	0.06578	0.06625
0.4	0.1291	0.1150	0.1266	0.1299	0.1308
0.8	0.2455	0.2214	0.2420	0.2478	0.2494
1.6	0.4254	0.3922	0.4206	0.4284	0.4305

veloped by [7]. They also used a cell-centred finite volume formulation with an updated lagrangian approach, but employed different methods for instance for the gradient calculation or mesh update. Their analysis was limited to a Saint Venant-Kirchhoff material and a maximum shear load of $\mathscr{K} = 1.6$. A similar numerical experiment was conducted by [25], who solved the static deflection of a thick Mooney-Rivlin beam under shear loads up to $\mathscr{K} \approx 15.5$. The authors did not present quantitative results on beam deflections but just highlighted the order of convergence of their mixed finite element formulation. Apart from these three-dimensional numerical solutions, which do not make any assumption in the final strain-stress state, several authors have made an effort during the last century to find closed form solutions for large deformation on beams. A review of the topic can be found in [26].

The first experiment will consist on reproducing the case from [7] (material model and external loads) in order to verify the nonlinear solution. To do so, four increasingly refined hexahedral meshes have been used. The number of control volumes in (x, y, z) of each mesh is: $2 \times 2 \times 20$ (mesh 1), $4 \times 4 \times 40$ (mesh 2), $8 \times 8 \times 80$ (mesh 3) and $16 \times 16 \times 160$ (mesh 4). It has been found that long aspect ratio cells produce stiffer bending response, as happens in displacement-based finite element formulations. In table 3.6 the dimensionless deflection predicted with the Saint Venant Kirchhoff constitutive model and all four meshes is compared with the reference solution. Figure 3.10 shows how this deflection is measured as $u_1 = (u_x^2 + u_y^2)^{1/2}$. As can be seen in the table, the numerical results converge to a slightly greater value than the reference for all levels of shear force. This can be caused by the mesh density. The original authors observed an increase in the resulting deflection as the mesh was refined but they stopped at a mesh resolution of $10 \times 10 \times 100$. However, in the present study a smaller grid size has been tested and consequently a more precise solution would have been obtained. Moreover, better accuracy would have been achieved with a coarser mesh of $8 \times 8 \times 80$ owing to the

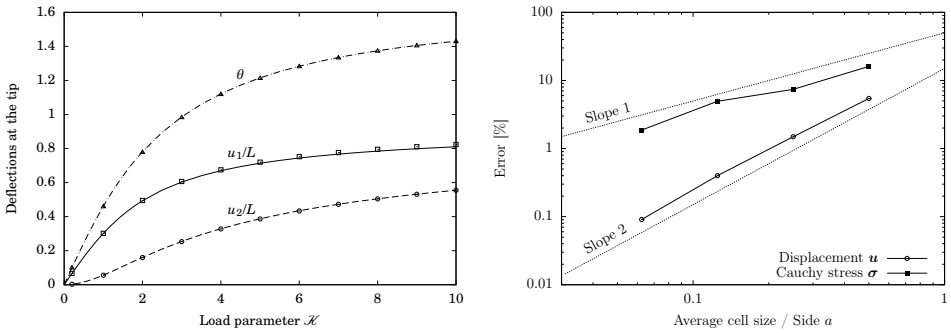

Figure 3.11: Case E: On the left the deflections at the beam tip for increasing magnitude of the external load. Closed form solution from [24] (lines) and numerical results with the compressible neo-Hookean constitutive model and mesh 4 (points). On the right the relative error in displacement and stress as a function of grid size with the neo-Hookean model and a load $\mathscr{K} = 5$.

implemented enhanced numerical method.

In the second test the terminal traction will be risen up to $\mathscr{K} = 10$. To avoid a wrong prediction from the Saint Venant-Kirchhoff material model when large strains arise, the compressible neo-Hookean model of equation 2.31 will be employed to describe the elastic response of the body. Simulations with mesh 4 and different load levels predict the deflections plotted in figure 3.11 (left). Non-linear response in the deformation is clearly visible, since the structure tends to stiffen when the force grows. As the bending increases, beam axis rotates and becomes more aligned with the conservative force, which maintains its original orientation. Thus, the force changes from a bending load to a tensile load, and the beam is able to show greater resistance against the latter.

The rate of convergence of the solution was examined for $\mathscr{K} = 5$ by comparing the results from all four meshes with the solution generated with a finer mesh of $32 \times 32 \times 320$ cubic control volumes. The global difference on displacement vector all over the domain is evaluated as:

$$err_{\boldsymbol{u}} = 100 \sqrt{\frac{\sum_i |\boldsymbol{\epsilon}_i|^2}{\sum_i |\boldsymbol{u}_{i,ref}|^2}}, \tag{3.6}$$

where i is every computational node of the mesh, $\boldsymbol{u}_{i,ref}$ is its corresponding benchmark displacement and $\boldsymbol{\epsilon}_i = \boldsymbol{u}_i - \boldsymbol{u}_{i,ref}$. The error in the stress tensor is similarly calculated, but with i referring to the face centres and using the matrix Frobenius norm for the tensor norm, i.e. the square root of the sum of the squares of its elements. These

Table 3.7: Case E: Deflection u_1/L of compressible neo-Hookean beams with different aspect ratio subjected to a load of $\mathscr{K} = 10$. Reference result from [24] and numerical results obtained with a mesh size equivalent to mesh 4, i.e. $a/16$.

L	u_1/L	Relative difference [%]
$10a$	0.82253	1.47
$20a$	0.81280	0.27
$40a$	0.81050	0.01
Mattiasson	0.81061	

two errors are displayed as a function of grid size in figure 3.11 (right). As expected, displacement converges to a second-order rate whereas the stress does to a first-order rate.

Finally, the neo-Hookean three-dimensional output will be compared with a closed form solution from [24], which was numerically evaluated by means of elliptic integrals within the same range of transversally acting loads. The author solved the large deflection of the cantilever beam considering both axial and shear deformations negligible. The purpose of this comparison is to assess the significance of such assumptions in the final deformation of thick beams like the one here considered. The original tabulated deflections are depicted along with the current results in figure 3.11 (left). In general, the simplified analytical solution yields a very good approximation of the body global deformation. However, a slight deviation in u_1 arises with the greater loads.

It is known that shear deformation becomes more relevant with large bending and thick beams, and that not considering it leads to underestimate deflections [27], as it is happening with the closed form solution in this case. To confirm this idea, slenderer structures with two and four times the length of the first geometry will be numerically solved under the maximum force of $\mathscr{K} = 10$, and attention will be paid to axial and shear deformations.

Table 3.7 shows how the bending measure approaches the analytical figure as the beam narrows. From 1.59 % difference with an aspect ratio $L/a = 10$ to 0.01 % with $L/a = 40$.

To further emphasize the contrast between the analytical and numerical studies, those ignored deformations in the former will be displayed. The axial deformation is evaluated as the stretch ratio in the axial direction:

$$\lambda_z = \frac{dz}{dz_0} = \frac{1}{\sqrt{1-2e_{zz}}}, \tag{3.7}$$

where dz_0 is the length of an infinitesimal fibre aligned with the undeformed body axis and dz is the length of the same fibre after the deformation. The term e_{zz} corresponds to the axial strain component of the Eulerian-Almansi finite strain tensor, which is referenced to the deformed configuration according to equation 2.11.

The distribution of the axial stretch ratio on the beam longitudinal sections is provided in figure 3.12. Despite the natural stretching and compression in the outer portions of the beam near the bending, it can be seen that there is almost no stretch along the central axis, even with the greatest thickness. In fact, in this case the final length of the beam, measured in the body centreline, has barely augmented by 0.44 %.

Consequently, as expected, it should be the shear deformation the responsible of the discrepancies captured with the thickest structure. The shear evaluation is computed as the change in angle between material vectors $\boldsymbol{z}_0 = (0,0,1)$ (representing the beam axis) and $\boldsymbol{s}_0 = (1,1,0)$ (representing the beam cross-section) once the static equilibrium is achieved. This angle can be extracted from the dot product of their spatial counterparts:

$$\boldsymbol{z} \cdot \boldsymbol{s} = |\boldsymbol{z}||\boldsymbol{s}| \cos\theta_{zs}\,, \tag{3.8}$$

where $\boldsymbol{z} = \boldsymbol{F} \cdot \boldsymbol{z}_0$ and $\boldsymbol{s} = \boldsymbol{F} \cdot \boldsymbol{s}_0$. The angle reduction is noted as ϕ_{zs} and calculated as $\pi/2 - \theta_{zs}$, since both vectors are initially perpendicular.

Again this shear distortion is presented in figure 3.13. It is demonstrated that notable shearing may appear with the aspect ratio of 10. Cross-sections do not remain totally perpendicular all along the axis, mainly near the clamped end, where the angle can change almost 9 º, as highlighted too by [28]. With the longest beam the perpendicularity between axis and sections is well maintained, and hence the similarity between detailed and simplified analysis.

3.3.2 Case F: Vibration of a nearly incompressible column

The transient oscillation of a three-dimensional nearly incompressible column is simulated to assess the robustness of the proposed methodology in highly nonlinear scenarios. Classical displacement-based formulations suffer from volume locking and non-physical pressure oscillations when dealing with nearly incompressible materials ($0.45 < \nu < 0.5$) [14, 29]. Such media, which can be elastomers, rubbers and materials in inelastic conditions, exhibit a vast difference between bulk modulus K and shear modulus μ, which multiplies the error in the evaluation of pressure from the volumetric strain. Consequently, different methods have been developed to solve these cases and

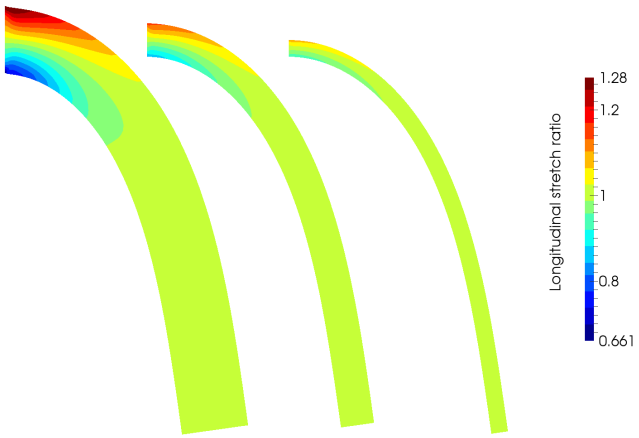

Figure 3.12: Case E: Stretch ratio λ_z in the axial direction under a load of $\mathscr{K} = 10$. From left to right longitudinal section of beams with length $10a$, $20a$ and $40a$, respectively. Numerical results obtained with a mesh size of $a/16$.

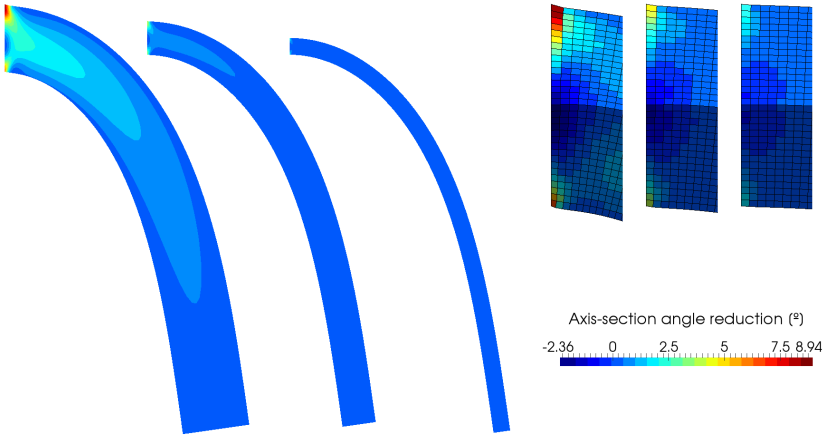

Figure 3.13: Case E: Angle reduction ϕ_{zs} between material vectors $\boldsymbol{z}_0 = (0,0,1)$ and $\boldsymbol{s}_0 = (1,1,0)$ after the deformation resulting from load $\mathscr{K} = 10$. Longitudinal sections (left) and deformed meshes near the clamped end (right) for beams with length $10a$, $20a$ and $40a$. Numerical results obtained with a mesh size of $a/16$.

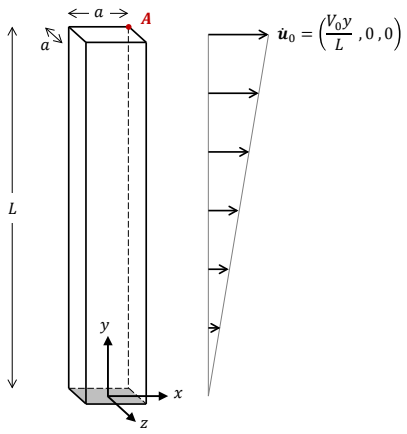

Figure 3.14: Case F: Problem description. $a = 1$ m, $L = 6a$, $V_0 = 10$ m/s and the coordinates of monitored point $\boldsymbol{A}$ are $(0.5, 6, 0.5)$ m. The bottom shaded face is fully clamped.

those which comprise a truly incompressible material ($\nu = 0.5$, $K = \infty$). Some examples within the finite volume framework can be found in [4, 30, 31].

The implemented modelling will be benchmarked against the upwind finite volume mixed formulation used in [31]. Their reference case consists on a squared cross section column with side $a = 1$ m and length $L = 6$ m, as outlined in figure 3.14. The structure is clamped on its bottom face and initialised with a linear velocity field given by $\dot{\boldsymbol{u}}_0 = (V_0 y/L, 0, 0)$, where $V_0 = 10$ m/s. A neo-Hookean model with the incompressibility enforcement of equation 2.32 is used such that density is 1100 kg/m^3, Young's modulus is 17 MPa and Poisson's ratio is 0.45.

Four different meshes are tested. There are three systematically refined hexahedral meshes: $4 \times 16 \times 4$ (mesh 1), $8 \times 32 \times 8$ (mesh 2) and $16 \times 64 \times 16$ (mesh 3); and an unstructured tetrahedral mesh with a uniform grid spacing of $h = 1/16$ m (mesh 4), which results in 158,056 cells. Time discretisation is performed by means of the Euler first-order scheme and a time step of $\Delta t = 10^{-4}$ s, i.e. a Courant number of 0.398 for mesh 3 and 1.96 for mesh 4. Such time parameters were chosen to avoid the numerical instabilities which were encountered with the other discretisation schemes and larger time steps. The reason for the solution divergence was probably related to ill-conditioning problems in the linear system solver, resulting from the almost incompressibility constraint.

Figure 3.15 monitors the evolution of displacement u_X at the column vertex $\boldsymbol{A}$ =

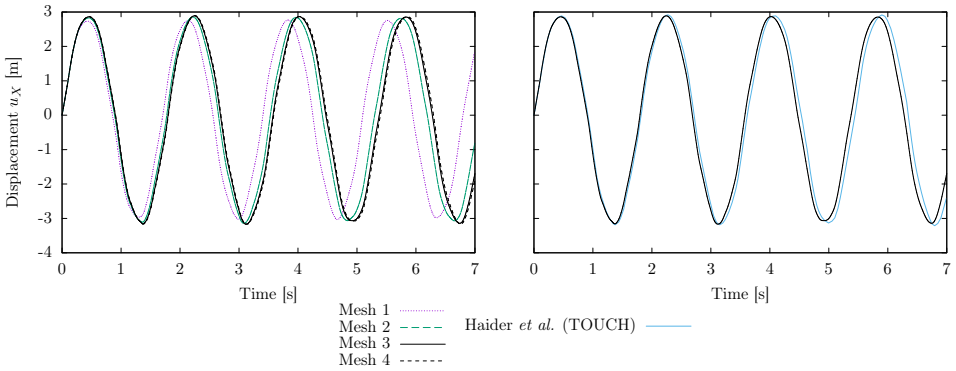

Figure 3.15: Case F: Deflection at material point $\boldsymbol{A} = (0.5, 6, 0.5)$ m. Numerical results obtained with the four meshes (left) and comparison with solution from [31] (right).

$(0.5, 6, 0.5)$ m. As observed, the displacement solution converges rapidly to the reference solution, and a locking-free behaviour is obtained even with coarse refinements. Moreover, the tetrahedral mesh provides almost the same deflection as the most refined hexahedral mesh, since both share equal grid spacing. A graphical comparison between transient deflection and pressure from different meshes can be seen in figure 3.16. The pressure or hydrostatic stress has been calculated as:

$$p = -\frac{\mathrm{tr}(\boldsymbol{\sigma})}{3}. \tag{3.9}$$

By refining the grid, higher pressures are predicted near the clamped face. Although there is no appearance of hourglassing instabilities in the mesh deformation, a minor spatial oscillation in the pressure close to the bottom is detected at time $t = 0.4$ s with all meshes. This results from the displacement-based formulation within nearly-incompressible situations, as mentioned earlier. Therefore, despite showing good performance on the displacement prediction when $\nu = 0.45$, specific mixed models would be required when aiming at further increasing the incompressibility constraint of the material.

3.4 Parallel performance

In this section, the parallel performance of the finite volume method is studied by conducting a memory-demanding simulation on a supercomputer using one to 64 nodes.

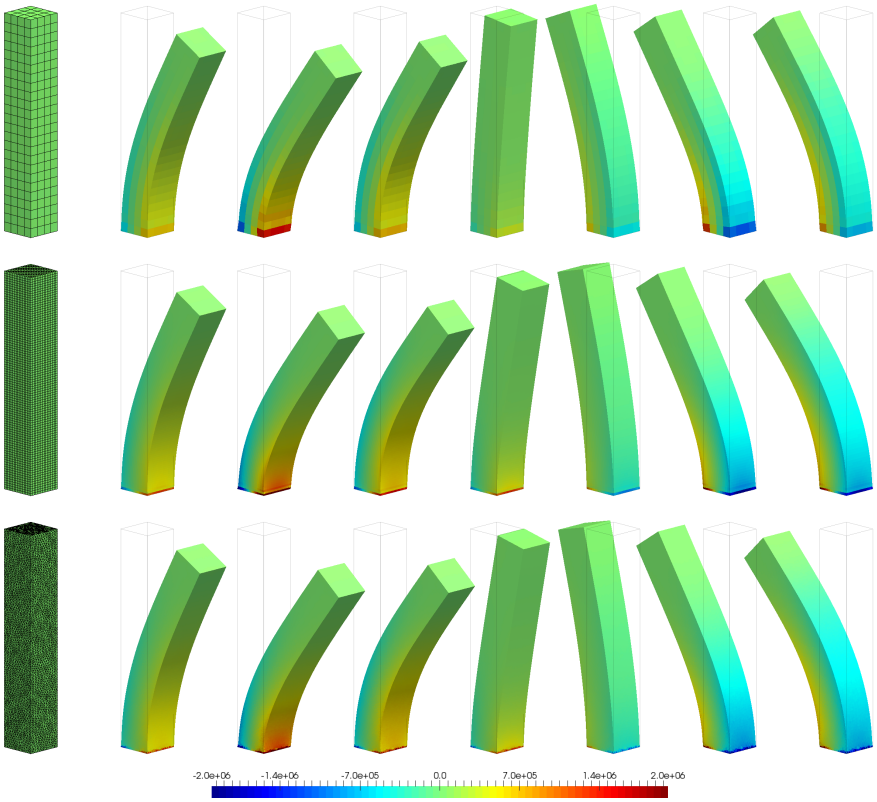

Figure 3.16: Case F: Instantaneous deformation with pressure distribution every 0.2 s, from 0 (left) to 1.6 s (right). From top to bottom: mesh 1, mesh 3 and mesh 4.

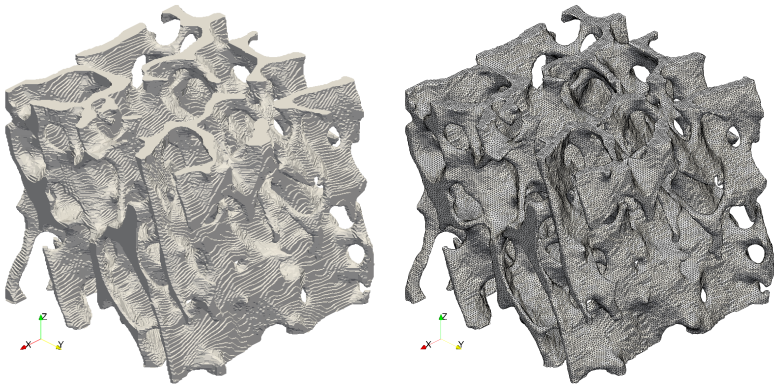

Figure 3.17: STL model of the trabecular bone specimen (left) and tetrahedral mesh 2 used in the computations with 2.4 million cell nodes (right).

As described in section 2.8, current methods have been implemented in TermoFluids C++ code [32], which utilises the MPI standard for distributed memory parallelisation. Consequently, following tests will be solved with only one processor per node to exclusively measure the efficiency of this kind of parallel systems. High performance computing cluster JFF2 from the Centre Tecnològic de Transferència de Calor (CTTC) will be used. This supercomputer has 128 nodes with 2 AMD Opteron 2376 quad-core processors at 2.3 GHz and 16 GB of RAM linked with the infiniband DDR 4X network.

The problem selected for this analysis concerns the compression of a kind of bone microstructure known as trabecular bone. This internal tissue of the skeleton is typically found at the end of long bones, near joints and in the inside of vertebrae. It consists of a complex porous network of trabecular rods resulting in a structure with high values of porosity [33]. Modelling trabecular specimens by high resolution finite element procedures has become a usual practice to investigate the mechanical properties of the bone within orthopaedic research [34]. Parallel computations allow for analysing larger specimens with higher resolution, and hence attention has been paid to continue enhancing parallel performance in this field [35].

Data of the trabecular bone specimen have been provided by the authors from [36], who used X-ray microtomography (microCT) to scan a human bone biopsy from the femoral neck. The resulting three-dimensional parallelepiped is about 4×4×4 mm and was transformed into a triangulated surface model in STL format. Figure 3.17 shows the original STL model and one of the unstructured tetrahedral meshes which has been

Table 3.8: Mesh quantities for the bone modelling and resulting compression force from the numerical experiment.

	Mesh 1	Mesh 2	Mesh 3	Mesh 4
# cell nodes $\times 10^6$	1.3	2.4	3.9	7.6
# face nodes $\times 10^6$	0.28	0.35	0.49	0.76
# degrees of freedom $\times 10^6$	4.7	8.2	13.2	25.2
Resultant force F_z [N]	84.7	83.4	83.3	81.7

used for the present study. In total four differently refined meshes have been tested. A summary of the number of nodes and degrees of freedom of each one is given in table 3.8. In the work developed by [37], a portion of the same specimen was reconstructed by voxel meshes and analysed by a sequential finite element method.

The presented test consists of subjecting the piece to static compression of 0.5 % in the z direction and measuring the reaction force F_z. To do so, a linear elastic model with $E = 15$ GPa and $\nu = 0.3$ is used. The bottom flat surface is fully clamped and the top one has a Dirichlet boundary condition with the known displacement in z direction and null in x and y. The rest of the surfaces are left with a traction-free boundary condition. Vertex interpolation is performed by the inverse distance weighting technique. Regarding the PETSc linear solver, the following configurations are employed:

- Segregated approach: A conjugate gradient iterative solver (cg) with the default algebraic multigrid preconditioner (amg). A relative residual of 10^{-7} for the convergence of fixed-point iterations is prescribed.
- Block-coupled approach: A generalised minimal residual method (lgmres) with block Jacobi preconditioning (bjacobi). Relative error tolerance of the solver is set to 10^{-7}.

The reaction force F_z resulting from the different grid spacings is outlined in table 3.8. A monotonic decrease in the force is observed as the mesh is refined. Nevertheless, it would be appropriate to run the case with a denser mesh to ensure a grid-independent solution. Figure 3.18 depicts the distribution of equivalent stress in the bone tissue from two different views. It can be appreciated how specific trabeculae become stress raisers as a result of their orientation and their thickness.

Non-scaled parallel problem The first study focuses on solving the pure compression of the coarsest mesh (mesh 1) with an increasing number of domain partitions and

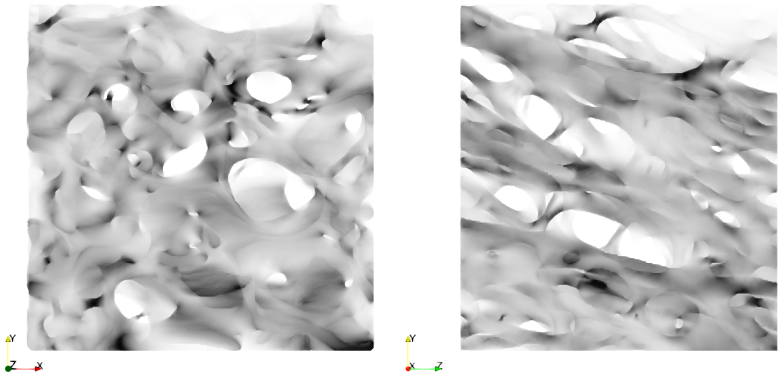

Figure 3.18: Volume rendering of equivalent stress in the compressed trabecular bone obtained with mesh 3.

Table 3.9: Number of iterations and execution times to solve the bone case with mesh 1 and an increasing number of processors. Iterations are referred to the fixed-point method in the segregated approach and the linear solver in the block-coupled approach. Simulations have been carried out at JFF2 supercomputer using one CPU core per node.

	Segregated							Block-coupled		
# nodes	1	2	4	8	16	32	64	16	32	64
# iterations	111	89	82	117	86	103	84	854	868	871
Time [min]	95	42	17	12	4.8	2.9	1.2	12	5.8	2.8

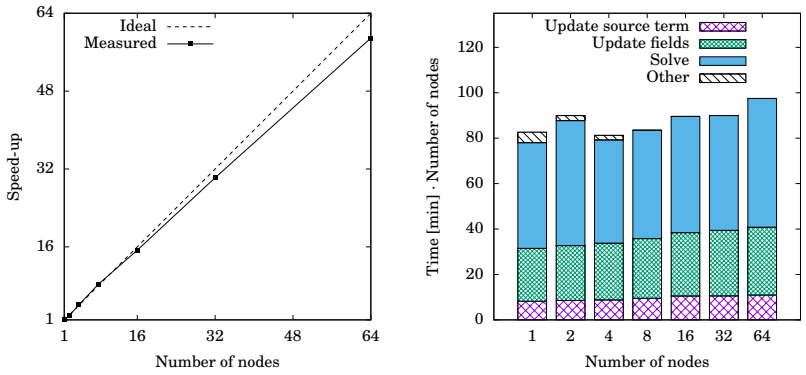

Figure 3.19: Speed-up (left) and CPU time (right) of the bone case using the segregated approach and mesh 1. Times have been scaled by the averaged number of iterations. Simulations have been carried out at JFF2 supercomputer.

processors. Therefore, the number of processors changes but not the computing weight in each one, which falls as more processors are used. This kind of non-scaled speed-up study provides information about the limit of scalability of the software and hardware.

This grid 1 has been chosen so as to fit, in terms of memory, in a single node when using the segregated method. Table 3.9 shows the number of fixed-point iterations from the segregated problem and the number of solver iterations from the coupled problem which are required to achieve the prescribed tolerance with a different number of partitions. Execution times for all cases are also tabulated. The memory limit was reached with the block-coupled method and 8 nodes and consequently the scaling is started with 16 nodes in this case.

As can be seen in the table 3.9, there is some variance in the number of iterations but without a clear tendency. In order to present an analysis more similar to a scalability test (which performs the same number of operations regardless of the number of processors) the execution times have been scaled to the averaged number of iterations. Only the portions of time which are affected by the number of iterations have been scaled. The resulting speed-ups are plotted in figures 3.19 and 3.20 (left). A high efficiency of the segregated procedure is observed up to 64 nodes, when 92 % parallel efficiency is achieved. On the other hand, the coupled program is showing superlinear speed-up as soon as the number of nodes rises. The program should handle a more substantial amount of memory in the calculations and is taking advantage of the memory hierarchy

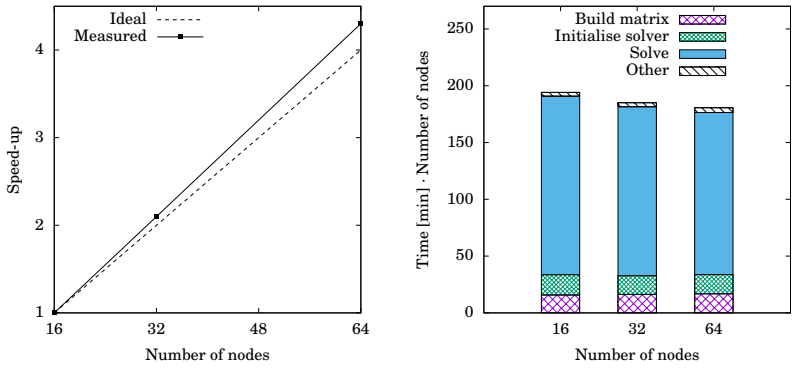

Figure 3.20: Speed-up (left) and CPU time (right) of the bone case using the block-coupled approach and mesh 1. Times have been scaled by the averaged number of iterations. Simulations have been carried out at JFF2 supercomputer.

architecture. The greater the number of nodes the larger the size of faster-access memory or cache. The necessary memory for vector operations could not be placed entirely in the cache with 16 nodes, slowing down the data access and inflating the scalability results with 32 and 64 nodes.

Figures 3.19 and 3.20 (right) show the total run time costs and the times for the major components of the computation, after scaling by iterations. Regarding the segregated approach, on average a 57 % of the time is consumed solving the linear system, 30 % updating the tensor fields $\nabla \boldsymbol{u}$ and $\boldsymbol{\sigma}$ and 11 % updating the source terms accordingly. Despite the fluctuations of the linear solver, it can be seen that the loss of efficiency is homogeneously distributed among these three main tasks. Meanwhile, the coupled arrangement dedicates 80 % of its solution time in the solver, 9 % in the solver initialisation and 9 % in the construction of the system matrix. The plot demonstrates that it is the resolution of the coupled linear system that takes the advantage of the cache effect.

It is important to pay attention to the total time spent by both methodologies, for example in table 3.9. In contrast to the comparisons between segregated and block-coupled methods of previous sections, here the former is faster than the latter. Unlike the preceding cases, this contains no bending, which reduces the coupling among displacement directions. Furthermore, the system size is significantly larger, and hence memory allocation and data access become a handicap for the coupled method.

Table 3.10: Number of iterations to solve the bone case with meshes 1, 2, 3 and 4 in 12, 21, 34 and 64 nodes, respectively, i.e. $3.9 \cdot 10^5$ degrees of freedom per node. Iterations are referred to the fixed-point method in the segregated approach and the linear solver in the block-coupled approach.

# nodes	12	21	34	64
Segregated	108	112	117	96
Block-coupled	850	1046	1226	1558

Scaled parallel problem A scaled speed-up test measures performance quantities of a given problem with increasing resolution. Compared with the non-scaled study above, this one aims at maintaining the same pressure on memory for all cases and hence avoid advantages from the memory architecture which can hide parallel inefficiencies of the code.

The uniformly refined meshes outlined in table 3.8 are decomposed to place approximately the same number of equations per processor. Using 64 nodes for the finest mesh 4 implies $3.9 \cdot 10^5$ degrees of freedom per node, and leads to 12, 21 and 34 partitions for meshes 1, 2 and 3, respectively.

Table 3.10 gives the number of iterations of both the segregated fixed-point algorithm and the block-coupled linear solver. The figures from the coupled tests show that the elasticity problem is becoming more challenging as the mesh is refined. This can be confirmed by observing figure 3.21 (right), where all principal time costs of the different experiments are displayed. The solver cost monotonically increases. With the segregated method, there is not such a trend in the number of outer iterations, but one would expect that the higher complexity of the problem should be affecting the cost of the solver call of each outer iteration. However, figure 3.21 (left) shows that time dedicated to the solver is weakly rising, and it is then hard to see if the segregated method faces a similar increase in difficulty when solving higher resolution cases. Extending the analysis to a greater number of processors could disclose better the parallel efficiency of using a segregated arrangement.

The mentioned observation was made as well by [35], who attributed the major challenge to the fact that the ratio of surface vertices to interior vertices enlarges as higher resolution meshes are used. With the current finite volume formulation would mean that the ratio of surface to volume nodes increases, and can be confirmed by examining table 3.8. Since a volume node has more neighbours than a surface node, more non-zeros per row appear in the system matrix with denser meshes.

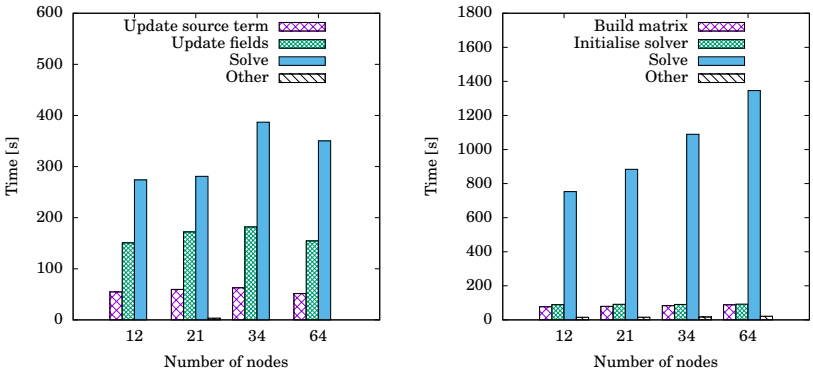

Figure 3.21: Execution times to solve the bone case with meshes 1, 2, 3 and 4 in 12, 21, 34 and 64 nodes. Segregated (left) and block-coupled approach (right).

3.5 Conclusions

The implemented linear thermoelasticity model based on advanced finite volume methods has been verified by simulating four available benchmark cases, which stress different features of solid mechanics: static elasticity, thermal expansion, vibration and structural damping. Spatial discretisation schemes were proved to provide second-order accuracy in the displacements, the primary variable, and first order in stresses. Second-order time integration schemes were tested, and the composite Bathe scheme was able to avoid the numerical instability shown with the Newmark integration and decreasing time steps. Furthermore, while mass proportional damping and Rayleigh damping dissipated the lowest vibration mode in similar magnitude, the stiffness contribution of the latter worked better removing the higher modes.

Regarding computational performance of the program, the Aitken acceleration technique proposed for the segregated approach was able to reduce the time cost by 10 to 76 % depending on the case. The block-coupled arrangement of the elasticity equations responded more effectively in this sense since a decrease between 72 and 97 % was achieved with respect to the classical segregated algorithm. Nonetheless, the segregated method should still be taken into consideration because it needs less effort on tuning the linear solver and fewer memory resources, two factors that can become a handicap when addressing complex problems with millions of degrees of freedom. This fact was observed when studying the parallel performance of the code. Additionally,

parallel efficiencies higher than 90 % were obtained up to 64 nodes with both system approaches.

On the other hand, the updated Lagrangian description used for hyperelastic materials has been verified too with the static finite deformation of a cantilever beam and the vibration of a nearly incompressible body. Both Saint Venant-Kirchhoff and neo-Hookean constitutive models have been employed. Numerical results demonstrated the influence of shear deformations on thick beams subjected to large deformations, and the locking-free response of the displacement-based formulation for almost incompressible materials.

References

[1] K.-J. Bathe and M. M. I. Baig. On a composite implicit time integration procedure for nonlinear dynamics. *Computers & Structures*, 83(31):2513 – 2524, 2005.

[2] P. J. Oliveira and C. J. Rente. Development and application of a finite volume method for static and transient stress analysis. *Proc. NAFEMS World Congress on Effective Engineering Analysis*, 1:297–309, 1999.

[3] A. K. Slone, C. Bailey, and M. Cross. Dynamic solid mechanics using finite volume methods. *Applied Mathematical Modelling*, 27(2):69–87, 2003.

[4] C. H. Lee, A. J. Gil, and J. Bonet. Development of a cell centred upwind finite volume algorithm for a new conservation law formulation in structural dynamics. *Computers & Structures*, 118:13 – 38, 2013.

[5] P. Cardiff, Ž. Tuković, P. D. Jaeger, M. Clancy, and A. Ivanković. A lagrangian cell-centred finite volume method for metal forming simulation. *International Journal for Numerical Methods in Engineering*, 109(13):1777–1803, 2017.

[6] P. Cardiff, Ž. Tuković, H. Jasak, and A. Ivanković. A block-coupled finite volume methodology for linear elasticity and unstructured meshes. *Computers & Structures*, 175:100–122, 2016.

[7] Ž. Tuković and H. Jasak. Updated lagrangian finite volume solver for large deformation dynamic response of elastic body. *Transactions of FAMENA*, 31:1–18, 2007.

[8] National Agency for Finite Element Methods & Standards (Great Britain). *The standard NAFEMS benchmarks*. NAFEMS, 1990.

[9] Dassault Systèmes. *Abaqus 6.12 Benchmarks Manual*, 2012.

[10] ANSYS, Inc. *ANSYS Mechanical APDL Verification Manual*, 2013.

[11] Siemens Product Lifecycle Management Software Inc. *NX Nastran 11 Verification Manual*, 2016.

[12] I. Demirdžić, S. Muzaferija, and M. Perić. Benchmark solutions of some structural analysis problems using the finite-volume method and multigrid acceleration. *International Journal for Numerical Methods in Engineering*, 40(10):1893–1908, 1997.

[13] D. Young and R. Felgar. *Tables of Characteristic Functions Representing Normal Modes of Vibration of a Beam*. Engineering research series. University of Texas, 1949.

[14] K.-J. Bathe. *Finite Element Procedures*. Prentice Hall, 1996.

[15] T. J. R. Hughes. *The Finite Element Method: Linear Static and Dynamic Finite Element Analysis*. Dover Publications, 2012.

[16] K.-J. Bathe. Conserving energy and momentum in nonlinear dynamics: A simple implicit time integration scheme. *Computers & Structures*, 85(7):437 – 445, 2007.

[17] K.-J. Bathe and G. Noh. Insight into an implicit time integration scheme for structural dynamics. *Computers & Structures*, 98-99:1 – 6, 2012.

[18] A. Idesman, H. Samajder, E. Aulisa, and P. Seshaiyer. Benchmark problems for wave propagation in elastic materials. *Computational Mechanics*, 43(6):797–814, 2009.

[19] M. Levinson. Free vibrations of a simply supported, rectangular plate: an exact elasticity solution. *Journal of Sound and Vibration*, 98(2):289–298, 1985.

[20] S. Otani. Nonlinear dynamic analysis of reinforced concrete building structures. *Canadian Journal of Civil Engineering*, 7(2):333–344, 1980.

[21] A. Alipour and F. Zareian. Study Rayleigh damping in structures; uncertainties and treatments. In *Proceedings of 14th World Conference on Earthquake Engineering*, Beijing, 2008.

[22] DNV GL. *Standard DNVGL-ST-F201, Dynamic Risers*, 2018.

[23] P. J. Roache. Quantification of uncertainty in computational fluid dynamics. *Annual Review of Fluid Mechanics*, 29(1):123–160, 1997.

[24] M. Kjell. Numerical results from large deflection beam and frame problems analysed by means of elliptic integrals. *International Journal for Numerical Methods in Engineering*, 17(1):145–153, 1981.

[25] J. Bonet, A. J. Gil, and R. Ortigosa. A computational framework for polyconvex large strain elasticity. *Computer Methods in Applied Mechanics and Engineering*, 283:1061 – 1094, 2015.

[26] D. G. Fertis. *Nonlinear Structural Engineering*. Springer, 2006.

[27] T. Kant and A. Gupta. A finite element model for a higher-order shear-deformable beam theory. *Journal of Sound and Vibration*, 125(2):193 – 202, 1988.

[28] H. Irschik. Enhancement of elementary beam theories in order to obtain exact solutions for elastic rectangular beams. *Mechanics Research Communications*, 68:46 – 51, 2015.

[29] E. A. de Souza Neto, D. Peric, and D. R. Owen. *Computational methods for plasticity: theory and applications*. John Wiley & Sons, 2011.

[30] I. Bijelonja, I. Demirdžić, and S. Muzaferija. A finite volume method for large strain analysis of incompressible hyperelastic materials. *International Journal for Numerical Methods in Engineering*, 64(12):1594–1609, 2005.

[31] J. Haider, C. H. Lee, A. J. Gil, and J. Bonet. A first-order hyperbolic framework for large strain computational solid dynamics: An upwind cell centred Total Lagrangian scheme. *International Journal for Numerical Methods in Engineering*, 109(3):407–456, 2016.

[32] Termo Fluids S.L. http://www.termofluids.com/.

[33] S. Cowin. *Bone Mechanics Handbook, Second Edition*. Taylor & Francis, 2001.

[34] E. Klintström, B. Klintström, R. Moreno, T. B. Brismar, D. H. Pahr, and Ö. Smedby. Predicting trabecular bone stiffness from clinical cone-beam CT and HR-pQCT data; an in vitro study using finite element analysis. *PloS one*, 11(8):e0161101, 2016.

[35] M. F. Adams, H. H. Bayraktar, T. M. Keaveny, and P. Papadopoulos. Ultrascalable implicit finite element analyses in solid mechanics with over a half a billion degrees of freedom. In *Supercomputing, 2004. Proceedings of the ACM/IEEE SC2004 Conference*, pages 34–34, 2004.

[36] E. Perilli and F. Baruffaldi. Proposal for shared collections of X-ray micro CT datasets of bone specimens. In *International Conference on Computational Bioengineering*, Zaragoza, 2003.

[37] A. Düster, J. Parvizian, Z. Yang, and E. Rank. The finite cell method for three-dimensional problems of solid mechanics. *Computer Methods in Applied Mechanics and Engineering*, 197(45):3768 – 3782, 2008.

4

Fluid-structure coupling tools

4.1 Introduction

Fluid-structure interaction (FSI) refers to problems with mutual dependence between a fluid flow and a moving structure. The structure motion depends on the load of the surrounding flow, but the flow behaviour depends on the shape and motion of the structure. There is a wide range of engineering, scientific and medical applications in which such interaction is produced. Fluttering and static deformation of aircraft and turbomachinery, dynamics of lightweight structures such as airbags or parachutes, and the biomechanical response of blood pumping and arterial flow, are some FSI examples [1].

Therefore, high-fidelity FSI prediction methods have become an important tool within the design process of contemporary engineering applications. The difficulty in modelling the FSI systems analytically, due to their inherent non-linearity, and the limitations in scope of laboratory experiments have fostered the development of numerical methods for this purpose.

In most cases, the solid computational domain follows the material particles with a Lagrangian description. Concerning the fluid domain, there are two classes of approaches: the non-conforming grid methods (or interface-capturing) and the conforming grid methods (or interface-tracking) [2, 3]. The non-conforming mesh methods impose the solid interface conditions as constraints on a Eulerian fluid model, without requiring any mesh update [4, 5]. On the other hand, in a conforming-mesh method the fluid grid is adjusted to the new shape defined by the solid boundaries. Most of these cases can be handled by moving the grid points and using an arbitrary Lagrangian-Eulerian

(ALE) formulation in the governing equations [6, 7]. However, remeshing and solution mapping might be needed in extreme situations, such as in contact between solids [8]. By conforming the fluid mesh, the element resolution near the solid moving surface is automatically controlled, and accurate predictions in that critical flow region are obtained.

Another general classification of numerical procedures for FSI is based upon the arrangement and coupling of both fluid-solid systems of equations. The monolithic approach uses a single mathematical framework and system solver to solve both media simultaneously [9, 10]. In contrast, partitioned methods use different mesh discretisations and separate solvers for fluid and structural equations and adopt a communication scheme to account for the interaction of the domains [11, 12]. While they introduce the additional challenge of coordinating and coupling two independent programs, they allow for integrating already available disciplinary methods that adapt best to each sub-problem phenomenology.

Partitioned methods can be further divided into explicit (or loosely coupled) and implicit (or strongly coupled). In the former, the fluid and structural equations are solved in sequence and only once at every time step [13]. Consequently, explicit methods do not satisfy the exact coupling condition at the fluid-solid interface. This can lead to convergence difficulties when the structure is light compared with the fluid and therefore becomes very sensitive to changes in the fluid forces. Implicit methods enforce the interface equilibrium by means of coupling iterations between both domains at each time step, becoming computationally expensive but more robust and suitable for the mentioned strongly coupled problems. Fixed-point (Gauss-Seidel or Jacobi) iterations [14] and Newton-based methods [15] are the most common techniques to carry out the FSI coupling iterations.

In this work, a partitioned approach with a Lagrangian description of the solid and an ALE description of an incompressible fluid is followed. Matching meshes of both media at the interface are assumed. A semi-implicit algorithm, which takes advantage of the projection method used in the in-house flow solver, has been designed to ensure numerical stability of strongly coupled problems at a moderate computational cost.

This chapter aims at presenting the numerical tools needed to deal with FSI analysis, namely: the ALE fluid model (section 4.2), the moving-mesh technique (section 4.3) and the fluid-solid partitioned algorithm (section 4.4). The whole method is enclosed in TermoFluids code [16]. To showcase the potentiality of the proposed methodology, an industrial FSI application is studied with a simplified structural model in section 4.5.

4.2 Fluid model

Fluid flow is assumed isothermal and incompressible, hence the modelisation with Navier-Stokes equations. Integrating over a moving control volume $V(t)$ leads to an arbitrary Lagrangian-Eulerian (ALE) formulation of the governing equations

$$\int_{V(t)} \nabla \cdot \dot{\boldsymbol{u}} dV = 0\,, \tag{4.1}$$

$$\int_{V(t)} \rho \frac{\partial \dot{\boldsymbol{u}}}{\partial t} dV + \int_{V(t)} \rho \dot{\boldsymbol{c}} \cdot \nabla \dot{\boldsymbol{u}} dV = \int_{V(t)} \nabla \cdot \boldsymbol{\sigma} dV\,, \tag{4.2}$$

where ρ is the density, p is the pressure, $\dot{\boldsymbol{u}}$ is the fluid velocity, and $\dot{\boldsymbol{c}}$ is the total convective velocity, which depends on the fluid velocity and the velocity of the moving reference $\dot{\boldsymbol{u}}_g$ as $\dot{\boldsymbol{c}} = \dot{\boldsymbol{u}} - \dot{\boldsymbol{u}}_g$. The stress tensor $\boldsymbol{\sigma}$ is defined by the constitutive equation of a Newtonian fluid as:

$$\boldsymbol{\sigma} = -p\boldsymbol{I} + \mu_f \left[\nabla \dot{\boldsymbol{u}} + (\nabla \dot{\boldsymbol{u}})^T \right], \tag{4.3}$$

where μ_f is the dynamic viscosity of the fluid. Applying the constitutive model and the divergence theorem to equation 4.2 yields the following form of the momentum conservation law

$$\int_{V(t)} \rho \frac{\partial \dot{\boldsymbol{u}}}{\partial t} dV + \int_{S(t)} \dot{\boldsymbol{u}} \left(\rho \dot{\boldsymbol{c}} \cdot \boldsymbol{n} \right) dS = \int_{S(t)} \mu_f \nabla \dot{\boldsymbol{u}} \cdot \boldsymbol{n} dS - \int_{S(t)} p \cdot \boldsymbol{n} dS\,. \tag{4.4}$$

A finite volume method is used to solve the governing equations. Second-order symmetry-preserving schemes are followed to discretise the equations on a collocated unstructured grid arrangement. These schemes guarantee the conservation of kinetic energy in the discrete representation [17], a crucial feature when dealing with turbulent flows [18].

An explicit time integration discretises the convective and diffusive terms of the momentum equation, whereas an implicit scheme is used for the pressure gradient term. The fractional-step projection method [19] is intended for decoupling and solving pressure and velocity with a three-step solution procedure. First, a predicted velocity field $\dot{\boldsymbol{u}}^p$ is evaluated from equation 4.4 without considering the incompressibility constraint. The simplest form can be obtained using a first-order explicit time scheme:

$$\dot{\boldsymbol{u}}_P^p = \frac{1}{V_P^{n+1}} \left[\dot{\boldsymbol{u}}_P^n V_P^n - \sum_f \dot{\boldsymbol{u}}_f^n \left(\dot{\boldsymbol{c}}_f^n \cdot \boldsymbol{n}_f^n \right) S_f^n \Delta t^{n+1} - \sum_f \frac{\mu_f}{\rho} (\nabla \dot{\boldsymbol{u}})_f^n \cdot \boldsymbol{n}_f^n S_f^n \Delta t^{n+1} \right]. \tag{4.5}$$

Pressure distribution at t^{n+1} can then be found by solving the Poisson's equation

$$\Delta p^{n+1} = \frac{1}{\Delta t^{n+1}} \nabla \cdot \dot{\boldsymbol{u}}^{p} , \tag{4.6}$$

whose spatially discretised version reads

$$\sum_{f} (\nabla p)_{f}^{n+1} \cdot \boldsymbol{n}_{f}^{n} S_{f}^{n} \Delta t^{n+1} = \sum_{f} \dot{\boldsymbol{u}}_{f}^{p} \cdot \boldsymbol{n}_{f}^{n} S_{f}^{n} . \tag{4.7}$$

The pressure is finally used to correct the new velocity at every cell P

$$\dot{\boldsymbol{u}}_{P}^{n+1} = \dot{\boldsymbol{u}}_{P}^{p} - \Delta t^{n+1} (\nabla p)_{P}^{n+1} . \tag{4.8}$$

Large Eddy Simulation (LES) models are used for turbulence. In LES, the largest scales of the flow are solved while the small-scale motions are emulated by a subgrid-scale model, reducing the computational cost of direct numerical simulations. Navier-Stokes equations are filtered spatially, and a modelisation is required for the filtered non-linear convective term. To do so, a subgrid-scale stress tensor is formulated as a function of a subgrid-scale viscosity ν_{sgs} [20]. In this work, such viscosity is calculated according to the wall-adapting eddy viscosity model [21].

More details on the in-house finite volume method for incompressible fluids can be found in [18, 22].

4.3 Fluid mesh motion

The automatic deforming mesh method adjusts the position of the internal mesh points to accommodate changes in the domain boundary without involving topological alterations. In this case, it is the fluid mesh that has to be adapted to the motion of the structure. Two different automatic methods have been implemented to tackle these cases, both taking advantage of the parallel unstructured cell-centred finite volume framework already available in the in-house TermoFluids code [16]: the pseudo-solid method and the Laplacian method.

Both moving mesh methods solve for the incremental displacement that connects two consecutive time-levels,

$$\boldsymbol{x}^{n} = \boldsymbol{x}^{n-1} + \Delta \boldsymbol{u}_{g}^{n} . \tag{4.9}$$

The pseudo-solid method treats the fluid domain as a linear elastic material, and static equilibrium determines the deformation of the internal nodes of the mesh (see

equation 2.36):

$$\int_S \boldsymbol{n} \cdot \left\{ \mu \nabla \left(\Delta \boldsymbol{u}_g \right) + \mu \left[\nabla \left(\Delta \boldsymbol{u}_g \right) \right]^T + \lambda \mathrm{tr} \left(\nabla \left(\Delta \boldsymbol{u}_g \right) \right) \boldsymbol{I} \right\} dS = 0 \,. \tag{4.10}$$

The Laplacian or pure diffusive method can be obtained by neglecting the terms that relate different displacement directions from equation 4.10,

$$\int_S \mu \boldsymbol{n} \cdot \nabla \left(\Delta \boldsymbol{u}_g \right) dS = 0 \,. \tag{4.11}$$

Although this Laplacian method does not allow rotation, which may be a necessity under some circumstances, it defines three uncoupled systems, one for each direction, that can be solved at a significantly lower cost than the pseudo-solid coupled system.

Both equations 4.10 and 4.11 are solved by the finite volume methodologies described in chapter 2, under boundary conditions of Dirichlet type (moving or fixed boundaries) or Neumann (sliding or free boundaries). One of the interpolation procedures of section 2.6.2 defines the vertex displacement solution needed for actually moving the grid.

The main difficulty in tackling cases with variable geometry is maintaining the mesh quality. According to the original solid isotropic formulation, the implemented methods would depend on two parameters to play with resulting mesh quality: ν and E. The former will be set to zero and the latter will be smartly tuned so as to keep good quality in critical regions of the domain. Here, a volume-based stiffening is proposed to define a local E at every cell element and at every time step as

$$E_P^n = \left(V_P^n \right)^{-\chi} , \quad \chi \geqslant 0 \,. \tag{4.12}$$

Consequently, the small cells, which are generally located at numerically or physically meaningful areas, become stiffer and harder to deform and the major distortion is absorbed by the softer large cells, which can readily tolerate the deformation without severely degrading their quality. Other volume-based stiffening were used within pseudo-solid methods in [23, 24]. In [25], local diffusivity μ was modified in a Laplacian method with respect to quality parameters and the distance to the moving boundary.

In order to compare both mesh update methods, the case of a flat plate moving in a two-dimensional square domain, previously reported by [23, 24], is carried out. The initial undeformed mesh is presented in figure 4.1. The square side is 2, plate length is 1 and plate thickness is 0.02. The prescribed motions of the internal boundary have been divided into 50 uniform steps, which are useful to continuously update the stiffening

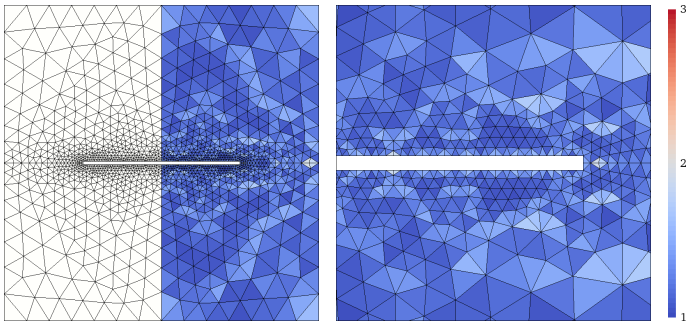

Figure 4.1: Two-dimensional domain for moving mesh tests. The field measures the grid quality as the highest edge ratio of every triangle.

and the geometrical data of Laplacian and elastic systems. Sliding movement of the vertices is allowed at the square walls.

The first test consists of translating the structure 0.5 non-dimensional units towards the upper wall. Figure 4.2 presents the final mesh obtained with both methods. The results demonstrate that volume stiffening may become mandatory to avoid excessive quality worsening or even invalid elements near the moving boundary. Since there is translation only, the Laplacian method can perform just as well as the pseudo-solid method. However, the second test shows the advantages of the pseudo-solid procedure when a rotation of the boundary is involved. The plate is now subjected to a pure bending deformation with no elongation. With a Laplacian approach, tangling near the structure tips appears, whereas with the elastic equations, cells around the structure practically follow a rigid motion and element distortion is concentrated in the bottom corners of the domain (see figure 4.3).

Space conservation law Regardless of the moving mesh method, special attention should be paid to the evaluation of the grid velocities $\dot{\boldsymbol{u}}_g$ present in the ALE formulation of the fluid system (equation 4.2). They are required to be consistent with the space conservation law (SCL) in order to avoid numerical errors in the form of artificial mass sources [26].

The continuous SCL is derived by taking the ALE continuum equation and assuming uniform fields of velocity and density:

$$\frac{\partial}{\partial t}\int_V dV - \int_S \boldsymbol{n}\cdot\dot{\boldsymbol{u}}_g dS = 0\,. \tag{4.13}$$

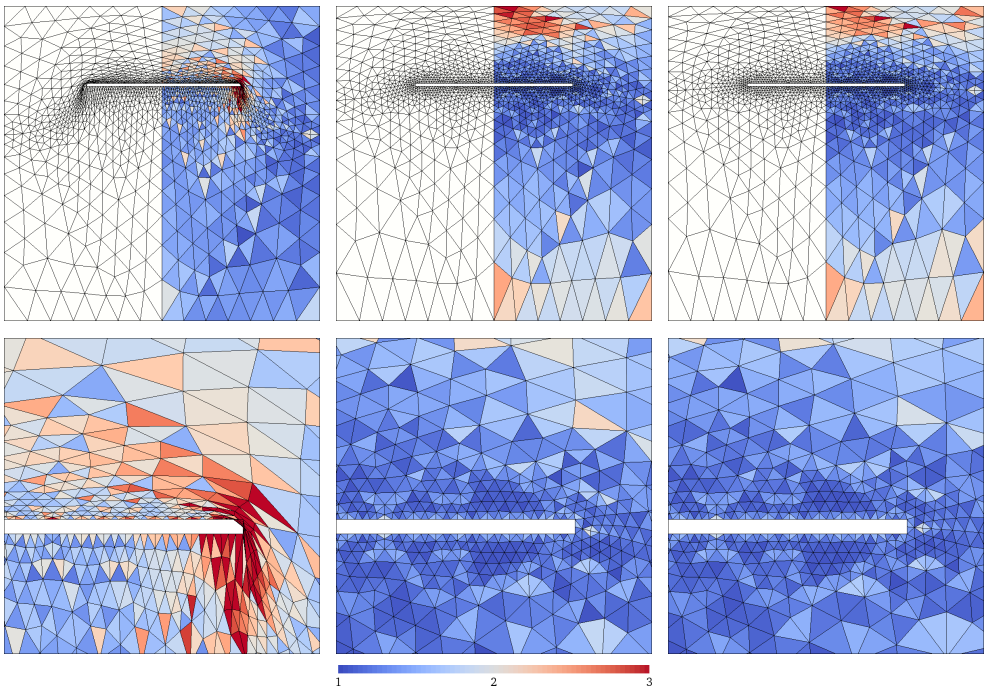

Figure 4.2: Translation test. From left to right: pseudo-solid with no tuning, pseudo-solid with $\chi = 1$ and Laplacian with with $\chi = 1$. For all cases, $\nu = 0$. The field measures the grid quality as the highest edge ratio of every triangle.

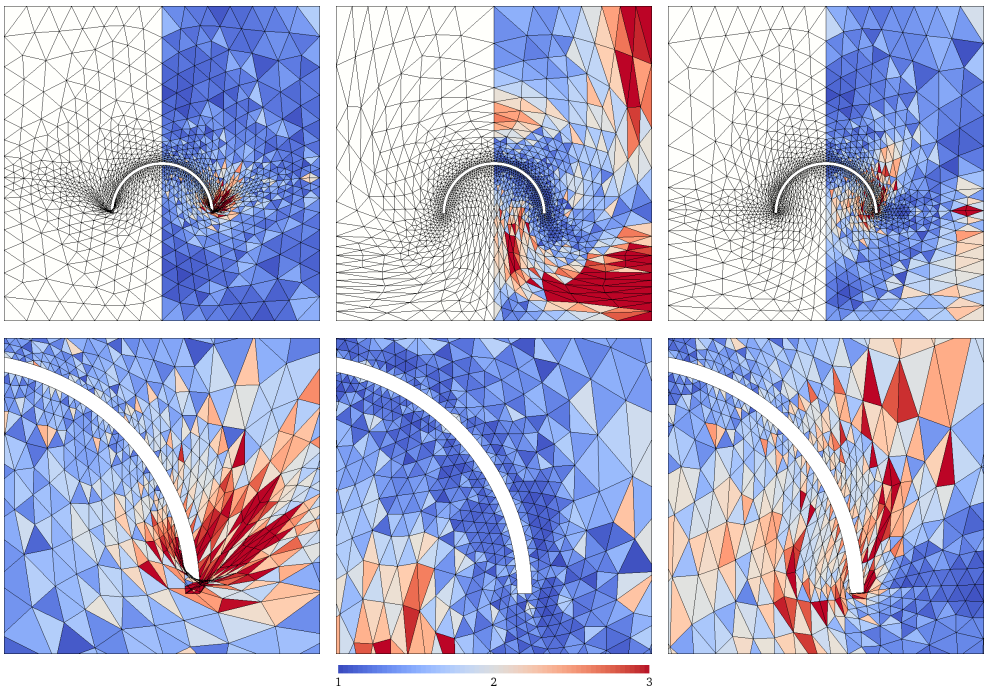

Figure 4.3: Bending test. From left to right: pseudo-solid with no tuning, pseudo-solid with $\chi = 2$ and Laplacian with with $\chi = 2$. For all cases, $\nu = 0$. The field measures the grid quality as the highest edge ratio of every triangle.

The discretised counterpart of the SCL, considering the same numerical schemes presented for the fluid governing equations, is:

$$\frac{V_P^{n+1} - V_P^n}{\Delta t^{n+1}} - \sum_f \underbrace{\boldsymbol{n}_f^n \cdot (\dot{\boldsymbol{u}}_g)_f^n S_f^n}_{\dot{V}_g^n} = 0, \tag{4.14}$$

where $\dot{V}_g^n$ is the volumetric flow rate due to the grid motion and will be carefully calculated in order to satisfy equation 4.14.

The difference between cell volumes is equivalent to the volume swept by all cell faces

$$V_P^{n+1} - V_P^n = \sum_f \delta V_f^n, \tag{4.15}$$

where δV_f^n can be exactly computed by integrating the flux crossing a triangular facet that moves linearly from t^n to t^{n+1} [27]. A graphical representation of the moving face is shown in figure 4.4. The explicit formula reads

$$\delta V_f^n = \frac{1}{3}(\Delta \boldsymbol{u}_A + \Delta \boldsymbol{u}_B + \Delta \boldsymbol{u}_C) \cdot \boldsymbol{\eta}, \tag{4.16}$$

$$\boldsymbol{\eta} = \frac{1}{6}\left[\overline{C_0A_0} \times \overline{C_0B_0} + \overline{CA} \times \overline{CB} + \frac{1}{2}\left(\overline{C_0A_0} \times \overline{CB} + \overline{CA} \times \overline{C_0B_0}\right)\right], \tag{4.17}$$

where for example $\overline{C_0A_0} = \boldsymbol{x}_{A_0} - \boldsymbol{x}_{C_0}$. Faces with more than three vertices are decomposed into triangles to apply the same formula.

Combination of equations 4.14 and 4.15 yields:

$$\frac{1}{\Delta t^{n+1}} \sum_f \delta V_f^n = \sum_f \dot{V}_g^n. \tag{4.18}$$

Hence, the face fluxes caused by the mesh motion for first-order time schemes are calculated using the following expression

$$\dot{V}_g^n = \frac{\delta V_f^n}{\Delta t^{n+1}}. \tag{4.19}$$

The extension to higher-order time schemes is straightforward.

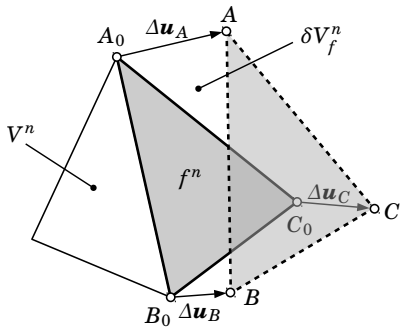

Figure 4.4: Volume swept δV_f^n by a triangular facet of a control volume.

4.4 Fluid-solid coupling algorithm

Kinematic and dynamic equilibrium should be satisfied on the fluid-solid interface. In the partitioned approach, equal velocities are imposed on the fluid boundary condition as

$$\dot{\boldsymbol{u}}_f = \frac{\partial \boldsymbol{u}_s}{\partial t}, \tag{4.20}$$

whereas equal stresses are imposed on the solid boundary condition as

$$\boldsymbol{n} \cdot \boldsymbol{\sigma}_s = \boldsymbol{n} \cdot \boldsymbol{\sigma}_f = \boldsymbol{t}_f, \tag{4.21}$$

where $\boldsymbol{n}$ is the unit normal vector at the interface. Thermal energy exchange has been ignored.

Having updated the boundary velocity with $\boldsymbol{u}_s$, the fluid problem can provide new values of pressure and velocity in the fluid medium and, therefore, define a new load distribution on the solid surface $\boldsymbol{t}_f$. The discrete equations of the fluid can be interpreted as an interface function according to $\boldsymbol{t}_f = \boldsymbol{F}(\boldsymbol{u}_s)$. Likewise, the structure system solves for the new deformation $\boldsymbol{u}_s$ derived from the fluid load: $\boldsymbol{u}_s = \boldsymbol{S}(\boldsymbol{t_f})$. Therefore, the coupled fluid-structure system of equations reduces into an interface problem of the form

$$\boldsymbol{S} \circ \boldsymbol{F}(\boldsymbol{u}_s) = \boldsymbol{u}_s \quad \text{or} \quad \boldsymbol{S} \circ \boldsymbol{F}(\boldsymbol{u}_s) - \boldsymbol{u}_s = 0. \tag{4.22}$$

An implicit partitioned coupled system needs to solve equation 4.22 by an iterative process. Despite the numerical stability shown by implicit methods, they are compu-

tationally expensive because fluid and solid equations should be solved several times at every time step. To alleviate this, here a semi-implicit approach to handle strongly coupled problems is developed. It leverages the fluid projection method to implicitly couple only the pressure term to the structure, without moving the mesh nor correcting the velocities at every fluid coupling iteration. The importance of considering the pressure implicitly in the solid side to avoid numerical instability has been demonstrated in previous works [11, 28].

The fixed-point form of the interface problem (equation 4.22) is managed by a block Gauss-Seidel method with Afitken's Δ^2 dynamic acceleration. This relaxation mitigates possible convergence issues of the Gauss-Seidel method and reduces the number of required iterations [6, 14]. Before updating the fluid velocity boundary condition, the solid displacement at the interface is relaxed as was described for the segregated method of the solid, equations 2.70 and 2.72. The difference from that method lies in the fact that here a recursive formulation is used for the relaxation factor

$$\gamma^{k+1} = -\gamma^{k} \frac{[r]^{k} \cdot \left([r]^{k+1} - [r]^{k}\right)}{\left|[r]^{k+1} - [r]\right|^{2}}, \tag{4.23}$$

and relaxation is applied at every coupling iteration.

The semi-implicit algorithm for a given time step can be summarised in the following sequence:

1. Set the fluid-solid coupling iteration $k = 0$.
2. Update the fluid Poisson's system matrix of equation 4.7 with the new mesh.
3. Evaluate the fluid predicted velocity with equation 4.5.
4. Increase the fluid-solid coupling iteration $k + 1$.
5. Update the fluid velocity boundary condition $\dot{\boldsymbol{u}}_f^{k+1}$ with the last interface displacement.
6. Solve the Poisson's equation for the fluid pressure p^{k+1}, equation 4.7.
7. Update the fluid load on the solid boundary $\boldsymbol{t}_f^{k+1}$ with the last fluid pressure.
8. Solve the solid system $\boldsymbol{u}_s^{k+1}$.
9. Evaluate the residual, relax the interface displacement solution $\tilde{\boldsymbol{u}}_s^{k+1}$ and return to step 4 if the residual is greater than the coupling numerical tolerance.

10. Correct the velocities with the converged pressure and equation 4.8.

11. Adapt the fluid mesh to the solid converged displacement and evaluate the volumetric flow rate $\dot{V}_g^n$ with equations 4.19 and 4.16.

4.5 Flow through reed valves

Design of reed valves is a challenging task and is of great relevance for the overall performance of hermetic reciprocating compressors [29, 30]. They are involved in suction and discharge processes, which are responsible for nearly half of the total thermodynamic losses of the compressor [31]. But besides efficiency, they also affect reliability, since the repetitive collision loading of the valves is the most common cause of failure of the machine [32, 33]. Reed valves are used as well in two-stroke engines [34, 35] and hydraulic applications [36, 37], and their operation is similar to that of heart valves [38].

The problem presents different complexities such as high pressure and velocity gradients, flow detachment, turbulence, collisions and fluid-structure multi-physics coupling. Traditionally the coupled process has been tackled by means of one-dimensional lumped models, which have been proved to work reasonably well for broad design studies [29,39]. However, a more detailed approach needs to be considered in order to fully understand the flow topology and optimise valve design. In the last years, following an enhance in computational resources, a growing research on 3D computational fluid dynamics (CFD) simulations for valve flow has been carried out. A verified FSI model, which strongly couples both 3D CFD and finite element structural procedures, was thoroughly explained and used for reed valves in [40]. Besides, different CFD analysis considering FSI have been performed which include comparison with experimental data. Some examples can be found in [41–44]. They mostly focused on the valve response rather than on the description of the numerical methodology or the results regarding the flow behaviour.

The objective of the following numerical experiment is to demonstrate the validity of the previously described tools to analyse complex fluid-solid phenomena of a real industrial application, the turbulent flow through a reed valve. Therefore, the partitioned semi-implicit algorithm, with the turbulent ALE fluid model, is to be used. The response of the structure will be solved using the mode superposition method combined with a plate model. The exercise should be read as a first step towards the final FSI numerical platform, which will integrate the finite volume solver for structures presented

in chapters 2 and 3.

First, the mathematical model for the reed valve is described in section 4.5.1. Next, sections 4.5.2 and 4.5.3 define the specific case parameters, whereas section 4.5.4 summarises the obtained results.

4.5.1 Plate model

Consider the reed valve as an arbitrarily shaped plate with uniform thickness h, where (x,y) are the coordinates on its mid-surface and z is the coordinate in the thickness direction. Such structure will be modelled by the isotropic Kirchhoff-Love plate theory, which is suitable for thin plates subjected to transverse loads t_z and small strains and rotations. After applying the kinematics assumptions, the problem becomes two-dimensional in (x,y):

$$\frac{Eh^3}{12\left(1-\nu^2\right)}\nabla^4 u_z(x,y,t)+2\rho h\ddot{u}_z(x,y,t)=t_z(x,y,t)\,, \tag{4.24}$$

where u_z is the normal displacement. Displacements in the other directions can be easily obtained from u_z:

$$u_x=(z_{mid}-z)\frac{\partial u_z}{\partial x}\,,\quad u_x=(z_{mid}-z)\frac{\partial u_z}{\partial x}\,, \tag{4.25}$$

where z_{mid} sets the position of the plate mid-plane.

In order to reduce the computational cost of a direct time integration, the mode superposition method for linear analysis is followed. Thus, the motion of a vibration system can be approximated by a combination of a limited number M of its free vibration modes [45, 46]:

$$u_z(x,y,t)\approx\sum_{m=1}^{M}q_m(t)\phi_m(x,y)\,, \tag{4.26}$$

where $\phi_m(x,y)$ and q_m are the normal deformation pattern and the generalised coordinate corresponding to the vibration mode m, respectively. Mode shapes $\phi_m(x,y)$ and natural radial frequencies ω_m have to be obtained beforehand by solving the eigenvalue problem of the free vibration equation of the system. Imposing the mode superposition to equation 4.24 and considering their orthogonality ($\int_S \phi_m\phi_n dS=0$ if $m\neq n$) transform the original continuum equation into a set of M independent equations, one for each

mode, written in terms of the generalised coordinates [30]:

$$\ddot{q}_m(t) + \omega_m^2 q_m(t) = \frac{\int_S \phi_m(x,y) t_z(x,y,t) dS}{\rho h \int_S \phi_m^2(x,y) dS}. \tag{4.27}$$

Three different sources can cause transverse load in the reed system: fluid pressure and shear stress $\boldsymbol{n} \cdot \boldsymbol{\sigma}$ (equation 4.3), gravitational force $\boldsymbol{g}$ and impact force with the seat I, considered totally perpendicular. If $\boldsymbol{n}$ is the unit normal outward to the plate in the current configuration, the transverse load results in:

$$t_z(x,y,t) = (0,0,1) \cdot \left[\boldsymbol{n}(x,y,t) \cdot \boldsymbol{\sigma}(x,y,t) + \rho \boldsymbol{g} h \right] + \frac{I(x,y,t)}{dS}. \tag{4.28}$$

Any other force, such as reed pre-tension or stiction force, is omitted at this stage. Thus, the total energy of the valve, which is the sum of kinetic energy e_T, strain energy e_K and gravitational potential energy e_G, should balance the work done by fluid and impact forces. The system reduction allows for evaluating these energies by employing the generalised coordinates as:

$$e_T = \frac{\rho h}{2} \sum_{m=1}^{M} \dot{q}_m^2 \int_S \phi_m^2 dS, \tag{4.29}$$

$$e_K = \frac{\rho h}{2} \sum_{m=1}^{M} \omega_m^2 q_m^2 \int_S \phi_m^2 dS, \tag{4.30}$$

$$e_G = -(0,0,1) \cdot \boldsymbol{g} \rho h \sum_{m=1}^{M} q_m \int_S \phi_m dS. \tag{4.31}$$

The numerical resolution of the system of M equations 4.27 is conducted by an integration over both upper and bottom surfaces of the valve plate. Once the load t_z on the face elements of the structure is known, the midpoint rule is used to approximate the right-hand side of equations 4.27. Then, a trapezoidal rule discretises in time the remaining terms and q_m solutions can be found.

The penalty method models the frictionless contact with the rigid seat. When a valve element penetrates the seat, a local impact force proportional to this penetration δ_i is recalled:

$$I_i = \begin{cases} \kappa_i \delta_i & \text{if } \delta_i > 0 \\ 0 & \text{if } \delta_i \leqslant 0, \end{cases} \tag{4.32}$$

where κ_i is the penalty stiffness. The higher the stiffness, the better the accuracy (less

penetration), but the more numerically unstable. In this case, it is sized according to [47, 48] recommendation:

$$\kappa_i = f_{SI} \frac{K S_i^2}{S_i h}, \tag{4.33}$$

where K is the plate bulk modulus and f_{SI} is a scale factor which has been set here to 1, thanks to the small time steps employed. Like the fluid pressure force, the impact force is integrated implicitly in the equilibrium equation and thus, an iterative process is required. Theoretical convergence and energy conservation through temporal refinement of the penalty method is proven in [49, 50].

4.5.2 Case definition

A comparative study of the experimental case carried out in [51] is presented here. It was focused on the fluttering motion of a reed valve under the load of a developed and stationary air pipe flux. The set-up consists of a feeding tube with $d = 34.9$ mm in diameter, closed by a reed reed valve at the end, and a space between two plates downstream of the valve. The valve thickness is $h = 0.4$ mm and its diameter D is 1.3 times the orifice diameter d. Figure 4.5 shows the other dimensions of the valve as well as those of the computational domain chosen for the simulations. Inlet and outlet boundaries have been located sufficiently far from the valve to avoid their influence in the solution.

The temperature of the air is 25 ºC, ambient pressure is defined at the outlet, and gravity is $\boldsymbol{g} = (0, 0, 9.81)$ m/s^2. The physical properties of the flexible valve are set to be: $\rho = 7850$ kg/m^3, $\nu = 0.3$ and $E = 2 \cdot 10^{11}$ Pa. The original authors reproduced the same experiment for Reynolds numbers ranging from 2,000 to 12,000. In this work, the inlet velocity of the fluid is determined such that Reynolds number is 10,000:

$$Re = \frac{\rho_f \bar{u}_z d}{\mu_f}, \tag{4.34}$$

where $\bar{u}_z$ is the axial bulk velocity. The inlet velocity is fixed following the profile of a developed pipe flow. This averaged velocity profile has been approximated by that corresponding to a similar value of Re [52] and is outlined in figure 4.6.

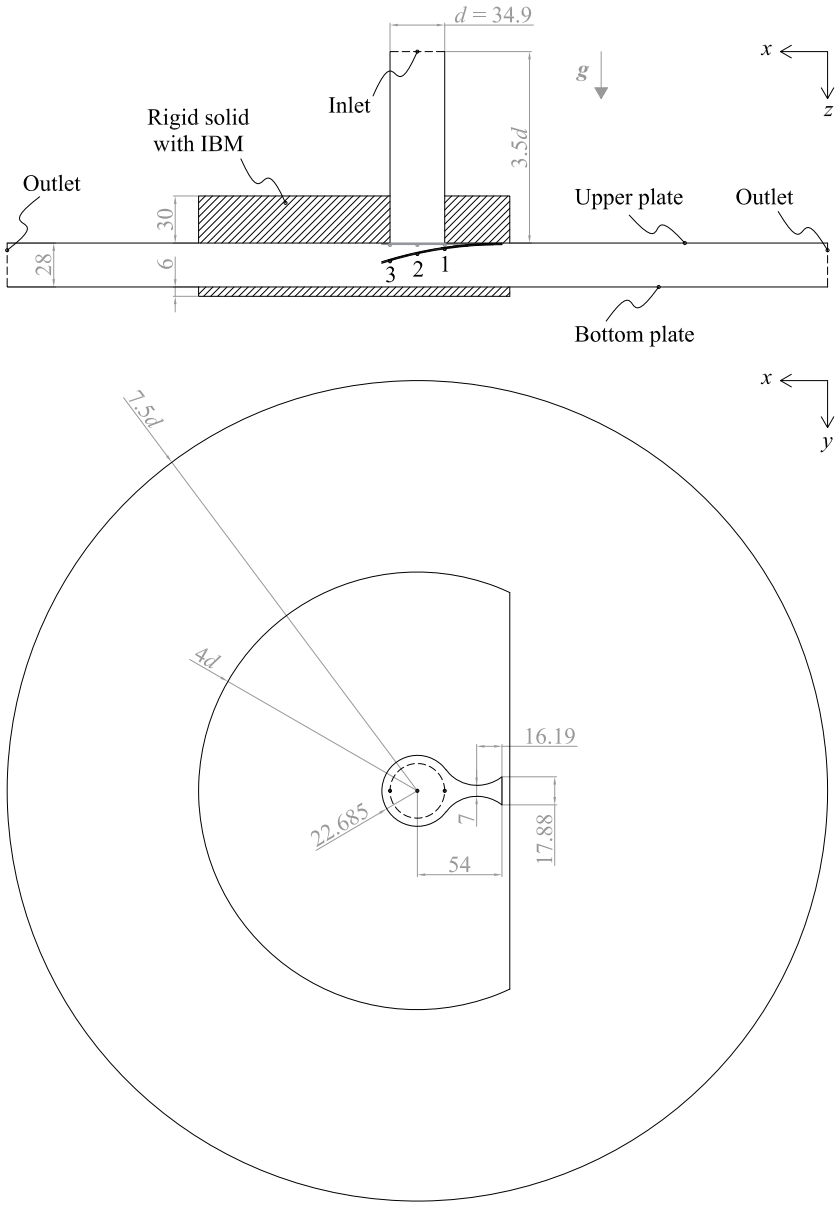

Figure 4.5: Two views of the computational domain with dimensions in mm. Control points 1, 2 and 3 for lift measurements.

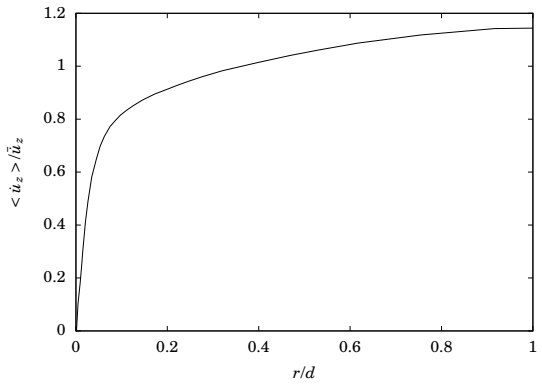

Figure 4.6: Averaged inlet velocity profile used for the simulations. Data extracted from [52] for a $Re = 13,750$.

4.5.3 Numerical parameters

Two unstructured meshes with different refinement level have been tested. Mesh 1 defines a mesh size of 1.5 mm on both surfaces of the plate, 1 mm on the plate perimeter and 3 mm on the walls of the feeding pipe. A total of 460,655 tetrahedral control volumes is reached. Mesh 2 halves the mesh sizes of mesh 1, raising the number of tetrahedra to 2,233,351.

Throughout valve opening, a gap will appear between the valve and the seat, making necessary a new set of fluid elements in that zone. In order to avoid a remeshing procedure, there will be moving elements which will perform as solid (upper plate) when valve is closed, and as fluid when it is opened. This change in the elements nature is achieved using an immersed boundary method (IBM) [53] and is shown in figure 4.7. Figure 4.5 includes the dimensions of the required auxiliary regions. As can be seen in both pictures, extra elements have been added as well at the bottom plate. They will help to accommodate the mesh deformation and to preserve mesh quality when the valve opens.

A relative residual tolerance of 10^{-6} is used to check the convergence of the fluid pressure solver, whereas 10^{-5} is used for the FSI coupling iterations which are performed at every time step. Fluid mesh update over time is solved by means of the Laplacian method with a volume stiffening of $\chi = 1$. Finally, the size of the time step is automatically maximised ensuring numerical stability of the explicit fluid model

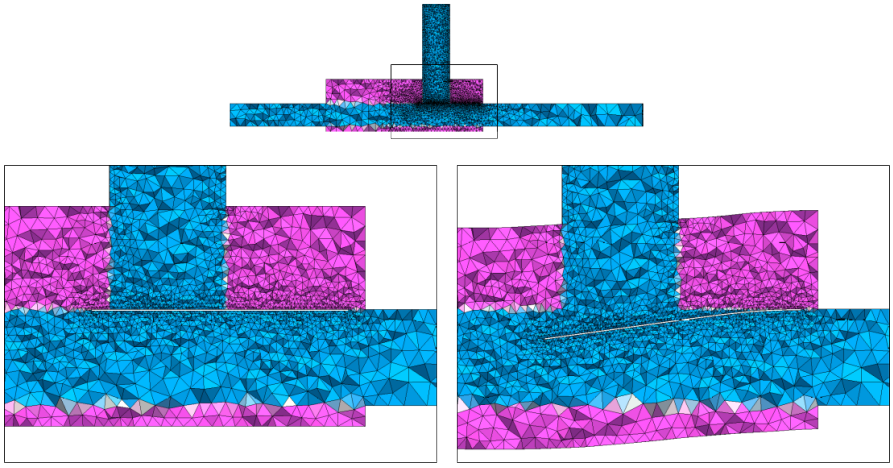

Figure 4.7: Mesh 1 at different instants. On the left when the reed valve is completely closed, and on the right when it is opened. Fluid elements in blue and immersed rigid body elements in pink.

Table 4.1: Natural frequencies of the reed valve.

Mode	1	2	3	4	5	6	7	8
f [Hz]	30.57	129.3	319.7	980.6	1039	1545	2039	2288

Mode	9	10	11	12	13	14	15
f [Hz]	2702	3738	3828	3925	4147	5412	5443

according to the method described in [54].

4.5.4 Results and discussion

First, a modal analysis has been carried out to find the mode shapes ϕ_m and the radial frequencies ω_m of the free vibrating reed with clamped boundary condition in its root. External commercial software has been used for this purpose. Work from [55] mentioned that up to 15 modes were excited when a beam collides with a stiff stop. Since the reed is subjected to impact with a rigid plate with an orifice, the study considers the first 15 normal modes of the structure. The solution of the normal mode analysis is summarised

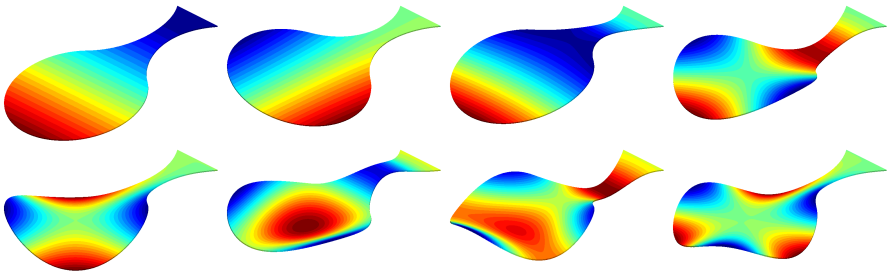

Figure 4.8: Deformation pattern of the first eight free vibration modes of the plate, ordered from left to right and from top to bottom. Colours according to the normal displacement.

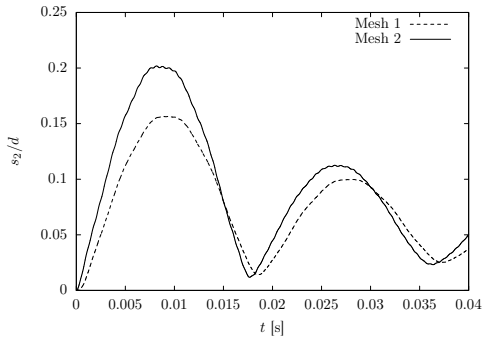

Figure 4.9: Valve lift measured at point 2 for the initial transient obtained with differently refined meshes.

in figure 4.8 and table 4.1. The obtained first natural frequency is very close to the value of 31.4 Hz found by the original authors [51].

Due to the computational cost associated with the most refined mesh 2, the complete transient simulation, until a periodic response of the system, has only been carried out with mesh 1. However, the initial transient obtained with both spatial discretisations has been compared to ensure that the coarser mesh provides a good representative description of the FSI phenomenon. Valve lift, which was described as u_z in section 4.5.1, is here represented directly by the letter s and has been tracked for the three control points highlighted in figure 4.5. Figure 4.9 plots the lift on the second control point during the first 0.04 seconds. Despite differences in amplitude and frequency of

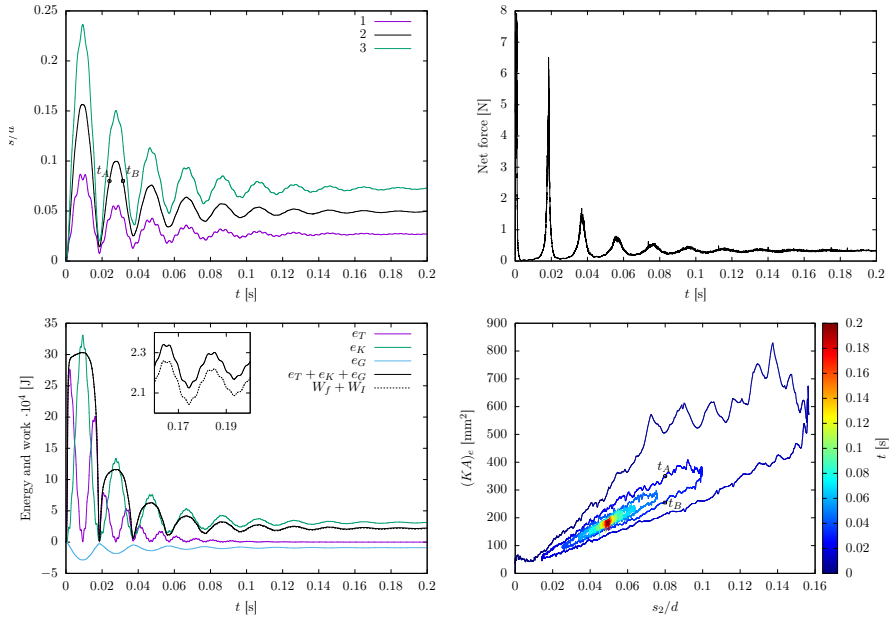

Figure 4.10: Summary of the complete transient simulation of the turbulent flow through a self-actuated valve obtained with mesh 1. Clockwise from top left: valve lift at the control points, fluid net force on the valve, effective flow area as a function of valve lift and time, and energy and external work of the valve.

the solid oscillatory motion, the trends are similar and mesh 1 can be used to conduct a qualitative study of the system.

The solution of the entire transient FSI analysis is summarised in figure 4.10. At the beginning, the gas flow impacts with the closed valve, generating a pressure load that abruptly bends the valve and opens the flow passage (see time evolution of the lift). Although the first mode of vibration predominantly governs the deformation, higher modes are also excited because of the sudden fluid load. The energy balance, observed in the same figure, shows that the work done by the fluid makes the structure kinetic energy increase. As soon as bending increases, fluid force drops and kinetic energy is progressively transformed to strain energy. This continues until reaching the maximum lift, where reed velocity is zero and strain energy is maximum. At this moment, if no more gas would flow, the solid would conserve this gained total energy,

by oscillating endlessly, since no structural damping has been considered within the plate model. Nevertheless, in this case, the steady incompressible flow is working as a viscous damper of the solid vibration.

As the reed starts closing and flow passage narrows, pressure upstream soars to ensure that the entire mass of incoming fluid can be evacuated from the channel and thus satisfy the continuity law. Such a pressure peak together with the fluid cushion placed between valve and seat is capable of stopping the reed before it collides with the seat. In this way, the solid with no speed is in an open position, resulting in a fluid force and work that are lower than those reached at the beginning, when the valve was stopped but completely closed. The total energy absorbed by the fluid diminishes, and so does the lift and the inertia to later approach the base. The oscillation amplitude decays until eventually a practically constant aperture is established after few cycles. The zoom on the energy graph shows that a slight mismatch between the total energy of the reed ($e_T + e_K + e_G$) and the total work done by the fluid (W_f) and the seat impacts (W_I) is accumulating over time. The energy of the structure is probably larger due to the trapezoidal rule employed for the time integration of the plate equations.

Figure 4.10 includes the effective flow area $(KA)_e$ as a function of the valve lift measured at point 2. The effective flow area is a design parameter of reed valves and is calculated for incompressible flows as [30]

$$(KA)_e = \frac{\dot{m}}{\sqrt{2\rho_f(p_u - p_d)}}, \tag{4.35}$$

where pressure p_u is the upstream pressure (taken as the average pressure on the inlet boundary) and p_d is the discharge static pressure (taken as the pressure on the outlet boundaries). Parameter $(KA)_e$ measures the area that an ideal flow would need to evacuate the inlet mass $\dot{m}$ with the existing pressure difference, and can be used to compare the difficulty faced by the fluid to flow through the valve. As can be seen in the graph, the effective area does not depend only on the reed lift but also on its velocity, since a greater value is obtained when it is opening than when it is closing. This means that the pressure drop developed is higher when the valve wall moves against the pipe flow. Such velocity effect becomes perceptible because of the high frequency of the structure, which generates velocities of the same order as those of the fluid.

Two instants that share a common lift of $s_2/d = 0.08$ have been chosen to analyse how the fluid load and flow topology varies according to the mentioned sign of the reed velocity. See points t_A (opening) and t_B (closing) in figure 4.10. Pressure distribution over the upstream face of the valve at both instants is outlined in figure 4.11. The

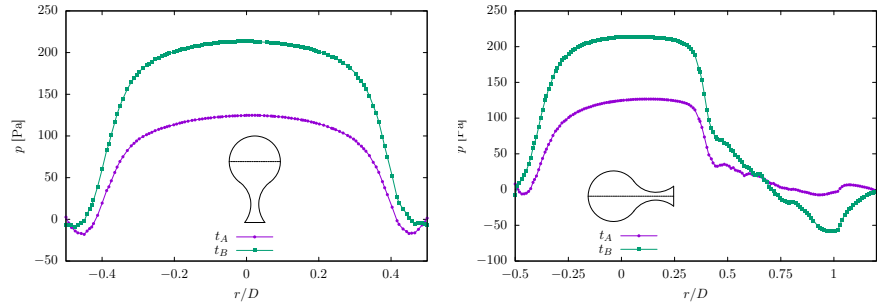

Figure 4.11: Relative pressure over the upstream face of the valve along both radial lines. Results from the simulation with mesh 2.

pressure is effectively higher when closing, due to the greater change of momentum of the colliding fluid particles. Besides, the pressure along the longitudinal axis shows asymmetry with respect to the centre of the pipe as a result of the bent reed profile.

Figure 4.12 shows the magnitude of the velocity at the same instants. At t_A the flow in the diffuser zone (between reed and seat) detaches from the valve and later reattaches to the seat, forming a recirculating bubble near the seat corner. Besides, a large vortex is developed around the valve perimeter. When the valve is closing at t_B, the mass flow through the diffuser rises, but the opening space is the same as in t_A. Therefore, velocity increases distorting the recirculating flow in the diffuser and the surrounding large-scale vortex.

With the finest mesh, the maximum lift at control point 1 is 3.89 mm, and the frequency of the first opening cycles is 56.3 Hz (see figure 4.9). These values are close to those measured in the experimental tests for the same Reynolds number, 3.07±0.02 mm and 57.9 Hz, respectively. Unfortunately, the predicted damped oscillation was not evidenced in the experimental tests [51]. Data from laboratory reflected a periodic fluttering motion of the valve with an impact against the seat in each opening cycle. The structure was less affected by fluid loads, as can also be seen in their higher oscillation frequency. A completely undamped vibration would define a frequency which doubles the first natural frequency, i.e. 61.14 Hz, due to the impact with the seat. Thus, the numerical model is predicting a stiffer flow that makes the valve response more compliant to the fluid. This leads one to think that the discrepancies might come from the fluid modelling, particularly from the incompressibility assumption.

The high velocities of the solid and the large pressure variations may be provoking

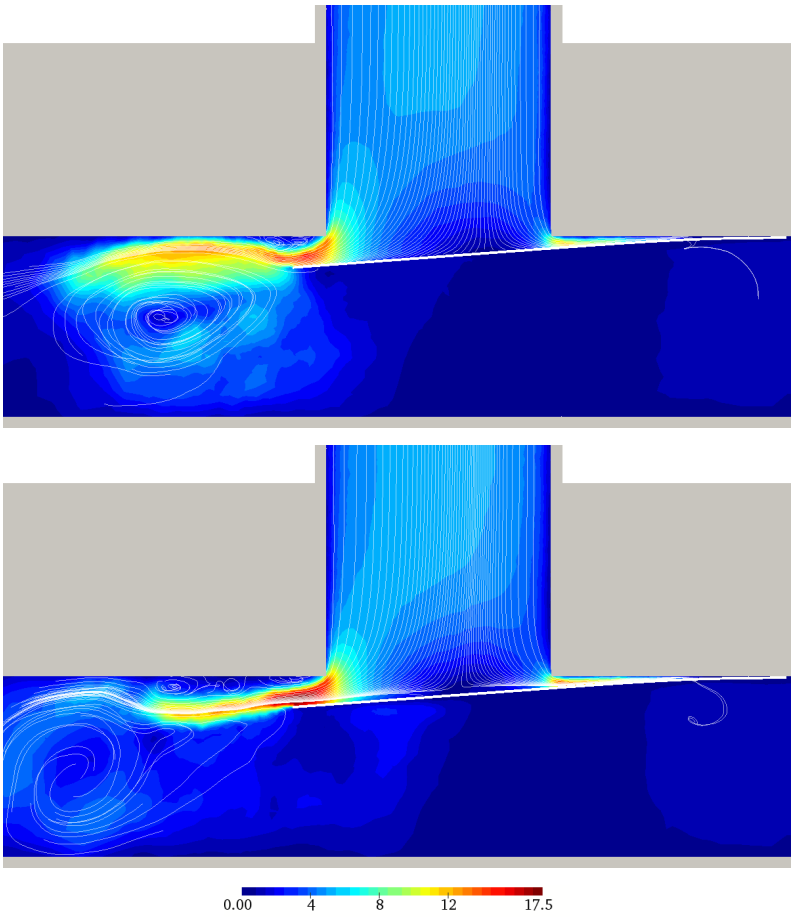

Figure 4.12: Velocity magnitude map (in m/s) and streamlines at t_A (top) and t_B (bottom). Results from the simulation with mesh 2.

changes in the air density. This variable density would alleviate the forces exerted on the reed and would allow the reed to collide with the seat with a certain speed. Models based on the incompressible flow through static disk-type and reed-type valves have been used for preliminary design and understanding the device physics [56–59]. However, it seems that a complete dynamic operation of this coupled problem needs to be modelled by compressible formulations. In fact, most of the previous FSI simulations of flow through reed valves were employing compressible fluid models [40, 42–44].

Systems involving valves of this type and incompressible flows, such as in compact electrohydraulic pumps [36, 60], would be a more suitable field to apply the presented methodology, according to the results from the current simulation.

4.6 Conclusions

A new FSI partitioned method for incompressible flows is presented and tested in this chapter. It works as a partitioned platform with a Lagrangian approach for the solid and an arbitrary Lagrangian-Eulerian approach for the fluid. Thus, the position of the solid interface moves and defines a new conformed computational domain of the fluid. The internal vertices of the fluid mesh adapt to the boundary displacement without altering the element topology by following one of the implemented moving-mesh techniques: the pseudo-solid and the Laplacian. Both include a volume-based element stiffness which makes the larger cells absorb the major deformation, and helps to preserve the quality of the mesh in physically meaningful zones. While the pseudo-solid and Laplacian methods performed satisfactorily when the boundary was exclusively translated, it was the former the only one to provide a valid redistribution of the inner vertices when boundary rotation was involved.

The tool is designed to solve cases with a strong coupling between fluid and structure physics thanks to a semi-implicit algorithm. A fractional-step method is used to split the pressure stress term of the fluid and implicitly couple it to the structure. The remaining fluid terms and the mesh motion are only explicitly coupled. The final method is modular, efficient and robust under weakly or strongly coupled FSI.

The airflow through a reed valve is analysed using the partitioned platform. The case is of industrial interest due to its role in the efficiency and reliability of hermetic reciprocating compressors. The plate-type valve allows solving the structural part with a simplified model based on the Kirchhoff-Love plate theory and the normal mode summation method. A penalty force is considered to simulate the impact between the elastic valve and the rigid seat. Such solid modelling help to easily test the implemented FSI

tools and generates trust to couple the finite volume structural procedures of previous chapters to the finite volume analysis of incompressible flows. The numerical solution agrees with the physical phenomenology of the case and predicts values of maximum amplitude and frequency of the structural vibration that are close to those captured in the experiment. However, the flow prevents the valve from closing completely, unlike seen in the experiment, and the oscillation is damped until finally reaching a steady open position which balances fluid load and elastic stresses of the solid. The first hypothesis for the discrepancy points to the need for a compressible flow formulation to alleviate the fluid pressure peaks and therefore replicate the periodic fluttering observed in the laboratory.

References

[1] Y. Bazilevs, K. Takizawa, and T. E. Tezduyar. *Computational Fluid-Structure Interaction: Methods and Applications*. Wiley Series in Computational Mechanics. Wiley, 2013.

[2] G. Hou, J. Wang, and A. Layton. Numerical methods for fluid-structure interaction — A review. *Communications in Computational Physics*, 12(2):337–377, 2012.

[3] T. E. Tezduyar, K. Takizawa, and Y. Bazilevs. *Fluid–Structure Interaction and Flows with Moving Boundaries and Interfaces*, pages 1–53. American Cancer Society, 2017.

[4] Y. Kim and C. S. Peskin. Penalty immersed boundary method for an elastic boundary with mass. *Physics of Fluids*, 19(5):053103, 2007.

[5] J. Yang, S. Preidikman, and E. Balaras. A strongly coupled, embedded-boundary method for fluid–structure interactions of elastically mounted rigid bodies. *Journal of Fluids and Structures*, 24(2):167 – 182, 2008.

[6] C. J. Greenshields, H. G. Weller, and A. Ivanković. The finite volume method for coupled fluid flow and stress analysis. *Computer Modeling and Simulation in Engineering*, 4(3):213–218, 1999.

[7] A. Borghi, N. B. Wood, R. H. Mohiaddin, and X. Y. Xu. Fluid–solid interaction simulation of flow and stress pattern in thoracoabdominal aneurysms: A patient-specific study. *Journal of Fluids and Structures*, 24(2):270 – 280, 2008.

[8] T. E. Tezduyar and S. Sathe. Modelling of fluid–structure interactions with the space–time finite elements: Solution techniques. *International Journal for Numerical Methods in Fluids*, 54(68):855–900, 2007.

[9] B. Hübner, E. Walhorn, and D. Dinkler. A monolithic approach to fluid–structure interaction using space–time finite elements. *Computer Methods in Applied Mechanics and Engineering*, 193(23):2087 – 2104, 2004.

[10] P. B. Ryzhakov, R. Rossi, S. R. Idelsohn, and E. Oñate. A monolithic lagrangian approach for fluid–structure interaction problems. *Computational Mechanics*, 46(6):883–899, 2010.

[11] P. Causin, J. F. Gerbeau, and F. Nobile. Added-mass effect in the design of partitioned algorithms for fluid–structure problems. *Computer Methods in Applied Mechanics and Engineering*, 194(42):4506 – 4527, 2005.

[12] J. Degroote. Partitioned simulation of fluid-structure interaction. *Archives of Computational Methods in Engineering*, 20(3):185–238, Sep 2013.

[13] M. Lesoinne and C. Farhat. Higher-order subiteration-free staggered algorithm for nonlinear transient aeroelastic problems. *AIAA journal*, 36(9):1754–1757, 1998.

[14] U. Küttler and W. A. Wall. Fixed-point fluid–structure interaction solvers with dynamic relaxation. *Computational Mechanics*, 43(1):61–72, 2008.

[15] M. Á. Fernández and M. Moubachir. A Newton method using exact jacobians for solving fluid–structure coupling. *Computers & Structures*, 83(2):127 – 142, 2005.

[16] Termo Fluids S.L. http://www.termofluids.com/.

[17] R. W. C. P. Verstappen and A. E. P. Veldman. Symmetry-preserving discretization of turbulent flow. *Journal of Computational Physics*, 187:343–368, 2003.

[18] L. Jofre, O. Lehmkuhl, J. Ventosa, F. X. Trias, and A. Oliva. Conservation properties of unstructured finite-volume mesh schemes for the Navier-Stokes equations. *Numerical Heat Transfer, Part B: Fundamentals*, 65(1):53–79, 2014.

[19] A. J. Chorin. Numerical solution of the Navier-Stokes equations. *Mathematics of computation*, 22(104):745–762, 1968.

[20] P. Sagaut and M. Germano. *Large Eddy Simulation for Incompressible Flows*. Springer-Berlag, 2001.

[21] F. Nicoud and F. Ducros. Subgrid-scale stress modelling based on the square of the velocity gradient tensor. *Flow, Turbulence and Combustion*, 62(3):183–200, 1999.

[22] F. X. Trias, O. Lehmkuhl, A. Oliva, C. D. Pérez-Segarra, and R. W. C. P. Verstappen. Symmetry-preserving discretization of Navier–Stokes equations on collocated unstructured grids. *Journal of Computational Physics*, 258:246 – 267, 2014.

[23] K. Stein and T. Tezduyar. Advanced mesh update techniques for problems involving large displacements. In *Fifth World Congress on Computational Mechanics (WCCM V)*, Vienna, 2002.

[24] R. Smith and J. Wright. A classical elasticity-based mesh update method for moving and deforming meshes. In *48th AIAA Aerospace Sciences Meeting Including the New Horizons Forum and Aerospace Exposition*, page 164, Orlando, 2010.

[25] H. Jasak and Ž. Tuković. Automatic mesh motion for the unstructured finite volume method. *Transactions of FAMENA*, 30(2):1–20, 2006.

[26] I. Demirdžić and M. Perić. Space conservation law in finite volume calculations of fluid flow. *International Journal for Numerical Methods in Fluids*, 8(9):1037–1050, 1988.

[27] M. Lesoinne and C. Farhat. Geometric conservation laws for flow problems with moving boundaries and deformable meshes, and their impact on aeroelastic computations. *Computer Methods in Applied Mechanics and Engineering*, 134(1):71 – 90, 1996.

[28] M. Á. Fernández, J.-F. Gerbeau, and C. Grandmont. A projection semi-implicit scheme for the coupling of an elastic structure with an incompressible fluid. *International Journal for Numerical Methods in Engineering*, 69(4):794–821, 2007.

[29] W. Soedel. *Design and Mechanics of Compressor Valves*. Purdue University, 1984.

[30] W. Soedel. *Mechanics, Simulation and Design of Compressor Valves, Gas Passages and Pulsation Mufflers*. Purdue University, 1992.

[31] F. A. Ribas, C. J. Deschamps, F. Fagotti, A. Morriesen, and T. Dutra. Thermal analysis of reciprocating compressors - A critical review. In *International Compressor Engineering Conference*, Indiana, 2008.

[32] S. M. Leonard. Increase reliability of reciprocating hydrogen compressors. *Hydrocarbon Processing*, 75(1):67 – 74, 1996.

[33] S. Woo, D. L. O'Neal, and M. Pecht. Reliability design of a reciprocating compressor suction reed valve in a common refrigerator subjected to repetitive pressure loads. *Engineering Failure Analysis*, 17(4):979 – 991, 2010.

[34] G. Cunningham, R. J. Kee, and R. G. Kenny. Reed valve modelling in a computational fluid dynamics simulation of the two-stroke engine. *Proceedings of the Institution of Mechanical Engineers, Part D: Journal of Automobile Engineering*, 213(1):37–45, 1999.

[35] A. Angeletti, M. E. Biancolini, E. Costa, and M. Urbinati. Optimisation of reed valves dynamics by means of fluid structure interaction modelling. In *4th European Automotive Simulation Conference*, Munich, 2009.

[36] A. Chaudhuri, J.-H. Yoo, and N. M. Wereley. Design, test and model of a hybrid magnetostrictive hydraulic actuator. *Smart Materials and Structures*, 18(8):085019, 2009.

[37] A. L. Knutson and J. D. Van de Ven. Modeling and experimental validation of a reed check valve for hydraulic applications. In *BATH/ASME 2016 Symposium on Fluid Power and Motion Control*, 2016.

[38] D. Kamensky, M.-C. Hsu, D. Schillinger, J. Evans, A. Aggarwal, Y. Bazilevs, M. S. Sacks, and T. J. R. Hughes. An immersogeometric variational framework for fluid–structure interaction: application to bioprosthetic heart valves. *Computer methods in applied mechanics and engineering*, 284:1005–1053, 2015.

[39] L. Böswirth. A new valve dynamics simulation program and its use for the design of valves. In *International Compressor Engineering Conference*, Indiana, 1996.

[40] M. Schildhauer and A. Spille-Kohoff. Numerical simulation of fluid-structure interaction: Turek benchmark and kinetics of a reed valve. *Progress in Computational Fluid Dynamics, an International Journal*, 14(1):38–48, 2014.

[41] J. Mayer, P. Bjerre, and F. Brune. A comparative study of different numerical models for flapper valve motion. In *International Compressor Engineering Conference*, Indiana, 2014.

[42] N. C. Lemke, M. König, J. Hennig, S. Försterling, and J. Köhler. Transient experimental and 3D-FSI investigation of flapper valve dynamics for refrigerant compressors. In *International Compressor Engineering Conference*, Indiana, 2016.

[43] A. Parihar, D. Myszka, B. Robinet, and T. Hodapp. Integrating numerical models for efficient simulation of compressor valves. In *International Compressor Engineering Conference*, Indiana, 2016.

[44] J. L. Gasche, A. D. S. de Lima Dias, D. D. Bueno, and J. F. Lacerda. Numerical simulation of a suction valve: Comparison between a 3D complete model and a 1D model. In *International Compressor Engineering Conference*, Indiana, 2016.

[45] W. Thomson. *Theory of Vibration with Applications (5th Edition)*. Taylor & Francis, 1998.

[46] K.-J. Bathe. *Finite Element Procedures*. Prentice Hall, 1996.

[47] J. O. Hallquist, G. L. Goudreau, and D. J. Benson. Sliding interfaces with contact-impact in large-scale lagrangian computations. *Computer Methods in Applied Mechanics and Engineering*, 51(1):107 – 137, 1985.

[48] P. Cardiff, A. Karač, and A. Ivanković. Development of a finite volume contact solver based on the penalty method. *Computational Materials Science*, 64:283 – 284, 2012.

[49] L. Paoli and M. Schatzman. Ill-posedness in vibro-impact and its numerical consequences. In *European Congress on Computational Methods in Applied Sciences and Engineering (ECCOMAS)*, Barcelona, 2000.

[50] H. Z. Jahromi and B. A. Izzuddin. Energy conserving algorithms for dynamic contact analysis using Newmark methods. *Computers & Structures*, 118:74 – 89, 2013.

[51] J. L. Gasche, D. M. Arantes, and T. Andreotti. Experimental analysis of the fluid structure interaction in a suction valve model. In *International Compressor Engineering Conference*, Indiana, 2014.

[52] J. Kim, P. Moin, and R. Moser. Turbulence statistics in fully developed channel flow at low reynolds number. *Journal of fluid mechanics*, 177:133 – 166, 1987.

[53] F. Favre, O. Antepara, O. Lehmkuhl, R. Borrell, and A. Oliva. On the fast transient spoiler deployment in a NACA0012 profile using LES techniques combined with AMR and IMB methods. In *6th European Conference on Computational Fluid Dynamics (ECFD VI)*, Barcelona, 2014.

[54] F. X. Trias and O. Lehmkuhl. A self-adaptive strategy for the time integration of Navier-Stokes equations. *Numerical Heat Transfer, Part B: Fundamentals*, 60(2):116–134, 2011.

[55] C. C. Lo. A cantilever beam chattering against a stop. *Journal of Sound and Vibration*, 69(2):245 – 255, 1980.

[56] C. J. Deschamps, A. T. Prata, and R. T. S. Ferreira. Modeling of turbulent flow through radial diffuser. *Journal of the Brazilian Society of Mechanical Sciences*, 22:31 – 41, 2000.

[57] J. Rigola, O. Lehmkuhl, J. Ventosa, C. D. Pérez-Segarra, and A. Oliva. Numerical simulation of the turbulent fluid flow through valves based on Low Mach models. In *International Compressor Engineering Conference*, Indiana, 2012.

[58] J. Rigola, D. Aljure, O. Lehmkuhl, C. D. Pérez-Segarra, and A. Oliva. Numerical analysis of the turbulent fluid flow through valves. Geometrical aspects influence at different positions. *IOP Conference Series: Materials Science and Engineering*, 90(1):012026, 2015.

[59] F. Barbi, J. L. Gasche, A. da Silveira Neto, M. M. Villar, and R. S. de Lima. Numerical simulation of the flow through a compressor-valve model using an immersed-boundary method. *Engineering Applications of Computational Fluid Mechanics*, 10(1):255–271, 2016.

[60] A. Chaudhuri. Static and dynamic deformations of a reed valve immersed in hydraulic fluid. In *Proceedings of the 2014 COMSOL Conference*, Boston, 2014.

5

Thermo-mechanical analysis of thermocline energy storage tanks

5.1 Introduction

Concentrated solar power (CSP) plants have become one of the most reliable promises for a sustainable energy future. They are able to transform the solar radiation into electricity by means of a collector system and a thermodynamic power cycle. The collector involves a set of reflectors that focuses the sunlight on a point (power tower, parabolic dish), or along a line (parabolic trough, Fresnel). A heat transfer fluid (HTF) is pumped to the reflectors focal region so that it absorbs the thermal energy. In many applications, this hot fluid works as the hot source within the power cycle by evaporating water. Eventually, the resulting steam moves a turbine and the electrical generator.

As a result of the day/night cycle and the weather, a thermal energy storage (TES) is essential, which is able to match supply and demand of energy in order to be commercially viable. This system collects the surplus thermal energy and provides it when there is not enough solar radiation to cover all the demand. The current standard storage for CSP is the two-tank molten salt TES in which there is a separate tank for the hot and cold fluid. Since its associated investment and operational costs are relatively high, different cheaper approaches have been considered.

In this sense, containing both fluids in a single thermocline storage tank is becoming a promising alternative as can be observed in the literature [1–3]. The conventional design is a dual-media vessel containing the HTF and an inert granulate material,

preferably quartzite rock and silica sand [4], which works as a porous medium. It is based on the principle of buoyancy stratification to separate hot and cold fluid; the former with a lower density at the top, and the latter at the bottom. Thus, a charging process (i.e. heating) is carried out by introducing the HTF from the upper tank section and a discharging process (i.e. cooling) from the base. The main benefit of the filler material is the reduction of higher-cost fluid required, since the solid is acting as the major sensible heat storage medium. This, together with the use of one tank instead of two, is translated in costs savings of approximately 33 % compared with the two-tank molten salt approach [5, 6].

Despite its proven potential, there is still a critical concern that has stopped it from being implemented in commercial plants. It refers to thermal ratcheting, a phenomenon that might compromise the structural integrity of the system [5, 7, 8]. It may occur when a tank filled with particulate solids is cyclically heated and cooled. As long as the wall has a greater thermal expansion than the filler material, a radial gap is generated between both during heating, allowing the cohesionless particles to settle lower to fill it. When temperature drops, the tank is unable to contract completely, resulting in thermal stresses that may cause plastic deformation. If the strain hardening cannot prevent the same process in the next heating and cooling cycles, the tank wall will be slowly ratcheted outward until it fails.

Some technological solutions have already been suggested in order to elude the thermal ratcheting matter. A composite wall for the vessel has been proposed by [8]. It settles an insulation layer between the inside and the metal shell, to minimise the wall temperature variation and consequently, the potential of ratcheting. A buried concrete tank with a truncated cone shape for guiding the rocks upwards during thermal expansion and, therefore, reducing lateral pressure on the walls, has been tested and modelled [9]. Air worked as HTF, and no liquid option was contemplated. Another concept removes all the solid filler material, obtaining a single-media thermocline tank with fluid only [10]. Even though convective mixing flows are significant without the porous media, the thermal diffusivity lessens, so that it can achieve a slightly better thermal function. A structured packed thermocline tank can also be considered as a viable proposal [11–13]. Different arrangements of structured material can be chosen to replace the packed aggregated bed and thus avoid solid filler settlement. The principal disadvantage of all these alternatives compared with the original thermocline rests on economics.

Although there has been extensive research regarding heat transfer and storage performance of thermocline tanks [6, 14–17], few works have carried out a mechanical

analysis that addresses the ratcheting issue. The design of the experimental thermocline system of Solar One Pilot Plant [18, 19] imposed a high yield strength material for the tank wall in order to avoid any plastic deformation. It was developed considering the active load of the inner gravel and its differential expansion with the shell. Only a particular stress state was evaluated: the cooldown from maximum temperature to ambient temperature with an assumed rigid filler. During the 5-year performance of these facilities, no evidence of thermal ratcheting was appreciated and some measures of tank wall hoop stress were taken [7]. Unfortunately, they showed great uncertainty and no conclusion was drawn.

The subsequent investigations have been limited to numerical modelling. The mentioned Solar One case has been reproduced using a static stress-strain finite element analysis with two states of maximum and minimum operating temperatures [8, 20]. The solid was simplified to be a cohesionless rigid medium without weight or thermal expansion. Filler solid and shell have been analysed more precisely considering elastoplastic numerical models in [21]. Preliminary results showed that bed physical properties are a crucial aspect to overcome ratchet failure. For this reason, experimental measures of these bed properties have been reported [22].

This chapter presents an original validated numerical model that can evaluate the energy and mechanical response of these storage tanks during a CSP plant normal operation. Compared with previous studies, this includes the thermal interaction between the principal components of the subsystem: particulate solid, fluid, shell, insulation, ullage, ground and environment. In this manner, the simulated plant and storage face real operating and weather conditions while performing an exhaustive thermal loss calculation. The structural analysis is improved utilising a generalised thermoelastic model for the walls and a complete model for the filler material, which considers temperature expansion and a bulk-solid mechanical behaviour.

The whole platform is employed to simulate different thermocline configurations within two different CSP plants that are currently working with a two-tank molten salt storage subsystem, Andasol and Gemasolar. First, tanks are properly sized for each scenario, and then a parametric study is carried out in order to test the storage performance and the risk of ratchet failure throughout normal operating conditions. The combination of such a complete advanced model with this kind of analysis has still not been presented in the literature. Consequently, a better awareness of the viability of packed-bed thermocline storage for solar plants is provided.

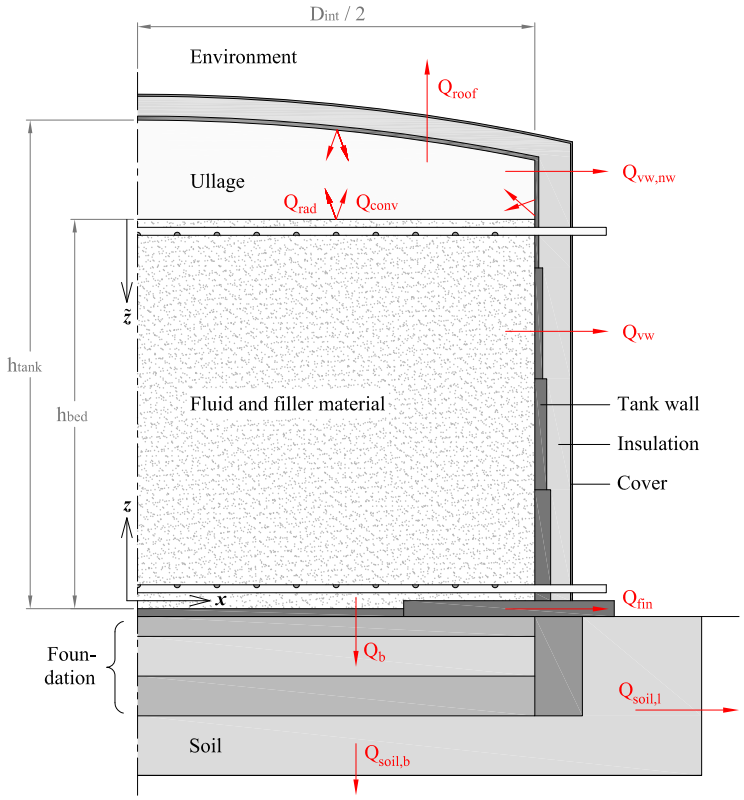

Figure 5.1: Elements of the thermocline storage tank and their boundary conditions.

5.2 Mathematical and numerical model

All components whose physics are solved and coupled in the present dual-media thermocline model are outlined in figure 5.1. The subsystem is a tank filled with fluid and bulk solid material. The walls are made up of metal rings with varying thickness. In order to minimise thermal losses, roof and sides are covered with an insulation blanket with a metal weather cover. There is an ullage space available above the fluid and bed to accommodate substance thermal expansion and to keep a non-hazardous inert gas. The ground consists of different layers of foundation and soil. When charging, hot fluid at T_{hot} is introduced through a manifold into the top of the tank and is drawn from a lower manifold, warming up the filler material. During the discharge process, cold fluid

at T_{cold} is pumped upwards, recovering through its way up the heat from the porous bed.

The coupling of all these elements considering the transient thermal and mechanical loads has been implemented within the existing NEST platform [23, 24]. It is a parallel computing code based on a modular object-oriented methodology. The individual models of each part are coupled explicitly, i.e. they use the boundary conditions defined by the linked elements in the previous time step. This loose coupling can be used due to the quasi-static processes that occur in this application. This together with the small deformations that are involved, avoids using all the FSI tools presented in chapter 4. The purpose of those is to tackle future strongly coupled problems which require an update of domain and mesh of the fluid.

The mathematical representation of the environment, ground, ullage and insulation are described in [24, 25]. The packed-bed and shell physics, as well as the subsystem management, are described hereinafter.

5.2.1 Storage management

The storage tank functioning relies on three variables: radiation availability, plant electric demand and stop-restart criteria for both charge and discharge processes. To take into account the whole power plant, a simplified replicable model is proposed. It consists of three main subsystems: a solar field (SF), a TES and a power block (PB), as it is sketched in figure 5.2. It is supposed to have constant firm capacity $\dot{W}_{EG}$. Thus, the thermal energy required for the hot source of the thermodynamic cycle is also constant,

$$\dot{Q}_{\mathrm{PB}} = \frac{\dot{W}_{\mathrm{EG}}}{\eta_{\mathrm{PB}}}, \tag{5.1}$$

where the thermal efficiency of the PB is given by η_{PB}. In the solar field the heat absorbed by the fluid from the sun is proportional to the direct normal irradiance DNI, the collector area S_{SF} and the solar field collecting efficiency η_{SF}:

$$\dot{Q}_{\mathrm{SF}} = \mathrm{DNI} \cdot S_{\mathrm{SF}} \cdot \eta_{\mathrm{SF}}. \tag{5.2}$$

Having defined the thermal energy the HTF should exchange in both subsystems,

the mass flows are to be found with the following enthalpic balances:

$$\dot{Q}_{\mathrm{SF}} = \dot{m}_{\mathrm{SF}}\,\bar{c}_{p,f}\left(T^{out}_{\mathrm{SF}} - T^{in}_{\mathrm{SF}}\right), \tag{5.3}$$

$$\dot{Q}_{\mathrm{PB}} = \dot{m}_{\mathrm{PB}}\,\bar{c}_{p,f}\left(T^{in}_{f\mathrm{PB}} - T^{out}_{\mathrm{PB}}\right). \tag{5.4}$$

At this point, if $\dot{m}_{\mathrm{SF}}$ is larger than $\dot{m}_{\mathrm{PB}}$, the storage will charge with a mass flow of $\dot{m}_C = \dot{m}_{\mathrm{SF}} - \dot{m}_{\mathrm{PB}}$. Otherwise, discharge will be set with $\dot{m}_D = \dot{m}_{\mathrm{PB}} - \dot{m}_{\mathrm{SF}}$. The resulting mixture between outflows from the subsystem SF or PB and the storage gives rise to the updated inlet temperatures (see figure 5.2),

$$T^{in}_{\mathrm{SF}} = \frac{\dot{m}_{\mathrm{PB}} T^{out}_{\mathrm{PB}} + \dot{m}_C T^{out}_C}{\dot{m}_{\mathrm{SF}}}, \tag{5.5}$$

$$T^{in}_{\mathrm{PB}} = \frac{\dot{m}_{\mathrm{SF}} T^{out}_{\mathrm{SF}} + \dot{m}_D T^{out}_D}{\dot{m}_{\mathrm{PB}}}, \tag{5.6}$$

where T^{out}_{SF} and T^{out}_{PB} are kept invariable controlling the mass flows and equal to T_{hot} and T_{cold}, respectively. The inlet temperatures for the solar field and the power block are used to decide whether the TES process (charge or discharge) can continue or should be stopped. Since there is a thermal gradient inside the tank, the output temperature is expected to be higher than T_{cold} at the end of charge and less than T_{hot} at the end of discharge. In this work, both receiver and generation subsystems are supposed to accept inlet temperatures that deviate ΔT_{CO} from their design magnitude. Bearing this in mind, the cut-off temperature for charging will be $T_{cold} + \Delta T_{CO}$, while it will be $T_{hot} - \Delta T_{CO}$ for discharging.

Furthermore, to avoid several charges and discharges being started and stopped in small time intervals, further thresholds have been defined for restarting the processes. In this sense, and considering a temperature restart tolerance of ΔT_R which is smaller than ΔT_{CO}, discharge does not start if the temperature at the top of the tank is lower than $T_{hot} - \Delta T_R$, while the charge if the temperature at the bottom is higher than $T_{cold} + \Delta T_R$.

5.2.2 Tank inner substances

The model presented in [17] is used. Mass, momentum and energy conservation equations have to be solved in order to be able to simulate the thermal behaviour of the packed bed. These equations are discretised using the finite volume method and assum-

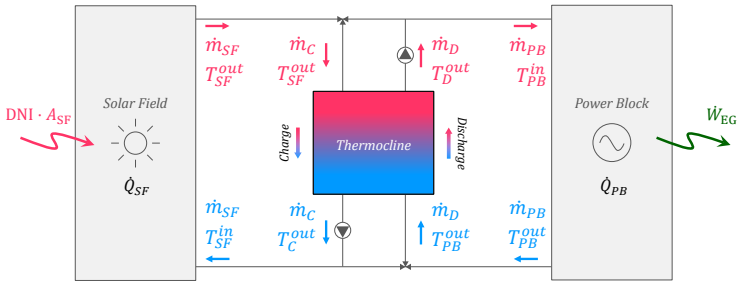

Figure 5.2: Plant diagram with a direct storage system scheme.

ing one-dimensionality in the fluid flow (axial direction of the cylindrical column) and in the heat transfer inside particles (radial direction of spherically shaped pebbles). Thus, only a single representative particle needs to be simulated in each tank section. The tank is divided into N_z cylindrical sections of height Δz_i, and the filler particle into N_r spherical volumes.

For the HTF going through the porous bed, the semi-discrete energy conservation equation in the ith tank section ($i = 1 \dots N_z$) results in:

$$\begin{aligned}\rho_f \epsilon_i V_i c_{p,f} \frac{\partial T_{i,f}}{\partial t} =& S_t \left(k_{eff} \frac{\partial T_f}{\partial z} \right) \Bigg|_{i-1/2}^{i+1/2} \\ &- \dot{m} c_{p,f} \left(T_{i+1/2,f} - T_{i-1/2,f} \right) \\ &- n_{s,i} \frac{T_{i,f} - T_{i.0}}{R_{conv,i}} \\ &- U_{TC-Sh} S_{w,i} \left(T_{i,f} - T_{i,Sh} \right), \end{aligned} \tag{5.7}$$

where r is the particle radial direction, $n_{s,i}$ is the number of filler particles, $T_{i,0}$ is the temperature on the surface of the particles, and ϵ_i is the volume liquid fraction (porosity) that results from the ith bed composition. In the advective term (second on the right-hand side) the fluid is assumed to be coming from section $i-1$ and going to section $i+1$. The calculation of the thermal resistance R_{conv} due to convection between the HTF and the filler material requires the fluid-to-bed Nusselt number, which is calculated using the correlation obtained from [26]. Consequently, the effective thermal conductivity, k_{eff}, takes into account the effects of molecular diffusion and thermal dispersion. The heat transfer convection coefficient between fluid and shell is denoted ad U_{TC-Sh}.

The energy balance for the inner nodes ($j = 1 \ldots N_r$ from outside to inside) of the filler material remains:

$$\rho_s V_{i,j} c_{p,s} \frac{\partial T_{i,j}}{\partial t} = \left(k_s S \frac{\partial T}{\partial r} \right)_{i,j-1/2} - \left(k_s S \frac{\partial T}{\partial r} \right)_{i,j+1/2}, \tag{5.8}$$

where the enthalpy is evaluated by means of the specific heat capacity $c_{p,s}$. For the boundary node ($j = 0$), which is in contact with the fluid, the equation, neglecting thermal conduction between different particles, becomes

$$\rho_s V_{i,0} c_{p,s} \frac{\partial T_{i,0}}{\partial t} = \frac{T_{f,i} - T_{i,0}}{R_{conv,i}} - \left(k_s S \frac{\partial T}{\partial r} \right)_{i,1/2}. \tag{5.9}$$

Regarding the discretisation, the diffusive terms in equations 5.7-5.9 have been approximated by a second-order central difference spatial scheme and a fully implicit temporal integration. The convective term is time-integrated using a fully explicit upwind scheme.

For further details of the model and the discretisation employed see [17].

5.2.3 Tank wall

Once the packed-bed has been solved for a given instant by following the description of the previous section, the temperature field on the shell is calculated. The stress-strain state of the tank wall can then be found taking into account the thermal load and the pressure of the inner substances.

A linear thermoelastic solid model is applied for the tank walls. The linear model is used owing to the small strains the shell is subjected to. It is elastic because it is enough to establish if yield point has been reached, i.e. if solid undergoes non-reversible plastic behaviour. Such solid is governed by the conservation laws for energy and momentum, whose Lagrangian form integrated over a control volume are equations 2.35 and 2.36. The energy source term depending on the strain rate (see equation 2.27) is negligible due to the slow change in the boundary conditions. The gravitational acceleration has replaced the body force $\boldsymbol{b}$ in the vertical direction in order to add the structure's own weight. The linear constitutive equation that specifies the relation between stress $\boldsymbol{\sigma}$, strain $\boldsymbol{\varepsilon}$ and temperature is:

$$\boldsymbol{\sigma} = 2\mu\boldsymbol{\varepsilon} + \lambda \mathrm{tr}(\boldsymbol{\varepsilon})\boldsymbol{I} - 3K\alpha(T - T_0)\boldsymbol{I}, \tag{5.10}$$

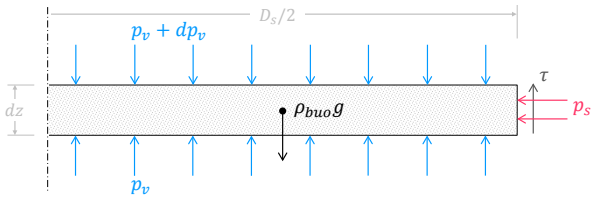

Figure 5.3: Force diagram of a cylindrical slice from the bulk solid.

where T_0 is the reference temperature with no thermal strain (in this case the ambient temperature), α is the thermal expansion coefficient, and μ and λ are the Lamé's coefficients, dependent only on Young's modulus of elasticity E and Poisson's ratio ν.

The infinitesimal strain is related at the same time with the displacements $\boldsymbol{u}$ through

$$\boldsymbol{\varepsilon} = \frac{1}{2}\left[\nabla \boldsymbol{u} + (\nabla \boldsymbol{u})^T\right]. \tag{5.11}$$

Taking (r, θ, z) as the tank cylindrical coordinates, the components $\varepsilon_{r\theta}$ and $\varepsilon_{\theta z}$ are zero, as well as $\sigma_{r\theta}$ and $\sigma_{\theta z}$, due to axisymmetric boundary conditions.

The equations are discretised and solved using the finite volume method described in chapter 2. A three-dimensional computational domain with axisymmetric boundary conditions has been used.

Mechanical boundary conditions Concerning the stress-strain calculation, the vessel geometry is simplified to a cylinder. There is a Dirichlet zero boundary condition in the vertical displacement at the bottom surface and a traction boundary condition at the other surfaces. This traction is nonzero only on the top surface and on the inner sidewall. The load on the top of the cylinder is the weight of the roof. On the inner wall surface, there is the fluid pressure, p_f, and bed pressure, p_s,

$$p(\tilde{z}) = p_f(\tilde{z}) + p_s(\tilde{z}), \tag{5.12}$$

where $\tilde{z}$ is the depth of the fluid column.

The fluid pressure is mainly the sum of the ullage pressure plus the hydrostatic fluid pressure, since slow flow velocity makes its pressure loss negligible,

$$p_f(\tilde{z}) = p_{ullage} + \rho_f g \tilde{z}. \tag{5.13}$$

The particulate solid load is measured through the Rankine active pressure [19].

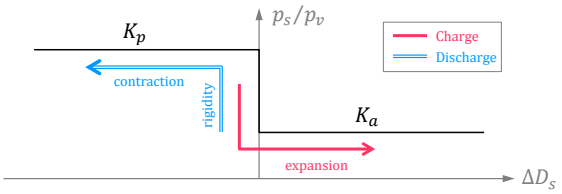

Figure 5.4: Bulk solid response using a rigid-perfectly plastic model.

It is based on the equilibrium of a bulk solid element like the one in figure 5.3, and defines a ratio between vertical, p_v, and lateral pressure, p_s. Compared with Jansen's theory, Rankine's does not consider any wall-filler friction ($\tau = 0$). This leads to a more conservative model which is appropriate for bunker-shape vessels like the thermocline ones [27]. Knowing the zero value of p_v at the bed free surface ($i = N_z$), the pressure at the bottom can be sequentially found in a discretised manner:

$$p_{v,i-1/2} = p_{v,i+1/2} + \rho_{buo,i} g \Delta z \,, \tag{5.14}$$

$$p_{v,i} = \frac{p_{v,i+1/2} + p_{v,i-1/2}}{2} \,, \tag{5.15}$$

where ρ_{buo} is the buoyant density of the solid in the fluid,

$$\rho_{buo,i} = (1 - \epsilon_i)\left(\rho_s - \rho_f\right) . \tag{5.16}$$

The ratio K_a between lateral and vertical pressure ($p_{s,i} = K_a p_{v,i}$), according to Rankine's theory, is given by:

$$K_a = \frac{1 - \sin(\phi)}{1 + \sin(\phi)} \,, \tag{5.17}$$

where ϕ is the angle of internal friction of the contained material.

The thermal load comes from the different thermal expansion between the bed and the tank wall [19]. When the temperature increases, the tank expands more than the filler, giving rise to a gap. The solid medium, assumed cohesionless, slumps downwards filling the gap. When the temperature decreases, the tank can only contract to the new dimension of the cooled inner solid,

$$D_{i,s}^{n+1} = D_{i,s}^{n} \left[1 + \alpha_s \left(T_i^{n+1} - T_i^{n}\right)\right] , \tag{5.18}$$

where α_s is the solid thermal expansion coefficient, $D_{i,s}^{n+1}$ is the bed diameter at the end

of a time interval (Δt), which moves from time iteration n to $n+1$.

The solid is preventing the total contraction of the wall by exerting a lateral load higher than the active pressure. Therefore, the wall strained radius is always forced not to be smaller than the bed one. When this limit is reached in one tank section i, its inner radial boundary condition changes from traction to Dirichlet, with the magnitude of the filler strain.

However, there is a maximum lateral resistance that a given soil can offer to a retaining wall that is pushing towards it. The soil will fail by shearing as soon as a maximum pressure known as passive pressure is reached [28]. The filler material can be simplified to a rigid-perfectly plastic material with a passive pressure limit, assuming the reaction of a loose cohesionless soil [29]. As a result, p_s is constrained to be less than or equal to the passive pressure. To evaluate this passive pressure, the ratio K_p is used following the next expressions [30]:

$$K_p = 1/K_a\,, \tag{5.19}$$

$$p_{s,i}^{\max} = K_p\, p_{v,i}\,. \tag{5.20}$$

In figure 5.4, the response of the filler material under the system thermal expansion is summarised. During cooling, the tank wall can only reduce its radius to the new diminished bed radius; the solid lateral pressure starts increasing, but its radius does not change. If cooling continues and the maximum passive pressure is reached, the aggregated solid fail by shearing and starts to reduce its radius. When heating, due to tank-filler differential expansion, the particles can freely expand, and lateral pressure can fall to the active value. Therefore, a day-periodic load history of relaxation-traction stress is expected in the tank over its service life.

Structural factors of safety As it has been stated, filler pressure and, consequently, tank wall stress grow during discharge. If wall stress rises above yield strength, all the thermal strain drop will not be able to change to elastic strain and a plastic deformation will appear. Since this tensile plastic strain cannot be removed, next heating strain will result in an increase of the total strain, i.e. the shell radius will enlarge. Then, rocks will settle down in the new gap which has been opened, and the process will start again. Yielding is set in each cooling and a radius increment in each heating. In the end, successive plastic deformation will induce cracks and probably a ratcheting collapse.

If the equivalent stress does not exceed yield strength, the strain diminished by temperature when cooling will be entirely compensated by elasticity and vice versa when

heating, without deforming plastically. Predicting yield by comparing the equivalent tensile stress with the material yield strength is formally known as the von Mises yield criterion, and is useful for multidimensional problems with ductile materials. The corresponding factor of safety against yielding is defined as:

$$\mathrm{FoS}_{static} = \frac{\sigma_y}{\sigma_{eq}}, \tag{5.21}$$

where σ_y stands for yield strength.

If this factor is maintained above one in all the tank geometry over its whole service life, no thermal ratcheting will appear. It has been referred to as "static" since it is defined only by the worst situation, the one in all the tank and in all the operation time in which the lowest value is reached. As a result, the factor is possibly too conservative. The structure may be plastically deformed only on a specific day, but this fact is not dangerous in terms of thermal ratcheting since ratcheting requires repeated plastic deformation.

Consequently, in order to take into account the dynamic cyclic behaviour of the system (daily relaxation-traction stress), another factor of safety has been defined. It is evaluated similarly to the yield factor of safety used in the Goodman relation for classical S-N (stress-life) fatigue analysis [31, 32] (figure 5.5). The resulting formulation contains the daily averaged minimum and maximum equivalent stresses.

$$\mathrm{FoS}_{dynamic} = \frac{\sigma_y - \bar{\sigma}_{eq,\min}}{\bar{\sigma}_{eq,\max} - \bar{\sigma}_{eq,\min}}. \tag{5.22}$$

In this manner, if there is no stress oscillation ($\bar{\sigma}_{eq,\min} = \bar{\sigma}_{eq,\max}$), a high safety factor will be obtained. But if there is oscillation and the maximum stress repeatedly approaches the yield limit, then the factor of safety will drop.

5.3 Model validation

The experimental non-commercial 170 MWht thermocline system of Solar One Pilot Plant is taken as a sample of performance of these storage tanks [7, 18, 19]. Although this first large-scale thermocline tank differs from what today is projected, e.g. in the use of hydrocarbon oil as HTF in place of molten salts, the thermo-mechanical behaviour is qualitatively identical. Furthermore, since the case has been experimentally tested (bed temperature and wall stress), it can be used to validate the developed mathematical model.

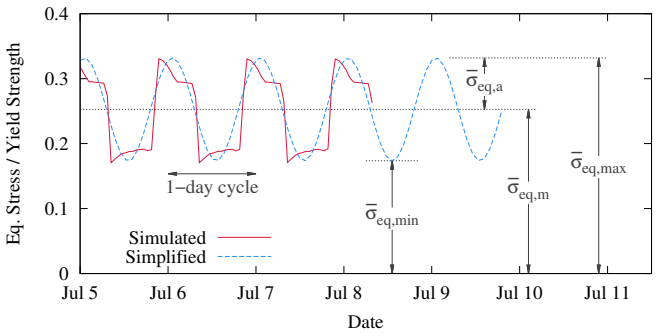

Figure 5.5: Load history of reference case $\mathscr{G}$ tank (defined in figure 5.4) at h = 6 m with the nomenclature for the simplified constant amplitude cyclic loading.

5.3.1 Case definition

Keeping in mind the validation purpose of this case, only two days of operation will be simulated. The first one, with an initial bed temperature of T_{cold} at 9 am, represents the system start-up and has the most significant variations in stress-strain physics. The second is a good example of the normal tank performance, but still with a high temperature stratification.

Solar One thermocline tank is a cylindrical vessel 18.2 m in inner diameter and 14 m high, composed of carbon manganese-silicon steel plates (A537 Class 2), and covered by 0.229 m of fibreglass insulation. The steel wall plate thickness decreases discretely from bottom to top as follows: 0.0286, 0.019, 0.0156, 0.0095, 0.0079 and 0.019 m. A total of six plates: the one below, with a height of 1.8 m, is followed by four plates 2.86 m high, and the last one is 0.38 m.

Inside an oil known as Caloria HT-43 works as HTF. The resulting fillerbed composition is, according to [7], from bottom to top: 0.66 m of sand-only region (porosity $\epsilon = 0.4$ and effective particle diameter $d_s = 0.002$ m), 1.1 m of rocks ($\epsilon = 0.4$ and $d_s = 0.05$ m), 10.5 m of quartzite rock and sand mixture ($\epsilon = 0.22$ and $d_s = 0.0046$ m) and 0.5 m of rocks again. The ullage is filled by nitrogen pressurised to 2240 Pa above atmospheric pressure.

Physical properties for the fluid, the particulate solid and the steel are presented in table 5.1. Temperature-dependent physical properties of steel are tabulated in the original source and are treated as piecewise linear functions in the code. Data for the insulation material have been taken from [7].

Table 5.1: Thermo-physical properties of the main materials used in the simulations. SI units.

Solar salt [33]	
ρ	1873.8
c_p	1501.5
k	$4.43 \times 10^{-4} + 1.98 \times 10^{-8} T$
μ_f	$2.2714 \times 10^{-2} - 1.24 \times 10^{-4} T + 2.281 \times 10^{-7} T^2 - 1.474 \times 10^{-10} T^3$
Caloria HT-43 [7]	
ρ	692.4
c_p	2700
k	$1.25 \times 10^{-4} - 1.4 \times 10^{-7} T$
μ_f	$132.73 T^{-2.207}$
Sand and quartzite rock [7, 18]	
ρ	2643
c_p	1000.5
k	2.2
ϕ	30°
α	7.92×10^{-6}
Steel A537 Class 2 (from 477 K to 577 K) [34]	
ρ	7850
c_p	[512, 547]
k	[53.5, 49]
E	$[1.92 \times 10^{11}, 1.84 \times 10^{11}]$
ν	0.3
α	$[1.39 \times 10^{-5}, 1.49 \times 10^{-5}]$
σ_y	$[3.11 \times 10^{8}, 2.82 \times 10^{8}]$
$T_{\max}$	371
Steel A387 Grade 91 (from 563 K to 663 K) [34]	
ρ	7850
c_p	[541, 600]
k	[27.3, 27.8]
E	$[1.95 \times 10^{11}, 1.88 \times 10^{11}]$
ν	0.3
α	$[1.26 \times 10^{-5}, 1.32 \times 10^{-5}]$
σ_y	$[3.76 \times 10^{8}, 3.61 \times 10^{8}]$
$T_{\max}$	649
Nickel alloy N06022 (from 563 K to 838 K) [34]	
ρ	8691
c_p	[482, 532]
k	[15.2, 20.8]
E	$[1.91 \times 10^{11}, 1.75 \times 10^{11}]$
ν	0.3
α	$[1.32 \times 10^{-5}, 1.74 \times 10^{-5}]$
σ_y	$[2.16 \times 10^{8}, 1.88 \times 10^{8}]$
$T_{\max}$	1250

In order to copy the actual working conditions of the tank as much as possible, in this specific case the inlet variables are not managed by equations 5.1-5.6, but they are directly imposed: temperature, mass flow and timing. Regarding the modes of operation reported in [35], the oil worked from a hot temperature of 304 ºC to a cold one of 204 ºC. The oil mass flow pumped into the tank was highly variable and difficult to measure. For this study, a constant average flow rate of 70 kg/s, both for charge and discharge, is considered. However, since the bed starts from a uniform temperature of T_{cold}, the mass flow is increased to 90 kg/s for the start-up charge in order to warm the system completely. Every charge-discharge-standby cycle lasts one day; charge starts at 9 am and discharge at 6 pm. The processes are stopped taking into account a cut-off temperature increment ΔT_{CO} of 4 ºC.

Bed and fluid have been discretised axially in 500 control volumes, and the automatically fitted time step [36] is around 4 s. The tank shell element for the thermoelastic problem has been divided axially into 400 sections, and radially in 3 sections. Its physics does not require such a small time increment, thus one of 900 s is used.

5.3.2 Results

A summary of the most relevant results for the Solar One storage tank during the start-up is presented in figure 5.6. As a result of the external insulation, wall temperature is always very close to the fluid temperature, and it is not really affected by the environment variable conditions. The major difference between bed and wall temperatures is appreciated near the ground, at around 1 m high, when the tank is fully charged (figure 5.6 (a) "+ 9 h" curve). It is due to the fillerbed composition and the derived oil-shell convection coefficient, which is changing abruptly from sand to rock layer (from 0.002 to 0.05 m in d_s).

Besides, the thermocline degradation throughout day-cycles is also noticeable. The initial condition in the first charge process (at 9 am) is a uniform cold temperature along the tank. For the next cycles, the initial condition of the bed is not a uniform temperature anymore, but a gradient temperature resulting from the previous discharge process and the requirements imposed on the outgoing fluid temperature. Since the difference between the incoming fluid temperature and that of the filler material is lower than in the 1st charge process, the thermal gradient and hence the heat transfer rate are also lower in the following cycles. Therefore, during the consecutive charge-discharge cycles, the thermal gradient tends to get "flattened" until a periodic steady state is reached. Due to this thermocline degradation, the stored energy in the periodic

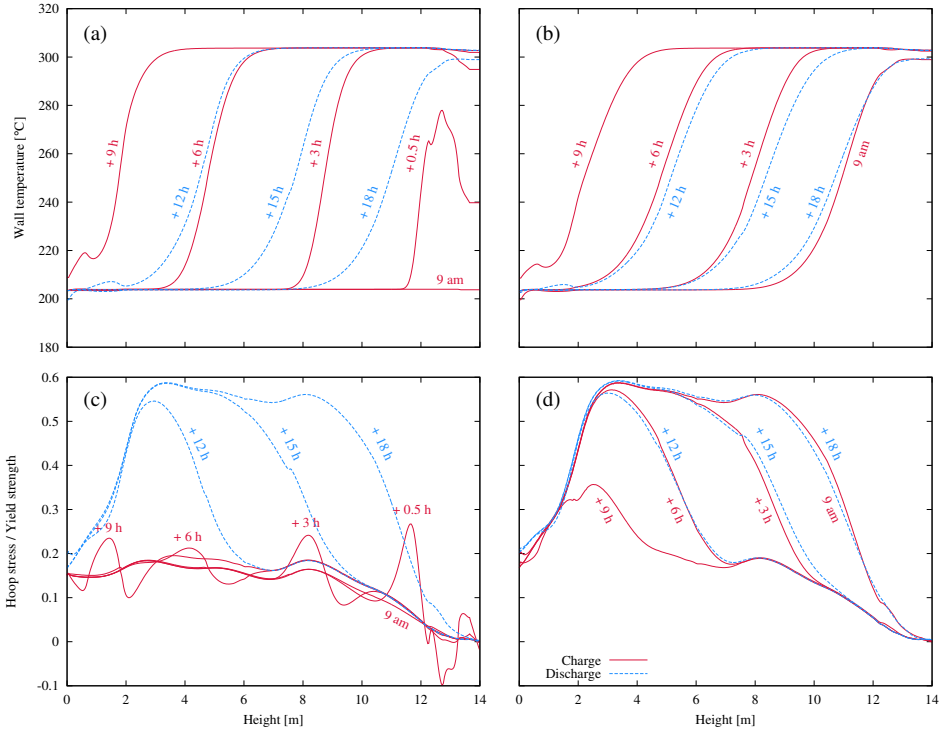

Figure 5.6: Summary of the Solar One thermocline start-up. Tank wall temperature during the first (a) and the second day (b); and tank wall hoop stress during the first (c) and the second day (d). Profiles belonging to charge (solid lines) and discharge (dashed lines) processes.

state is lower than that of the initial cycles, and so is the operation time, since outlet thresholds are reached earlier.

Figure 5.6 also includes the shell hoop stress $\sigma_{\theta\theta}$ resulting mainly from the weight of the inner substances and from bed-shell differential thermal expansion. Any pressure applied by inner substances generates a radial stress σ_{rr} that varies from the value of this pressure p on the interior surface, to p_{atm} outside. As simplified pressure vessel theory deduces, the hoop stress required to balance a cross tank section is much higher than this internal radial stress:

$$\sigma_{\theta\theta} \approx p\frac{D_{int}}{2e}, \tag{5.23}$$

which means that $\sigma_{\theta\theta}$ would be approximately 455 times larger than σ_{rr} in this case. Concerning axial stresses σ_{zz}, as long as there is no vertical restriction, they will be caused by the own weight of the structure and by the torsion phenomenon of large axial temperature gradients [37, 38]. Similarly to σ_{rr}, the effect of σ_{zz} in the equivalent stress is very low. That is why, though the three-dimensional thermoelastic model is evaluating all components of the stress tensor, only the hoop stress is highlighted.

The stress state at the beginning of the simulation is only due to hydrostatic fluid pressure and gravel active load because homogeneous heating from ambient temperature to T_{cold} does not produce any perceptible stress. Hoop stress directly proportional to this pressure, which increases linearly from top to bottom, is developed. As it is depicted in figure 5.6 (c) at "9 am", $\sigma_{\theta\theta}$ profile is not linear owing to the variable wall thickness.

In the course of the first heating (from "9 am" to "+ 9 h"), when the fluid sets the highest stratification and there is still no particle settlement, a wave of hot-compressive/cold-tensile hoop stress moves together with the temperature gradient. Once the gradient has passed a specific height, the circumferential stress returns to its previous value in that point. The apparent remaining stress increment that can be seen in the graph is only due to the reduction in the yield strength with high temperatures, the absolute hoop stress does get its old value.

During discharge (from "+ 12 h" to "+ 18 h"), radial contraction is restrained down to the new radius of the filler material. That is, as it is cooled, filler pressure rises and accordingly the thermal hoop stress. In this case, the solid pressure never exceeds the passive pressure of equation 5.20, hence there is no plastic deformation of the particulate solid, i.e. it is always responding rigidly. This means that filler pressure rise and thermal hoop stress are proportional to the temperature drop in time. Therefore, after discharge, an almost constant thermal stress is observed between 4 and 8 m, in

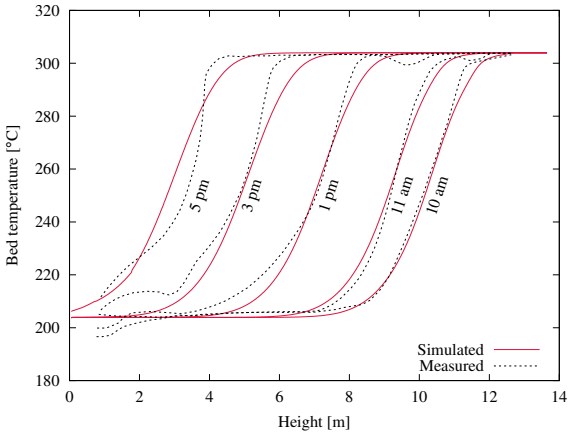

Figure 5.7: Temperature maps of Solar One bed during the second-day charge. Numerical simulation results (solid lines) and measures on May 18, 1983 [35] (dashed lines).

which ΔT is nearly 100 ºC. This thermal hoop stress is added to the elastic stress the structure has at the beginning of the simulation. Consequently, the maximum stress relative to the yield strength the structure must withstand is almost 0.6 at 3.4 m from the ground as a combination of thickness, maximum temperature variation in time and high active pressure. Being $\sigma_{eq} < \sigma_y$, the structure is always working within the elastic regime.

From this 1st cycle on, the structure relaxes every charging process (see figure 5.6 (d)). The thermal stress in a section is completely removed as soon as the temperature in that section reaches its historical maximum, at which the maximum radius of the bed was established. However, while discharge takes place, it is stressed from top to bottom following the temperature decrease and its tendency to contract.

5.3.3 Validation

The numerical solution for bed temperature during the second-day charging process, when the axial temperature gradient is still fairly large, is shown in figure 5.7. The results are compared with the bed temperature measurements collected by thermocouples installed in the storage unit of Solar One during May 18, 1983 [35]. Good agreement between experimental and numerical results is observed.

Nevertheless, whereas curves from the simulation show a similar gradient when

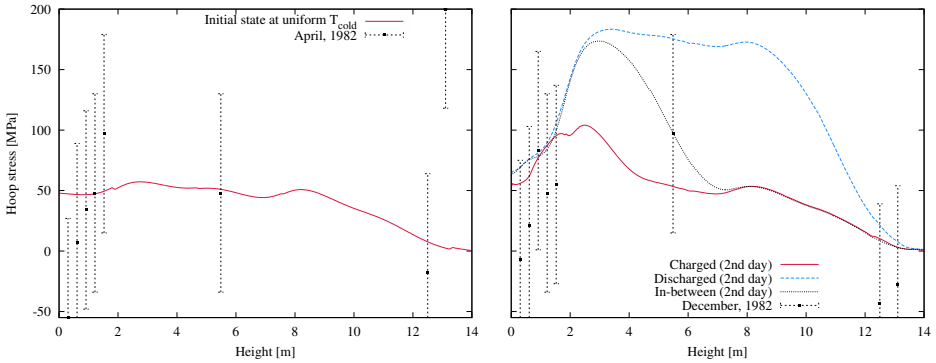

Figure 5.8: Hoop stress in Solar One thermocline tank. Characteristic simulation results (lines) and measured data [7] (dots).

reaching both temperature extremes, real profiles have a far sharper change of temperature in the hot part than in the cold part. The cycles preceding the measures may explain this. Focusing on the hot part of the thermocline, the colder the temperature reached at the top while discharging, the sharper the gradient of temperature in the following charging and thenceforth. Similarly for the cold part. Thus, it seems that before May 18, 1983, the cut-off temperature for discharge had been considerably lower than the one imposed in the simulation, 300 ºC.

Regarding the structural analysis, the only measured stresses from [7] have been used, even though according to the original authors, some of them were inconsistent with the problem physics and there was significant uncertainty. Measurement errors of around 56 MPa to 142 MPa were possible. In this work, an intermediate error of 82 MPa, mentioned in [7], has been considered.

Measurements and hoop stress resulting from the model are plotted in figure 5.8. Readings from April 1982, just prior to heating for the first time the thermal storage unit, are compared with the hoop stress at the beginning of the simulation. The data recorded after a few operating cycles in December 1982 are presented with the main results from the 2nd day because there is no information about the specific time when these stresses were measured. Numerical results of both cases come close to the recorded stress variability, and are within the range of uncertainty of the most reliable measures (the second, third and fourth point starting from the base according to [7]). The differences at the bottom part are likely to be due to the boundary condition, which in the simulation is only restricting vertical displacement, but not axial bending nor

Table 5.2: Location basic data. Here summer covers the months of June, July and August; and winter the months of December, January and February. T in [ºC], DNI in [Wh/m^{2}day] and t_{sun} in [h].

Location	$T_{\min}$	$T_{\max}$	$\overline{\text{DNI}}$	$\bar{t}_{sun}$
Granada, Spain				
Summer	13.3	35.1	8222	14.3
Winter	2.1	21.1	3739	9.8
Sevilla, Spain				
Summer	13.3	35.1	7280	14.2
Winter	2.1	21.1	4148	9.7
Upington, RSA				
Summer	-0.1	25.9	6670	10.0
Winter	14.9	39.6	8455	12.7

radial expansion.

More measured stresses in June 1984 revealed that an averaged hoop stress of 180 MPa was placed in the 0.6096 m to 1.219 m region. The magnitude is equal to the maximum stresses obtained from the simulation, but they are located between 3 m and 3.7 m. This suggests that Solar One tank would have been charged more than in the simulation, reaching higher temperatures near the ground. If there had been a similar heating in the simulation, the larger thermal stresses, consequence of the temperature variation, would have extended closer to the bottom.

Consequently, the whole numerical platform developed, including modelling and linking of all thermocline storage elements, agrees consistently with real temperatures and hoop stresses of packed-bed thermal storage tanks.

5.4 Definition of the cases

Having implemented and validated the simulation platform, and having understood the mechanical response of thermocline tanks, it is time to analyse their behaviour facing a real up-to-date situation. For this purpose, two CSP plants, which are currently working with a two-tank molten salt storage, have been selected as scenes to test different thermocline tank configurations. On the one hand, there is the Andasol-1 thermosolar plant based on a parabolic-trough technology with a temperature difference of 100 ºC. On the other hand, there is the Gemasolar plant which has a central tower receiver that raises the HTF temperature by 275 ºC. The reference case related to the former

will be referred to as $\mathscr{A}$, whereas the one placed in the latter will be referred to as $\mathscr{G}$. Here below, the particular specifications of case $\mathscr{A}$ [24, 39, 40] (those belonging to the tank have been extracted from the hot tank of the real plant):

- Plant configuration: $\dot{W}_{\mathrm{EG}}$ = 50 MW, S_{SF} = 510,120 m^2, T_{cold} = 290 ºC, T_{hot} = 390 ºC, η_{PB} = 0.38, η_{SF} = 0.7.
- Location: Aldeire (Granada, Spain). The meteorological data for the 8760 hours in a reference year have been generated by [41] (irradiation) and [42] (ambient temperature, wind, humidity, pressure). Essential data are given in table 5.2.
- Geometry: h_{tank} = 14 m, h_{bed} = 13.16 m. The tank appropriate diameter is determined in the next section.
- Materials: A387 grade 91 alloy steel for the tank shell, 0.4 m of Spintex342G100 for tank insulation and 0.001 m of aluminium as tank cover.
- Foundation thicknesses: 0.006 m of slip plate, 0.006 m of dry sand, 0.420 m of foam-glass, 0.060 m of hard fire-brick, 0.360 m of insulating fire brick, 0.450 m of heavy weight concrete and 9 m of soil.

Likewise, after consulting [43–45], the characteristics of case $\mathscr{G}$ can be listed:

- Plant configuration: $\dot{W}_{\mathrm{EG}}$ = 19.9 MW, S_{SF} = 306,658 m^2, T_{cold} = 290 ºC, T_{hot} = 565 ºC, η_{PB} = 0.40, η_{SF} = 0.42.
- Location: Fuentes de Andalucía (Sevilla, Spain). All the meteorological data are from [42] and are summarised in table 5.2.
- Geometry: h_{tank} = 11.2 m, h_{bed} = 10.5 m. The tank appropriate diameter is determined in the next section.
- Materials: N06022 nickel-chromium-molybdenum alloy for the tank shell, 0.4 m of fibreglass for tank insulation, and 0.001 m of aluminum as tank cover. Although the metal used in the hot tank of the real plant is an A240 grade 347 stainless steel, preliminary studies revealed that its yield strength (~140 MPa at 427.5 ºC) was too low for proposed thermocline storage. Therefore, following [34], the nickel alloy was chosen owing to its similar physical properties and to its higher resistance at moderate temperatures.

- Foundation thicknesses: 0.006 m of slip plate, 0.165 m of firebrick, 0.3 m of foam-glass, 0.23 m of insulating concrete, 0.61 m of concrete slab and 9 m of soil.

Vertical walls of both tanks have been divided uniformly into six plates with the thicknesses of the current Andasol hot tank. According to [24,25], they are, from bottom to top: 0.039 m, 0.032 m, 0.0255 m, 0.0185 m, 0.0115 m and 0.01 m.

Solar salt (60 % $NaNO_3$ + 40 % KNO_3) has been chosen as HTF for the reference cases, as it is employed in the original two-tank subsystems. Regarding the fillerbed, a mixture of two solids of differing particle diameter, e.g. rock and sand, is preferred because it allows closer packing and, thus, less fluid is required. A layer with only rocks surrounding the two manifolds prevents sand from entering in the piping system. Therefore, similarly to [5–7] designs, the fillerbed has been stratified in four layers of quartzite rock and silica sand. At the bottom, 1 % of the bed height is filled with sand. Above the sand layer and at the top, enclosing the manifolds, there are rock-only regions with a height of $0.08h_{bed}$. Sandwiched between these two layers is the mixture of rock and sand. Their porosity and effective particle diameter are like in the validation case. Moreover, air at atmospheric pressure is placed in the ullage space. Table 5.1 contains the physical properties of this gravel and the remaining materials.

Another common feature for both cases is the stop/restart criteria for charge and discharge processes. They have been defined respectively by the following temperature increments: ΔT_{CO} = 15 ºC and ΔT_R = 10 ºC. The cut-off temperature takes into account the acceptable range of temperature entering into the solar field and power block [46,47]. Besides this, the period of plant operation has been the same in the simulations too. May is left for reaching the periodic cyclic state, independent of the initial conditions of the first cycle. After that, the daily service during June, July and August is used for the result collection and processing.

Finally, considering their height, $\mathscr{A}$'s tank has been axially discretised in 800 control volumes, whereas $\mathscr{G}$'s has needed 638. After a mesh refinement study, it was found that there was less than 1 % and 2 % difference in the numerical results with refined meshes of double number of control volumes concerning case $\mathscr{A}$ and $\mathscr{G}$, respectively.

Simulating this period by the wall three-dimensional thermoelastic method has a high computational cost to carry out a suitable parametric analysis. It has been proved that fairly similar strain-stress results can be obtained with a one-dimensional (z) model analogous to that used for pressure vessels. It just considers the principal stresses: σ_{rr} takes $p_f(\tilde{z})$ value, σ_{zz} derives from the structure's own weight only (no bending effect), and $\sigma_{\theta\theta}$ is evaluated via equation 5.23. The boundary conditions are strictly maintained. In Solar One validation exercise, height-averaged discrepancies of

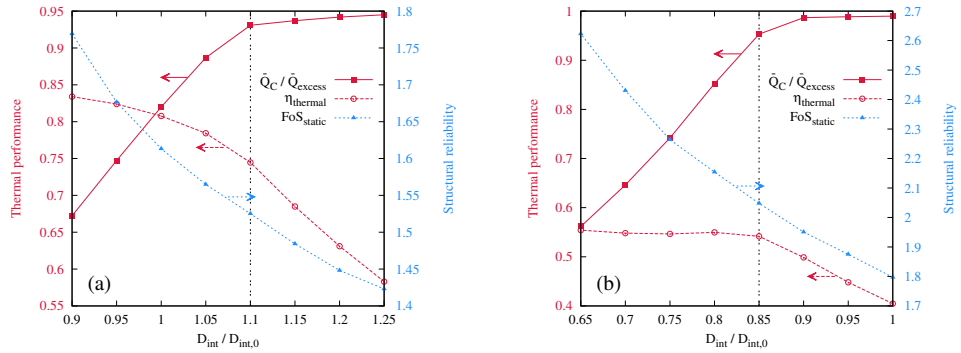

Figure 5.9: Change on some $\mathscr{A}$ (a) and $\mathscr{G}$ (b) operating conditions due to tank diameter. Thermal energy stored relative to the excess energy from the solar field, thermal efficiency and static factor of safety.

Table 5.3: Mass confined (ton) and storage capacity (MWh) of the reference tanks and those with the original two-tank molten salt storage radius, $D_{int,0}$.

	Case $\mathscr{A}$		Case $\mathscr{G}$	
$D_{int}/D_{int,0}$	1.1	1	0.85	1
Mass of filler material	35758	29552	6242	8639
Mass of confined fluid	8487	7014	1481	2050
Filler storage capacity	994	821	477	660
Fluid storage capacity	354	293	170	235
Total storage capacity	1348	1114	647	895

the simplified model compared with the general 3D theory were less than 7 % while the difference in the maximum stress, located at z = 3.4 m, was ~3 %. By using this model for the parametric study, a good approximation of tank stress response and its trends over normal operating periods will be assessed.

5.4.1 Definition of the tank volume

The authors of [36] noticed that, in the Andasol plant, the packed-bed tank should be larger than the hot two-tank to gain the thermal energy lost by thermocline degradation.

The tank volume will be determined by the radius only, keeping the original height previously mentioned fixed. In the course of the study, the diameter of the real two-tank subsystem is taken as a reference. In the Andasol plant, the hot tank diameter, $D_{int,0}$,

is 38 m, whereas in Gemasolar it is 23 m. The optimal volume will have to balance safety, thermal performance and cost during the three months previously defined. The first requirement is measured by the most conservative structural factor of safety (see equation 5.21). The second, by the capability to store the excess thermal energy of the plant, i.e. the part of the solar energy that is not needed in the power block,

$$\dot{Q}_{excess} = \dot{Q}_{\mathrm{SF}} - \dot{Q}_{\mathrm{PB}}\,. \tag{5.24}$$

For the stored energy, enthalpy difference is evaluated at each portion of the fluid and solid discretised domains. The thermal energy stored over the time step moving from iteration n to $n+1$ results in:

$$Q_{C,f}^{n+1} = \sum_i \rho_f \epsilon_i V_i c_{p,f} \left(T_{i,f}^{n+1} - T_{i,f}^{n}\right), \tag{5.25}$$

$$Q_{C,s}^{n+1} = \sum_i \left[\sum_j \rho_s V_{i,j} c_{p,s} \left(T_{i,j}^{n+1} - T_{i,j}^{n}\right)\right], \tag{5.26}$$

$$Q_{C}^{n+1} = Q_{C,f}^{n+1} + Q_{C,s}^{n+1}\,. \tag{5.27}$$

The day stored heat is obtained by adding all stored energies throughout a charge process. With this, a three-month operating period will be summarised by the daily averaged energies as $\bar{Q}_C/\bar{Q}_{excess}$.

The economic side is outlined thanks to thermal efficiency. It is evaluated as the thermal energy stored in the tank divided by its ideal storage capacity,

$$\eta_{th} = \frac{\bar{Q}_C}{Q_{storable}}, \tag{5.28}$$

where $Q_{storable}$ is calculated as the heat needed to raise the temperature of the entire tank from T_{cold} to T_{hot}.

How do these variables behave facing a change in volume? If the tank is too small, its storage capacity is small, and it will be unable to accumulate all the plant surplus solar energy ($\bar{Q}_C/\bar{Q}_{excess}$ less than one). By contrast, if it is overdimensioned, it will store this energy ($\bar{Q}_C/\bar{Q}_{excess}$ close to one), but it will not be using all its height, since there is not enough energy to charge it completely. This means a drop in η_{th} and a tendency of the thermal gradient to spread across a big part of the height (high thermal degradation, low stratification). In other words, there will be an unneeded stock of salt and rocks in the storage system. In addition, from equations 5.13 and 5.14 it is known

Table 5.4: Inner diameter, bed height and aspect ratio of the reference cases and their aspect ratio variations, AR1 and AR2.

	Case $\mathscr{A}$			Case $\mathscr{G}$		
	Base	AR1	AR2	Base	AR1	AR2
D_{int} [m]	41.8	37.91	46.09	19.55	15.84	24.13
h_{bed} [m]	13.16	16	10.82	10.5	16	6.89
AR	0.31	0.42	0.23	0.54	1.01	0.29

that inner pressure will not change because it only depends on the depth $\tilde{z}$. Even so, as can be observed from equation 5.23, the larger the radius, the higher the stress in the tank shell, i.e. the less FoS.

An overview of the simulations is presented in figure 5.9, where all three requirements of the optimal volume are plotted. The trend is pretty similar in both cases $\mathscr{A}$ and $\mathscr{G}$. At first, when the volume is not big enough to accommodate all the thermal energy, the tank is fully heated in every charge process, which results in a steady high efficiency. When raising the radius, there is a particular point beyond which the tank is already storing almost all the energetic surplus, and the efficiency starts falling due to growing non-used bed height. In terms of structural reliability, the factor of safety decreases steadily with the radius as expected, but never arising material yielding.

It turns out that the original volume of case $\mathscr{A}$ is too small for the magnitudes of its plant, while it is oversized for case $\mathscr{G}$. Observing figure 5.9 (b), the optimal diameter of $\mathscr{G}$ should be between $0.85D_{int,0}$ and $0.9D_{int,0}$. Prioritising thermal efficiency, $0.85D_{int,0}$ is chosen for the reference tank $\mathscr{G}$. As for case $\mathscr{A}$, efficiency has a perceptible stagnation beyond $D_{int} = 1.1D_{int,0}$. Accordingly, this diameter is selected for $\mathscr{A}$, as it also lies on the smooth decline of the efficiency curve. In table 5.3, there are the masses filling each sized tank as well as their storage capacity.

5.4.2 Definition of the parameters

The parametric analysis has been carried out in order to distinguish critical factors that might compromise the structural integrity of a thermocline packed bed tank and, at the same time, to assess their effects from a thermal point of view. Sized tanks of section 5.4.1 are treated as base cases (code B). Five different parameters of these cases have been altered so as to generate the new prototypes:

1. Bed aspect ratio (h_{bed}/D_{int}). Two different geometric configurations have been tested: one taller than the reference tank (code AR1) and another shorter (AR2);

both with the same volume and the same quantities of salt, rock and sand. First, the height of AR1 is set to 16 m, the maximum allowed according to [6]. Therefore, the corresponding diameter which preserves the volume can be found. The inverse of the change in aspect ratio of AR1 is then applied to define AR2. The diameter is restricted to a maximum of 48 m underlined in [5]. The final geometry of each case is presented in table 5.4. The new configurations are made up of plates of the same height and thickness as the reference case. The taller case uses the thinnest plate of 0.01 m to reach 16 m high. AR2 places the same plates from bottom to top reaching the new height. The discretisation of these prototypes has been adapted to keep the same Δz of the base cases.

2. Cut-off temperatures. One case (CO1) has wider admissible temperature intervals for both charge and discharge processes: ΔT_{CO} = 25 ºC. The opposite one (CO2) has narrower intervals: ΔT_{CO} = 5 ºC. ΔT_R is kept unchanged.

3. Season. While the base case works from May to August, this case (S1) runs from November to February.

4. Location. The location of Upington, in South Africa, has been selected to place the reference plants during summer (L1) and winter (L2).

5. Wall thickness. A new tank with 50 % thicker thicknesses of the metal tank shell has been tested (T1).

5.5 Results and discussion

Tables 5.5 and 5.6 show the averaged quantitative results obtained from the simulation of the different cases considered, after the periodic state has been reached. Firstly, the focus will be on the main differences between base cases $\mathscr{A}$ and $\mathscr{G}$ and then on the effect of each parameter. But before this, it is necessary to explain some new variables attached in the tables:

- For evaluating the power generation potential of the energy delivered by the thermal storage, the global exergy balance of the HTF is calculated in the following manner (see figure 5.2):

$$\dot{B}_D = \dot{m}_D c_{p,f} \left(T_D^{out} - T_{\mathrm{PB}}^{out} - T_{ref} \ln \frac{T_D^{out}}{T_{\mathrm{PB}}^{out}} \right), \tag{5.29}$$

Table 5.5: Daily averaged performance results for each $\mathscr{A}$ configuration.

Results	B	AR1	AR2	CO1	CO2	S1	L1	L2	T1
Energy from SF, $\bar{Q}_{\mathrm{SF}}$ [MW h]	2936	2936	2936	2936	2936	1335	2382	3019	2936
Excess energy / Energy from SF, $\bar{Q}_{excess}/\bar{Q}_{\mathrm{SF}}$ [%]	37	37	37	37	37	16	48	49	37
Stored energy / Excess energy, $\bar{Q}_C/\bar{Q}_{excess}$ [%]	93	93	93	93	74	100	89	69	93
Delivered energy / Stored energy, $\bar{Q}_D/\bar{Q}_C$ [%]	100	100	100	100	100	99	100	100	100
Delivered exergy, $\bar{B}_D$ [MW h]	485	486	484	487	386	100	491	490	485
Energy lacking / Energy needed, $\bar{Q}_{lacking}/\bar{Q}_{\mathrm{PB}}$ [%]	8	8	8	8	15	58	28	17	8
Energy losses [MW h]	2.07	2.04	2.14	2.06	2.08	1.92	2.04	2.08	2.06
Charge time [h]	12.1	12.1	12.0	12.1	9.5	5.3	7.5	7.8	12.1
Discharge time [h]	8.6	8.6	8.5	8.6	6.7	2.8	8.4	8.4	8.6
Charged stand-by time [h]	1.0	0.9	1.0	0.9	3.5	0.0	0.9	3.0	1.0
Discharged stand-by time [h]	2.4	2.4	2.4	2.3	4.2	15.9	7.2	4.8	2.4
Time with $T_C^{out} < T_{cold} + 5$ [%]	97	97	97	97	100	100	96	97	97
Time with $T_D^{out} > T_{hot} - 5$ [%]	97	97	95	96	100	90	95	95	96
Thermal efficiency, η_{th} [%]	74	75	74	75	59	16	76	76	74
Thermocline height / Bed height, h_{th}/h_{bed} [%]	16	15	17	14	29	21	15	15	16
Static factor of security, FoS_{static}	1.5	1.1	1.7	1.5	1.5	1.5	1.5	1.5	2.2
Dynamic factor of security, $\mathrm{FoS}_{dynamic}$	2.4	1.5	3.2	2.4	2.4	5.5	2.4	2.4	4.0

Table 5.6: Daily averaged performance results for each $\mathscr{G}$ configuration.

Results	B	AR1	AR2	CO1	CO2	S1	L1	L2	T1
Energy from SF, $\bar{Q}_{\mathrm{SF}}$ [MW h]	938	938	938	938	938	534	859	1089	938
Excess energy / Energy from SF, $\bar{Q}_{excess}/\bar{Q}_{\mathrm{SF}}$ [%]	39	39	40	39	39	32	46	45	39
Stored energy / Excess energy, $\bar{Q}_C/\bar{Q}_{excess}$ [%]	95	99	78	99	31	99	84	66	94
Delivered energy / Stored energy, $\bar{Q}_D/\bar{Q}_C$ [%]	100	100	100	100	98	100	100	100	100
Delivered exergy, $\bar{B}_D$ [MW h]	190	196	156	196	61	91	179	177	189
Energy lacking / Energy needed, $\bar{Q}_{lacking}/\bar{Q}_{\mathrm{PB}}$ [%]	22	22	28	21	43	55	33	22	23
Energy losses [MW h]	0.96	1.02	0.96	0.93	1.00	0.93	0.97	0.96	0.96
Charge time [h]	9.1	9.7	7.3	9.7	3.6	5.5	7.0	7.3	9.1
Discharge time [h]	8.0	8.2	6.7	8.2	3.1	4.2	7.3	7.3	7.9
Charged stand-by time [h]	0.6	0.0	2.4	0.0	6.1	0.0	1.4	3.3	0.6
Discharged stand-by time [h]	6.3	6.1	7.6	6.1	11.2	14.3	8.4	6.1	6.4
Time with $T_C^{out} < T_{cold} + 5$ [%]	93	96	91	95	100	99	94	94	93
Time with $T_D^{out} > T_{hot} - 5$ [%]	93	95	90	91	100	91	93	93	93
Thermal efficiency, η_{th} [%]	54	56	45	56	18	26	51	50	54
Thermocline height / Bed height, h_{th}/h_{bed} [%]	42	38	55	40	75	62	45	44	43
Static factor of security, FoS_{static}	2.0	0.9	2.7	2.1	2.1	2.1	2.0	2.0	3.1
Dynamic factor of security, $\mathrm{FoS}_{dynamic}$	3.4	0.9	5.2	3.5	3.7	4.2	3.4	3.5	5.6

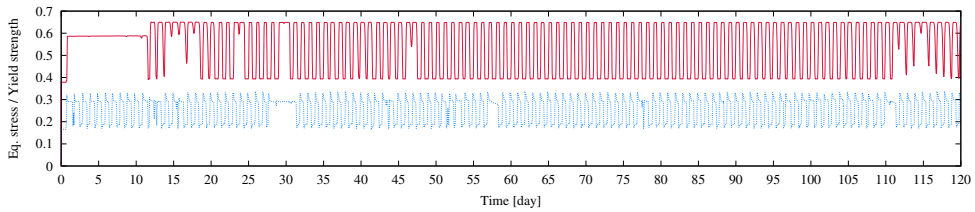

Figure 5.10: Total load history of base cases (B): tank $\mathscr{A}$ at $h = 7$ m (solid line) and tank $\mathscr{G}$ at $h = 6$ m (dashed line).

where T_{ref} is the temperature corresponding to the dead state, which in this work has been taken as 45 ºC due to being a reasonable value for the temperature at which vapour is condensed in the power generation block.

- Stand-by periods result from two types of imbalance: thermal energy in excess (the tank has been fully charged and there is still radiation), and lacking thermal energy (the tank has been already discharged and there is no radiation). The former forces to throw part of the available solar energy and the latter to resort to an alternative heat source, i.e. fossil fuels, to cover the thermal demand of the power block. This scarcity is presented in the tables relative to the total thermal energy requested by the generation subsystem to have firm capacity ($\bar{Q}_{lacking}/\bar{Q}_{\mathrm{PB}}$).

- The thermocline thickness h_{th} is measured as another indicator of thermal performance. Its formulation is similar to that proposed by [46]:

$$h_{th} = \begin{cases} \frac{h(T_{hot,c})\,\Delta T_{th}}{T_{hot,c} - T_{bottom}}, & T_{bottom} > T_{cold,c} \\ \frac{(h_{bed} - h(T_{cold,c}))\,\Delta T_{th}}{T_{top} - T_{cold,c}}, & T_{top} < T_{hot,c} \\ h\left(T_{hot,c}\right) - h\left(T_{cold,c}\right), & \text{elsewhere} \end{cases} \tag{5.30}$$

where $T_{hot,c}$ and $T_{cold,c}$ are the critical cold and hot temperatures for delimiting the thermocline thickness, respectively; and $\Delta T_{th} = T_{hot,c} - T_{cold,c}$. In the present study, $T_{hot,c}$ has been chosen to be $T_{hot} - 15$ and $T_{cold,c}$ to be $T_{cold} + 15$.

5.5.1 $\mathscr{A}$ versus $\mathscr{G}$

Observing the first row of tables 5.5 and 5.6, one may notice that solar thermal energy received throughout a day in $\mathscr{A}$ is significantly higher than that in $\mathscr{G}$. The causes are three: a larger collector's area (1.66 times larger in $\mathscr{A}$), a greater collecting efficiency (1.67 times), and a greater solar irradiation (1.13 times). Unfortunately, this total source represents only 93 % and 79 % of the thermal energy required by $\mathscr{A}$ and $\mathscr{G}$ power blocks, respectively. Taking into account this limitation, it should be concluded that the sizing of base storage tanks was properly done since plant lacking energy agrees with these ideal values. In fact, both tanks keep about 95 % of the available surplus solar energy. Regarding the portion of solar energy not directly sent to generation and hence storable, it is almost equal in both cases owing to the similarity of the collector's area solar multiple: ~2.6 in $\mathscr{A}$ and ~2.7 in $\mathscr{G}$.

If attention is paid to cycle times, no further conclusion can be drawn. The lacking energy previously stated can also be seen in the number of hours $\mathscr{G}$ tank is in standby with no deliverable energy, 6.3 h. Increasing receiver area and, consequently, enlarging the storage tank, would reduce this idle time, as $\mathscr{A}$ does with only 2.4 h.

Another remarkable figure is thermal efficiency, which is considerably poorer in case $\mathscr{G}$. The fact is that $\mathscr{G}$'s thermal performance will never be as good as $\mathscr{A}$'s, provided that outlet temperature tolerances are the same in both cases (ΔT_{CO} = 15 ºC). With the same tolerance, the thermal gradient will be the same, but, since the temperature difference $T_{hot} - T_{cold}$ to overcome is larger in $\mathscr{G}$, the gradient region will be eventually wider there. This is clearly shown in figure 5.12. The result is that the tank $\mathscr{A}$ accumulates three-fourths of its ideal capacity, whereas $\mathscr{G}$ just half. These ideal capacities are almost equivalent to equally sized two-tank systems because the heat capacity ($\rho_f c_{p,f}$) of salt and quartzite are pretty similar.

In all cases, thermal losses are very low (less than 1 % of the energy delivered to the power block by the TES), which is an indication of having sufficient thermal insulation.

In terms of stress on the tank shell, the first thing worth mentioning is that both factors of safety are greater than one. According to simulations, it implies that the metal structure is never subjected to plastic deformation nor, as a result, to ratcheting. In addition, they are within the safety limit of 1.5 against yield failure recommended by [48]. Nevertheless, given the approximations made –regarding the particulate medium mechanics or the physical properties– more conservative factors would be preferable for a commercial design.

The disparity between static and dynamic factors of safety is simply due to the

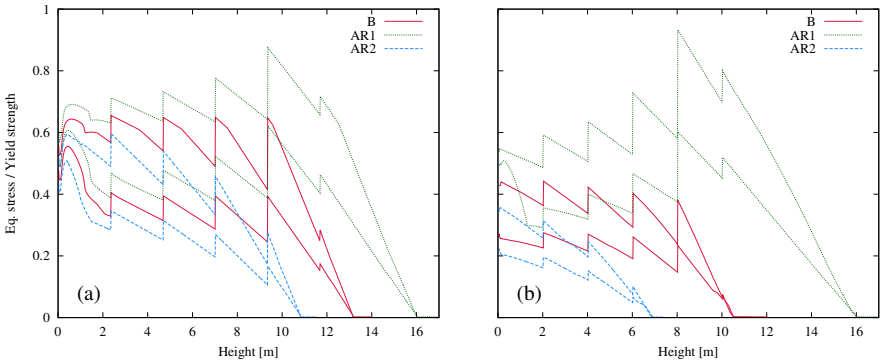

Figure 5.11: Wall equivalent stress for base cases and their aspect ratio variations on July 9. Maximum stresses belong to discharged state and minimum stresses to charged state. Case $\mathscr{A}$ (a) and $\mathscr{G}$ (b).

averaged minimum stress, which is only influencing the latter (see equation 5.22): the higher it is, the less stress oscillation, and the higher $\text{FoS}_{dynamic}$. The equivalent stress history presented in figure 5.10 shows that there has not been any particular day in which the stress was higher than usual. That is why there is no big effect of averaging the daily maximum and minimum stresses and it seems more reliable to focus on FoS_{static}, at least in these cases.

Comparing the safety factors of $\mathscr{A}$ and $\mathscr{G}$, an unexpected fact is revealed: $\mathscr{G}$ vessel is safer than $\mathscr{A}$ vessel, although temperature decline in $\mathscr{G}$ is almost three times larger than that in $\mathscr{A}$. To understand it, figure 5.11 should be examined first. The graph shows the maximum and minimum stresses reached on an average day, when the tank is fully discharged and fully charged, respectively (sudden changes in the profiles are due to the one-dimensional elastic model). As can be seen, maximum stresses are all roughly 0.2 points above the minimum ones, while in Solar One case there was a 0.4 point rise during discharge, as a proportional result of the 100 ºC temperature drop. The explanation is that in these new examples the maximum lateral resistance of the bulk solid, i.e. the passive pressure, has been reached, unlike what happened in the Solar One simulation.

However, why are these configurations reaching passive pressure if Solar One did not? The key is in the fluid density. The oil used in Solar One was four times lighter than quartzite gravel in such a way that solid pressure represents four-tenths of the total inner pressure (see equation 5.12). By contrast, in the reference tanks the fluid

is only 1.4 times lighter than the gravel. Fluid and rock densities are similar, hence rocks "float more" and provide just one-tenth of the total inner pressure (see ρ_{buo} of equation 5.16). It is known that passive pressure multiplies the active one by nine (due to the angle of internal friction), but if this latter hardly represents a minor part of the total, then the difference between total pressure with active response and total pressure with passive response will be minimum. Therefore, having a denser HTF ends up being beneficial from a structural point of view, because it reduces the rock pressure and prevents the total temperature difference effect, which would lead to considerably more dangerous stresses.

The increase in hoop stresses during discharge is not proportional to the temperature change but is just determined by the bed passive pressure. Thus, having a similar distribution of internal substance pressure, only tank size and thicknesses might create the difference between both cases $\mathscr{A}$ and $\mathscr{G}$. The tank shape discussion of the next section clarifies their influence over mechanical performance.

5.5.2 Effect of aspect ratio: AR1-AR2

Concerning thermal performance, the results agree well with the idea expounded on [5]. The taller the tank, the better. Since the space occupied by the thermocline gradient is the same (for a given temperature difference and a process outlet threshold), the more height, the more proportion of the volume can be warmed to T_{hot}. In case $\mathscr{G}$, the aspect ratio variations are more pronounced than in $\mathscr{A}$, and the differences in operation are more noticeable. Thermocline thickness falls from $0.42h_{bed}$ in the reference tank to $0.38h_{bed}$ in the higher modification (AR1), which allows it to collect 4 % more surplus energy. The shorter tank (AR2) instead, can only collect 78 % of this energy because of the relatively thicker thermocline. This constraint is forcing processes to extend more often to the cut-off point (outlet temperatures start to decay earlier).

In this manner, in spite of having equal storage capacity (same amount of fluid and gravel), the higher prototype is more efficient thermally and can accumulate more energy. In other words, if the vessel geometry is stretched, its volume can be reduced without altering the final storage capacity. This is particularly important as long as $T_{hot} - T_{cold}$ increases: with 100 ºC like in $\mathscr{A}$, a bed 10.82 m tall leads to efficiencies close to 80 %, whereas with 275 ºC, a bed height of 16 m is needed to at least arise a 60 %.

Wall equivalent stress plotted in figure 5.11 reveals its strong dependence on varying plate thickness. It has already been mentioned that fluid and rock pressure only depends

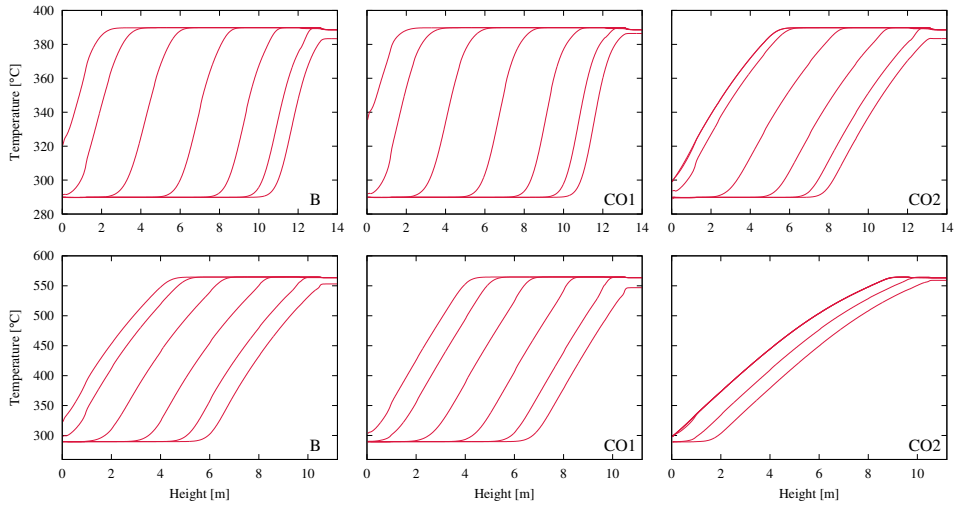

Figure 5.12: Wall temperature maps throughout charge on July 9. The curves are separated by a 2-hour interval and their chronological order is from right to left. $\mathscr{A}$ charge (top) lasted from 5 am to 5 pm and $\mathscr{G}$ (bottom) from 7 am to 5 pm.

on the depth measured from the bed surface ($\tilde{z}$). However, hoop stress is different at a common depth for all three modifications. It is a consequence of the traction developed on the wall under an inner pressure, which is proportional to D_{int}/e, as can be seen in equation 5.23. Although AR1 has a smaller diameter, the plate thickness for a certain depth is much smaller, resulting in a higher factor D_{int}/e and hoop stress. The opposite happens with AR2; the diameter is larger but the thicknesses are much larger, so stress eventually falls.

In the end, the higher tank seems equally preferable. Although the metal shell should be thicker in order to be structurally reliable, the economic investment could be balanced by the fluid and gravel savings, because it is more thermally efficient.

And this explains the difference aforementioned between base cases $\mathscr{A}$ and $\mathscr{G}$. Though the steel's yield strength is higher than the nickel alloy's (see table 5.1), the relative stresses presented in figure 5.11 are still higher in $\mathscr{A}$. The fact is that absolute stresses are much larger in $\mathscr{A}$ than in $\mathscr{G}$ because the factor D_{int}/e is much larger too.

5.5.3 Effect of cut-off temperatures: CO1-CO2

The base tank sizing procedure of section 5.4.1 is used for storing the maximum surplus solar energy. Both tanks were able to retain around 95 % of that energy. As a result, raising the cut-off tolerance to 25 ºC (CO1) is producing no remarkable difference as a TES. This strategy would be useful in a smaller tank. The tank would be able to accommodate the same heat with a higher efficiency, but having earlier-degrading outlet temperatures.

On the other hand, the reduced tolerance of ΔT_{CO} = 5 ºC negatively affects thermal operation. The thermocline height almost doubles, and so does the energy required from alternative sources. This thermal degradation is excessive in plant $\mathscr{G}$, as can also be identified in figure 5.12.

The conclusion is that a tank cannot have steady design outgoing temperatures and good thermal efficiency. The higher the tolerance in the temperatures entering the solar field and the power block, the better the efficiency and the smaller the tank needed.

There is another noteworthy feature in figure 5.12. Although both charge and discharge processes are stopped when the block inlet temperature deviates ΔT_{CO} from its design temperature, it seems that this tolerance is higher in charging than in discharging. This is easily noticeable in $\mathscr{A}$ prototypes shown in figure 5.12. Charge and power generation coincide (when there is sunlight). It means there is a cold HTF leaving the PB that is able to reduce the charge outlet temperature down to the cut-off temperature before entering the SF. By contrast, discharge and solar energy collection do not take place at the same time since discharge usually starts when there is no radiation. Therefore, the mixing effect of equation 5.6 hardly happens when there is discharge, and the temperature threshold is directly reflected inside the storage tank.

From a structural point of view, the impact of this parameter is negligible. Even so, due to the serious thermal degradation of $\mathscr{G}$'s CO2 modification, the tank does not reach such big temperature changes nor such maximum stresses once the steady cycle has been set. Therefore, $\text{FoS}_{dynamic}$ increases.

5.5.4 Effect of season: S1

The most critical parameter in the meteorological data is direct normal irradiance. From the averaged summary of table 5.2, it is known that DNI approximately halves during winter in Granada as well as in Sevilla. Looking at the sixth row of tables 5.5 and 5.6, one deduces that both plants can only deliver about 40-45 % electric energy from the

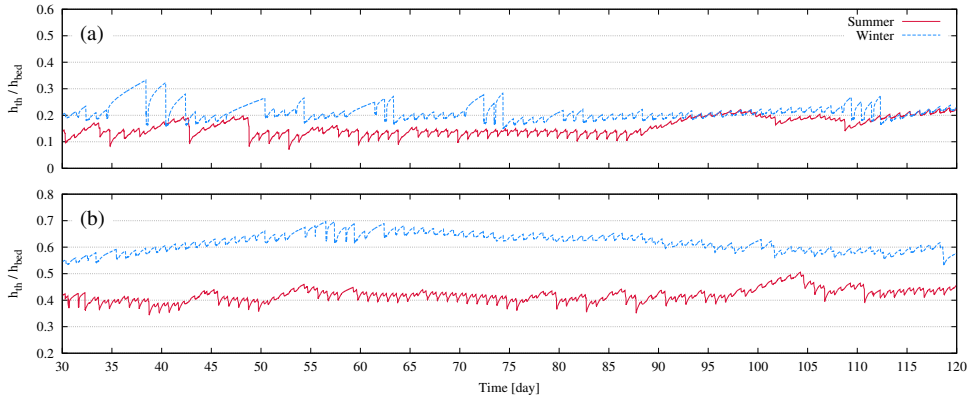

Figure 5.13: Thermocline height over a three-month period. $\mathscr{A}$ plant (a), located in Aldeire (Granada), and $\mathscr{G}$ plant (b), in Fuentes de Andalucía (Sevilla).

solar power in winter, other heat sources should provide the rest. Plant performance worsens considerably owing to seasonal variation in these two locations. For example, discharging time in $\mathscr{A}$ drops from 8.6 h during summer to 2.8 h in winter, while in $\mathscr{G}$ falls from 8 h to 4.2 h.

Now the focus will be specifically on the tank thermal efficiency and thermocline height. The former can be defined as the portion of the bed which is heated up to T_{hot} during charge. Therefore, it should be equivalent to consider the bed height (100 %) minus the thermocline thickness. Nevertheless, in all the studied combinations, this value is higher than the actual efficiency (see equation 5.28). This is a matter of weather since the daily radiation is not always able to fill the tank until its limit. This issue is especially present in winter. Taking into account the thermocline thickness, $\mathscr{A}$'s tank can accumulate a 79 % of what a zero-degradation thermocline TES would. But with the efficiency, this value is believed to be 16 %. Having rare solar irradiance, the extreme thermal degradation is damped in this case by reaching the cut-off temperature at every discharge. This places the temperature oscillation only at the top of the tank, where stresses are not the highest. That is why $FoS_{dynamic}$ soars to 5.5 in $\mathscr{A}$.

In figure 5.13 the temperature gradient length over the period of simulation is presented. Regardless of the inherent fluctuations related to processes and standby periods, it can be seen that $\mathscr{A}$'s thermocline is pretty stable and comparable throughout both periods summer and winter. The behaviour of $\mathscr{G}$ is reasonably different. Initially,

the storable energy is so scarce in winter that thermal degradation grows, and not until the end of the second month (day 60) is it starting to decrease.

Therefore, cold seasons do affect the thermocline, increasing the degradation. But this degradation can be progressively lessened with increasing sunny days. Structurally, winter and the consequent degradation reduce the temperature decline during discharge, and hence the stresses.

5.5.5 Effect of location: L1-L2

Upington is a fitting choice of CSP plant location because of its climate: sunny, warm and relatively constant throughout the year. Even so, and obtaining heat by the solar receiver similar to that of Spain, the tables prove that the defined TES does not adapt so well to this new place. Neither L1 nor L2 can even keep a 90 % of the energy available for storage, and eventually the dependence on alternative heat sources to assure plant firm capacity increases.

Tables 5.2, 5.5 and 5.6 show that, even though the solar receiver collects a similar amount of solar energy, it takes far less time to do it. Solar radiation is shorter but more intense than in Spain. This is reflected in the larger proportion of excess energy sent to storage, and in the shorter time devoted to charging. The resulting electrical power generated with warm fluid directly coming from the solar field falls, and the TES is asked to accumulate more thermal energy and retrieve it for a longer period.

This dominant role of TES within the plant would be satisfied employing larger tanks, both in $\mathscr{A}$ and $\mathscr{G}$. With the current capacity, the tanks are delivering the same exergy than in the reference cases: around 490 MWh over 8.4 h in $\mathscr{A}$ and around 180 MWh over 7.3 h in $\mathscr{G}$. However, they are not enough for the more extended periods with no radiation in Upington.

Concerning the stress-strain state of the walls, it can be seen that there is no variation since the inner materials and the work temperatures have not changed.

5.5.6 Effect of tank wall thickness: T1

The impact of changing the wall thickness is of minor relevance with respect to plant and storage performance. However, hoop stresses decrease approximately by a factor of 1.5, just what the thickness has risen. Thus, the results agree with the proportionality between $\sigma_{\theta\theta}$ and D_{int}/e already mentioned.

In order to arise a factor of safety against yield (and at the same time against

thermal ratcheting) close to two, case $\mathscr{A}$ would need about 50 % more wall thickness than a two-tank system, whereas $\mathscr{G}$ can be built with equal plates. As it has already been seen, it is not a matter of plant temperature difference, which is higher in $\mathscr{G}$ than in $\mathscr{A}$, but a matter of the larger size of tank $\mathscr{A}$.

5.6 Conclusions

A new validated numerical simulation platform for packed-bed thermocline energy storage tanks for CSP plants has been presented. It is able to dynamically solve and couple all its significant components to obtain the thermal and mechanical response of the subsystem over the plant's normal operation. The structure is studied using the thermoelastic theory for the tank wall and a rigid-perfectly plastic model with thermal expansion for the cohesionless bulk solid.

A broad thermo-mechanical parametric analysis is carried out in order to better understand whether the thermocline concept is a viable alternative for TES in CSP plants, regarding energetic effectiveness and structural reliability. It starts by sizing the thermocline storage system within two real commercial plants. The defined tanks work with solar salt as the HTF and a layered mixture of silica sand and quartzite rock as the filler material. A parabolic trough plant with 50 MW_e and 100 ºC of temperature difference leads to a 41.8×13.16 m (diameter×height) tank with 1010 MWh real storage capacity and 8.6 h delivering time. By contrast, a central tower plant with 19.9 MW_e and 275 ºC of temperature difference gives rise to a 19.55×10.5 m tank with 348 MWh thermal energy deliverable along 8 h.

Their thermal efficiency differs significantly, from 75 % in the former to 55 % in the latter, due to the importance of gradient degradation in each case. A lower plant temperature difference and a broader range of admissible temperatures in power block and solar field results in a better storage performance. Other factors like vessel geometric aspect ratio or seasonal weather variation also affect the storage capacity. Generally, the thermal operation of the 275 ºC thermocline is considerably poor. Thus, it seems appropriate to consider improvements, like the multi-layered solid-PCM (Phase Change Material) concept, for plants with a high temperature jump.

The numerical results show that material yielding, and hence thermal ratcheting, can be avoided in both cases with a factor of safety greater than two. A key aspect of its design involves tank walls with proper thickness, but not more than 0.06 m, made of a high yield strength metal and an HTF with a density of the same order as that of the fillerbed. As observed, tank wall stress can be summarised by hoop stress, because

the effect of radial stress, structure's own weight and temperature gradient bending is negligible in the equivalent stress.

References

[1] A. Gil, M. Medrano, I. Martorell, A. Lázaro, P. Dolado, B. Zalba, and L. F. Cabeza. State of the art on high temperature thermal energy storage for power generation. Part 1—Concepts, materials and modellization. *Renewable and Sustainable Energy Reviews*, 14(1):31 – 55, 2010.

[2] G. J. Kolb. Evaluation of annual performance of 2-tank and thermocline thermal storage systems for trough plants. *Journal of Solar Energy Engineering*, 133(3):031023 – 5, 2011.

[3] M. Liu, N. H. S. Tay, S. Bell, M. Belusko, R. Jacob, G. Will, W. Saman, and F. Bruno. Review on concentrating solar power plants and new developments in high temperature thermal energy storage technologies. *Renewable and Sustainable Energy Reviews*, 53:1411 – 1432, 2016.

[4] D. A. Brosseau, P. F. Hlava, and M. J. Kelly. Testing thermocline filler materials and molten salt heat transfer fluids for thermal energy storage systems used in parabolic trough solar power plants. Technical report, Sandia National Laboratories, Albuquerque, New Mexico, July 2004. SAND2004-3207.

[5] Solar thermocline storage systems: Preliminary design study. Technical report, Electric Power Research Institute (EPRI), Palo Alto, CA, June 2010. Project 1019581.

[6] J. E. Pacheco, S. K. Showalter, and W. J. Kolb. Development of a molten-salt thermocline thermal storage system for parabolic trough plants. *Journal of Solar Energy Engineering - Transactions of the ASME*, 124:153–159, 2002.

[7] S. E. Faas, L. R. Thorne, E. A. Fuchs, and N. D. Gilbertsen. 10 MWe solar thermal central receiver pilot plant: Thermal storage subsystem evaluation – Final Report. Technical report, Sandia National Laboratories SAND86-8212, 1986.

[8] S. M. Flueckiger, Z. Yang, and S. V. Garimella. An integrated thermal and mechanical investigation of molten-salt thermocline energy storage. *Applied Energy*, 88(6):2098–2105, 2011.

[9] G. Zanganeh, A. Pedretti, S. Zavattoni, M. Barbato, and A. Steinfeld. Packed-bed thermal storage for concentrated solar power – Pilot-scale demonstration and industrial-scale design. *Solar Energy*, 86(10):3084–3098, 2012.

[10] C. Mira-Hernández, S. M. Flueckiger, and S. V. Garimella. Comparative analysis of single- and dual-media thermocline tanks for thermal energy storage in concentrating solar power plants. *Journal of Solar Energy Engineering - Transactions of the ASME*, 137(3):031012–031012, 2015.

[11] B. M. Brown, M. N. Strasser, and R. P. Selvam. Development of a structured thermocline thermal energy storage system. In *Proceedings of ASES*, volume 74, 2012.

[12] F. Motte, S. L. Bugler-Lamb, Q. Falcoz, and X. Py. Numerical study of a structured thermocline storage tank using vitrified waste as filler material. *Energy Procedia*, 49:935 – 944, 2014.

[13] M. Wu, M. Li, C. Xu, Y. He, and W. Tao. The impact of concrete structure on the thermal performance of the dual-media thermocline thermal storage tank using concrete as the solid medium. *Applied Energy*, 113:1363–1371, 2014.

[14] Z. Yang and S. V. Garimella. Molten-salt thermal energy storage in thermoclines under different environmental boundary conditions. *Applied Energy*, 87(11):3322 – 3329, 2010.

[15] M. Hänchen, S. Brückner, and A. Steinfeld. High-temperature thermal storage using a packed bed of rocks – heat transfer analysis and experimental validation. *Applied Thermal Engineering*, 31(10):1798 – 1806, 2011.

[16] J. T. V. Lew, P. Li, C. L. Chan, W. Karaki, and J. Stephens. Analysis of heat storage and delivery of a thermocline tank having solid filler material. *Journal of Solar Energy Engineering*, 133(2):021003 – 10, 2011.

[17] P. A. Galione, C. D. Pérez-Segarra, I. Rodríguez, A. Oliva, and J. Rigola. Multi-layered solid-PCM thermocline thermal storage concept for CSP plants. Numerical analysis and perspectives. *Applied Energy*, 142:337–351, 2015.

[18] C. J. Bunnell and J. C. Powell. Solar Pilot Plant, Phase 1. Preliminary design report. Volume V. Thermal storage subsystem. CDRL Item 2. Technical report, Honeywell Energy Resources Center SAN-1109-8/7, May 1977.

[19] R. W. Hallet and R. L. Gervais. Central receiver solar thermal power system, Phase 1. CDRL Item 2. Pilot Plant Preliminary Design Report. Volume 5. Thermal Storage Subsystem. Technical report, McDonnell Douglas Astronautics Company SAN/1108-8/5, October 1977.

[20] S. M. Flueckiger, Z. Yang, and S. V. Garimella. Thermomechanical simulation of the solar one thermocline storage tank. *Journal of Solar Energy Engineering*, 134(4):041014–041014–6, 2012.

[21] G. J. Kolb, G. Lee, P. Mijatovic, and E. Valmianski. Thermal ratcheting analysis of advanced thermocline energy storage tanks. In *SolarPACES 2011*, Granada, 2011.

[22] B. D. Iverson, S. J. Bauer, and S. M. Flueckiger. Thermocline bed properties for deformation analysis. *Journal of Solar Energy Engineering*, 136(4):041002–041002–9, 2014.

[23] R. M. Damle, G. Colomer, O. Lehmkuhl, and I. Rodríguez. Energy simulation of buildings with a modular object-oriented tool. In *ISES Solar World Congress*, Kassel, 2011.

[24] I. Rodríguez, C. Pérez-Segarra, O. Lehmkuhl, and A. Oliva. Modular object-oriented methodology for the resolution of molten salt storage tanks for CSP plants. *Applied Energy*, 109:402–414, 2013.

[25] S. Torras, C. D. Pérez-Segarra, I. Rodríguez, J. Rigola, and A. Oliva. Parametric study of two-tank tes systems for CSP plants. *Energy Procedia*, 69:1049–1058, 2015. International Conference on Concentrating Solar Power and Chemical Energy Systems, SolarPACES 2014.

[26] N. Wakao, S. Kaguei, and T. Funazkri. Effect of fluid dispersion coefficients on particle-to-fluid heat transfer coefficients in packed beds: Correlation of nusselt numbers. *Chemical Engineering Science*, 34(3):325–336, 1979.

[27] J. G. Faber and F. H. Mead. *Oscar Faber's Reinforced Concrete, Second Edition*. Taylor & Francis, 1977.

[28] S. Helwany. *Applied Soil Mechanics with ABAQUS Applications*. John Wiley & Sons, 2007.

[29] S. Hansbo. *Foundation Engineering*. Developments in Geotechnical Engineering. Elsevier Science, 1994.

[30] A. Aysen. *Soil Mechanics: Basic Concepts and Engineering Applications*. Taylor & Francis, 2002.

[31] E. Zahavi, V. Torbilo, and S. Press. *Fatigue Design: Life Expectancy of Machine Parts*. A Solomon press book. Taylor & Francis, 1996.

[32] R. G. Budynas and J. K. Nisbett. *Shigley's Mechanical Engineering Design*. McGraw-Hill Education, 2014.

[33] A. B. Zavoico. Solar power tower design basis document revision 0. Technical report, Sandia National Laboratories SAND2001-2100, San Francisco, CA, July 2001.

[34] American Society of Mechanical Engineers. *An International Code - 2010 ASME Boiler & Pressure Vessel Code, Section II Part D - Properties (Customary) Materials*, July 2007.

[35] 10 MWe solar thermal central receiver pilot plant mode 5 (test 1150) and mode 6 (test 1160) Test Report. Technical report, McDonnell Douglas Astronautics Company, June 1986.

[36] P. A. Galione, C. D. Pérez-Segarra, I. Rodríguez, S. Torras, and J. Rigola. Multi-layered solid-PCM thermocline thermal storage for CSP. numerical evaluation of its application in a 50 MWe plant. *Solar Energy*, 119:134–150, 2015.

[37] S. Timoshenko and S. Woinowsky-Krieger. *Theory of Plates and Shells*. McGraw-Hill, 1959.

[38] I. Furuhashi, N. Kawasaki, and N. Kasahara. Evaluation charts of thermal stresses in cylindrical vessels contained fluid. *Journal of Computational Science and Technology*, 2:547–558, 2008.

[39] U. Herrmann, M. Geyer, and R. Kistner. The AndaSol project. Workshop on thermal storage for trough power systems. Technical report, FLABEG Solar Int. GmbH, Solar Millennium AG, February 2002.

[40] P. A. Galione, C. D. Pérez-Segarra, I. Rodríguez, S. Torras, and J. Rigola. Numerical evaluation of multi-layered solid-PCM thermocline-like tanks as thermal energy storage systems for CSP applications. *Energy Procedia*, 69:832–841, 2015. International Conference on Concentrating Solar Power and Chemical Energy Systems, SolarPACES 2014.

[41] Radiación solar en Andalucía. https://www.agenciaandaluzadelaenergia.es/Radiacion/radiacion1.php. Accessed: 2015-09-07.

[42] S. Meteotest Fabrikstrasse 14, CH-3012 Bern. Meteonorm 4.0, 1999.

[43] B. Kelly and D. Kearney. Thermal storage commercial plant design study for a 2-tank indirect molten salt system. Technical report, National Renewable Energy Laboratory (NREL), July 2006. Final Report.

[44] J. I. Burgaleta, S. Arias, and D. Ramirez. Gemasolar, the first tower thermosolar commercial plant with molten salt storage. In *SolarPACES 2011*, Granada, 2011.

[45] Gemasolar plant in Seville, Spain. http://www.sener-power-process.com/ENERGIA/ProjectsI/gemasolar/en. Accessed: 2015-09-21.

[46] C. Xu, Z. Wang, Y. He, X. Li, and F. Bai. Sensitivity analysis of the numerical study on the thermal performance of a packed-bed molten salt thermocline thermal storage system. *Applied Energy*, 92:65–75, 2012.

[47] A. Modi and C. D. Pérez-Segarra. Thermocline thermal storage systems for concentrated solar power plants: One-dimensional numerical model and comparative analysis. *Solar Energy*, 100:84–93, 2014.

[48] American Society of Mechanical Engineers. *An International Code - 2010 ASME Boiler & Pressure Vessel Code, Section VIII Rules for Construction of Pressure Vessels - Division 1*, July 2010.

6

Concluding remarks and future research

6.1 Concluding remarks

The thesis summarises the advances achieved in the numerical analysis of fluid-structure interaction. In this regard, a finite volume method for solid mechanics is developed, the incompressible fluid program is adapted for FSI problems and a coupled case of the solar thermal field is studied in detail.

The numerical method for structures is built under the same cell-centred finite volume infrastructure used for the fluid dynamics discretisation, resulting in a three-dimensional parallel code for unstructured meshes. As a result, a unified FSI approach will be obtained, setting a consistent and more flexible coupling strategy, and preserving a conservative formulation for the coupled discretised system.

Thermoelastic and hyperelastic (Saint Venant-Kirchhoff and neo-Hookean) materials are incorporated in the structural analysis. The former under the hypothesis of small deformations and the latters with no constraint in the magnitude of the strains. The nonlinear system of equations is integrated in time considering an updated Lagrangian formulation and an implicit incremental analysis. Spatial discretisation of the governing equations is performed by second-order schemes, which calculate the displacement gradient and stresses directly on the faces of the control volume in order to improve the accuracy of the solution.

Different time schemes have been tested and their integration errors numerically

quantified, including the Bathe method, which has been able to avoid the numerical instability shown by the Newmark scheme with decreasing time steps. Two different arrangements of the resulting linear system allow for reducing the time cost of the classical segregated method followed in finite volume discretisations. On the one hand, a segregated approach with an Aitken acceleration and a transient predictor step could save between 10 and 76 % of the computing time in the tested cases. On the other hand, the block-coupled arrangement reduced the time cost by 72 to 97 %.

Besides, a new partitioned FSI method based on an ALE form of the fluid governing equations for a conforming mesh has been developed. Two different moving mesh techniques, i.e. the pseudo-solid and the Laplacian, with a volume-based stiffness parameter have been implemented, showing effective operation under large displacements of the solid interface. The space conservation law is satisfied when evaluating the velocity of the faces of a control volume. A semi-implicit algorithm ensures numerical stability at a moderate computational cost for strongly coupled FSI phenomena. To showcase the potentiality of the implemented methodology, the airflow through a self-activated valve is analysed by using a simplified structural model.

The numerical solution predicts values of maximum amplitude and frequency of the structural vibration that are close to those captured in the experiment. However, the flow prevents the valve from closing completely, unlike seen in the experiment. The incompressibility constraint imposed in the air might be generating a too stiff fluid loading on the valve in view of the high pressure peaks.

As a concluding applied investigation, a new numerical coupled platform for packed-bed thermocline energy storage tanks has been presented and used to identify whether they are a viable alternative for concentrated solar power plants. The finite volume method for thermoelastic materials is used to model the tank walls. After validating the system modelling, criteria for tank sizing is proposed, and a parametric thermo-mechanical study is carried out under real working conditions.

Temperature gradient degradation has shown a different impact on thermal efficiency, depending on the temperature jump of the plant. From 75 % with 100 ºC to 55 % with 275 ºC. Thus, it seems appropriate to consider improvements like the multi-layered solid-PCM concept for plants with a high temperature difference. Numerical results show that material yielding, and hence thermal ratcheting, can be avoided with high yield strength metals and affordable wall thickness. Using filler material and fluid with similar densities helps to alleviate the exerted pressure on the walls considerably.

6.2 Future work

After the progress achieved with this thesis, it is clear that the first pending task is to integrate the implemented structural application within the developed FSI platform for incompressible flows. This work can pose some challenges with regard to parallelisation of the coupled calculation, data exchange between non-matching meshes or temporal synchronisation. The result will be an FSI simulation tool entirely modelled by the finite volume method which can comprise the strong interaction between incompressible turbulent flows and elastic structures subjected to large deformations. Biomechanical studies, such as the blood flow through arteries of complex geometry, could take advantage of this method [1].

Another future avenue of work with enormous potential is to extend the phenomenology captured on the fluid side of the FSI platform, beyond the Newtonian incompressible flows employed up to now. This would mean taking, for example, the multiphase [2] or compressible flow [3] methods that are already available within TermoFluids code and coupling them to the structural problem. The multiphase concept would allow to study canonical cases such as the impact of a breaking dam on an elastic wall [4] or the filling of an elastic container [5]. Costal engineering and naval architecture can exploit these FSI capabilities. On the other hand, contemplating compressible flows along with reed-type structures would offer a more realistic prediction of charge and discharge processes of hermetic reciprocating compressors, whose influence on the efficiency and reliability of the compressor is crucial [6].

Similarly, further material models can be added to the solid analysis aiming at generalising the FSI tool. The TermoFluids libraries for the solid medium have been designed in an abstract modular flexible way so that adding new constitutive models becomes a natural and relatively simple task. In this sense, plastic regime, incompressible deformation or viscoelastic materials could be implemented.

References

[1] Y. Bazilevs, V. M. Calo, Y. Zhang, and T. J. R. Hughes. Isogeometric fluid–structure interaction analysis with applications to arterial blood flow. *Computational Mechanics*, 38(4):310–322, 2006.

[2] N. Balcázar, L. Jofre, O. Lehmkuhl, J. Castro, and J. Rigola. A finite-volume/level-set method for simulating two-phase flows on unstructured grids. *International Journal of Multiphase Flow*, 64:55 – 72, 2014.

[3] J. B. Pedro, A. Báez-Vidal, O. Lehmkuhl, C. D. Pérez-Segarra, and A. Oliva. On the extension of LES methods from incompressible to compressible turbulent flows with application to turbulent channel flow. *Journal of Physics: Conference Series*, 745(3):032047, 2016.

[4] E. Walhorn, A. Kölke, B. Hübner, and D. Dinkler. Fluid–structure coupling within a monolithic model involving free surface flows. *Computers & Structures*, 83(25):2100 – 2111, 2005.

[5] A. Franci, E. Oñate, and J. M. Carbonell. Unified lagrangian formulation for solid and fluid mechanics and FSI problems. *Computer Methods in Applied Mechanics and Engineering*, 298:520 – 547, 2016.

[6] M. Schildhauer and A. Spille-Kohoff. Numerical simulation of fluid-structure interaction: Turek benchmark and kinetics of a reed valve. *Progress in Computational Fluid Dynamics, an International Journal*, 14(1):38–48, 2014.

Appendix A

List of publications

A.1 Journal Papers

- A. Naseri, I. González, A. Amani, C. D. Pérez-Segarra, A. Oliva. A second-order time accurate semi-implicit method for fluid–structure interaction problems. *Journal of Fluids and Structures*, 86:135-155, 2019.
- A. Naseri, O. Lehmkuhl, I. González, E. Bartrons, C. D. Pérez-Segarra and Assensi Oliva. A semi-implicit coupling technique for fluid-structure interaction problems with strong added-mass effect. *Journal of Fluids and Structures*, 80:94-112, 2018.
- I. González, C. D. Pérez-Segarra, O. Lehmkuhl, S. Torras, A. Oliva. Thermomechanical parametric analysis of packed-bed thermocline energy storage tanks. *Applied Energy*, 179:1106-1122, 2016.

A.2 Conference Proceedings

- I. González, A. Naseri, J. Chiva, J. Rigola, C. D. Pérez-Segarra. An enhanced finite volume based solver for thermoelastic materials in fluid-structure coupled problems. In *6th European Conference on Computational Mechanics*, Glasgow, June 2018.
- A. Naseri, I. González, A. Amani, C. D. Pérez-Segarra. Second-order semi-implicit partitioned method for fluid-structure interaction problems. In *6th European Conference on Computational Mechanics*, Glasgow, June 2018.

- I. González, A. Naseri, J. Rigola, C. D. Pérez-Segarra, A. Oliva. A fluid-structure interaction solver for the fluid flow through reed type valves. *IOP Conference Series: Materials Science and Engineering* 2017, 232(1):012032. In *10th International Conference on Compressors and their Systems*, London, September 2017.

- I. González, O. Lehmkuhl, A. Naseri, J. Rigola, A. Oliva. Fluid-structure interaction of a reed type valve. In *23rd International Compressor Engineering Conference at Purdue*, Indiana, July 2016.

- A. Naseri, O. Lehmkuhl, I. González, A. Oliva. Partitioned semi-implicit methods for simulation of biomechanical fluid-structure interaction problems. *Journal of Physics: Conference Series* 2016, 45:032020. In *7th European Thermal-Sciences Conference (Eurotherm)*, Krakow, June 2016.

- C. D. Pérez Segarra, I. González, S. Torras, J. Rigola, A. Oliva. Advanced analysis of thermal energy storage in CSP plants. In *European Energy Research Alliance Conference*, Birmingham, November 2016.

- I. González, O. Lehmkuhl, C. D. Pérez-Segarra, A. Oliva. Dynamic thermoelastic analysis of thermocline-like storage tanks. *Energy Procedia* 2015, 69:850-859. In *SolarPACES 2014: International Conference on Concentrating Solar Power and Chemical Energy Systems*, Beijing, September 2014.

- E. Guadamud, A. Oliva, O. Lehmkuhl, I. Rodriguez, I. González. Thermal analysis of a receiver for linear fresnel reflectors. *Energy Procedia* 2015, 69:405-414. In *SolarPACES 2014: International Conference on Concentrating Solar Power and Chemical Energy Systems*, Beijing, September 2014.